Numerical Study of a Microturbine Combustor

Master Thesis in Energy

Thermal Machines

Lars Møller-Pedersen

University of Bergen

Geophysical Institute

Western Norway University of Applied Sciences

The Faculty of Engineering and Sciences

Bergen, June 2018

Numerical Study of a Microturbine Combustor

Lars Møller-Pedersen

University of Bergen (UiB)
The Faculty of Mathematics and Natural Sciences
Geophysical Institute
Post Box 7803
5020 Bergen, Norway

In cooperation with:
Western Norway University of Applied Sciences (HVL)
The Faculty of Engineering and Sciences
Department of Mechanical and Marine Engineering (IMM)
Post Box 7030
5020 Bergen, Norway

Norwegian Title:	Numerisk analyse av brennkammer til en mikroturbin
Author:	Lars Møller-Pedersen
UiB student number:	151553
HVL student number:	134160
Program:	Master Programme in Energy, Thermal Machines
Course:	ENERGI399K
ECTS credits:	30
Date of submission:	1.6.2018
Supervisor, UiB:	Professor Martin Fernø
Supervisor, HVL:	Associate Professor Shokri Amzin
Number of files submitted:	1 (in .pdf format)
Simulation files available:	2 (in .sim format files for STAR-CCM+ 13.02.011)
Simulations can be obtained from:	Associate Professor Shokri Amzin

Preface

This 30 ECTS points master thesis is a project for the Department of Mechanical and Marine Engineering at Western Norway University of Applied Sciences. It is part of the master programme in Energy with specialization within thermal machines. The programme is run by the University of Bergen Geophysical Institute in cooperation with Western Norway University of Applied Sciences.

The thesis has been supervised by Associate Professor Shokri Amzin at Western Norway University of Applied Sciences Department of Mechanical and Marine Engineering. It has been co-supervised by Professor Martin Fernø at University of Bergen Department of Physics and Technology.

The topic for this thesis is numerical simulation using computational fluid dynamics (CFD) of a small gas turbine engine combustion chamber. The CFD-software used is Siemens STAR-CCM+.

I would like to acknowledge the following people and thank them for their support with this project:

Associate Professor (HVL) Shokri Amzin for guidance, assistance and valuable advice.

Professor (UiB) Martin Fernø for valuable advice on scientific writing.

Thermal Machines Programme Lead Associate Professor (HVL) Lars Magne Nerheim and The Department of Mechanical and Marine Engineering for providing a relevant and interesting engineering task to examine.

My fellow students in the Thermal Machines programme and co-students sharing room D425 for their friendship and good spirits.

Siemens for providing a free student license of the full STAR-CCM+ software without any restrictions on grid size and resolution. This work would not have been possible without this software package.

I would also like to send a special thanks to my partner Maria-Isabell Heimark. This work would have been much more difficult to accomplish without your continued positive support.

Abstract

Microturbines are small-scale gas turbine engines with a power range of 20 to 500 kW, typically used for off-grid power generation or mechanical drive scenarios. The technology also shows potential in combination with high-temperature fuel cell technology to provide high chemical to electrical energy conversion efficiency with very low emissions.

A core component in the microturbine is the combustor where the fuel is oxidised with compressed air, releasing its chemical energy. A cost-efficient combustion chamber is needed that will burn the fuel with high efficiency and low formation of pollutants such as Carbon Monoxide (CO) and Nitrogen Oxides (NO_x). The Department of Mechanical and Marine Engineering at Western Norway University of Applied Sciences has a microturbine that is used for demonstration purposes. The combustor is a simple can-type combustor fuelled by propane. The combustor is a very simple design with a straight perforated flame tube. It is assumed that this design can be improved with regards to combustion efficiency and lower emissions.

This thesis contains numerical simulations of the selected microturbine combustor using a Computational Fluid Dynamics tool. The numerical algorithm solves the Navier-Stokes transport equations iteratively in the context of Reynolds-averaged Navier-Stokes paradigm. The K-Epsilon model is incorporated into the algorithm to account for the turbulence effects. The mean reaction rate term in the averaged species transport equations are closed using the Steady Laminar Flamelet model. The computational costs of this method are lower compared to other more complex approaches. The geometry of the investigated combustor mimics the non-premixed combustion mode where the fuel and oxidiser streams are segregated. The first numerical model represents the exact geometry of the installed combustor. The initial and boundary conditions are chosen from experimental data. Experimental data is also used for model validation.

The results from the numerical simulation are provided for scalars such as temperature, velocity, unburnt fuel, CO and NO_x. The results show that the selected combustor is a compromised design with excessive temperatures, incomplete combustion and high CO emissions.

The second numerical computations represent a modified design of the first case, with the same initial and boundary conditions. The proposed model has a larger diameter with a complex geometry. A swirler device is introduced to improve the mixing between the fuel and the oxidiser, to enhance the combustion and to reduce emissions. The computed scalars of interest such as major and minor species and mean temperature obtained from the modified combustor are compared with the original combustor. This proposed model requires further validation with laboratory measurements. The model can also serve as a basis for further design improvements before a prototype is built.

Abbreviations

The abbreviation used in this document are given in table 1. They are provided for quick reference.

Table 1: *Table of abbreviations that are used in this thesis.*

AFR	Air/fuel ratio
CAD	Computer-aided Design
CFD	Computational Fluid Dynamics
CO_2	Carbon Dioxide
CO	Carbon Monoxide
CPU	Central Processing Unit
DNS	Direct Numerical Simulation
FGM	Flamelet Generated Manifold
GRI	Gas Research Institute
GTE	Gas Turbine Engine
GTFC	Gas Turbine Fuel Cell
HVL	Western Norway University of Applied Sciences
IMM	Department of Mechanical and Marine Engineering
IPCC	Intergovernmental Panel on Climate Change
LES	Large Eddy Simulation
LFC	Laminar Flame Concept
NO_x	Nitrogen Oxides
UHC	Unburnt Hydrocarbons
PDF	Probability Density Function
RANS	Reynolds-averaged Navier-Stokes
rpm	Revolutions per minute
SCR	Selective Catalytic Reduction
SLF	Steady Laminar Flamelet
UiB	University of Bergen
ppmw	Parts per million weight
SO_x	Sulphur Oxides

Table of Content

1.0 Introduction

It is well documented that burning of carbon-based fuels to fulfil energy demands has a severe impact on mankind and the environment. The harvesting of fuel resources is polluting and energy intensive. The combustion process itself generates emissions which have an impact on the environment and public health. For example, issues such as air quality, global warming, smog, ozone depletion, acid rain and ocean acidification are common topics in leading scientific debates [1]. In addition, both minor species such as unburnt hydrocarbons (UHC) and major species Carbon Dioxide (CO_2) contributes to the greenhouse effect and global warming. These effects are well documented by the Intergovernmental Panel on Climate Change (IPCC). Despite these negative effects, the combustion of carbon-based fuels will dominant as a major energy source.

Technological development, economic growth, emerging economies and more stringent local, regional and global environmental legislation require a drive for improved combustion systems with higher efficiencies and lower emissions. These systems need to be flexible so that they can be used with the various fuels locally available. They must also have an improved thermal efficiency so that less fuel is needed to achieve the same amount of useful energy. Additionally, lower emission levels per unit of fuel spent are required to reduce the environmental and health related impacts related to combustion.

With this motivation, the main objective of this work is to examine a combustor for a small gas turbine engine (GTE), often referred to as a microturbine. The combustor of interest is used by faculty for demonstrations, testing and hopefully in future research. However, as it stands today its design is basic and there is room for improvement with regards to both combustion efficiency and emissions.

The selected combustor will be numerically simulated with its existing design to investigate several engineering scalars of interest such as turbine outlet temperatures, temperature distributions and the formation of emissions. The existing microturbine combustor design requires improvement to increase its efficiency and to reduce the emissions generated. A better design is to be proposed based on extensive numerical calculations. The obtained results will be evaluated for recommendations on future design and construction.

The numerical computations are performed using Siemens STAR-CCM+ software. Two different numerical computations representing the original and the proposed design are performed. The solutions are obtained using the Steady Laminar Flamelet (SLF) Reynolds-averaged Navier Stokes (RANS) approach. The first case represents the original design while the second case represents the improved design. The initial and boundary conditions are the same for both cases.

The outline of this thesis is as follows; Chapter 2 provides background information on microturbines, combustors and a short overview of other work concerning computational fluid dynamics (CFD) and combustor simulation. Chapter 3 describes the methods used, hereunder introducing the governing equations that are solved by the software. The methods chapter also introduces the setup of the cases for simulation, including the geometry, physical models, initial- and boundary conditions, mesh and mesh sensitivity analysis. The simulation results are provided and discussed in chapter 4. Suggestions for future work are also provide here. Chapter 5 concludes the work.

2.0 Background

This chapter contains some background information on the topic of microturbines. It begins with introducing the working principles of gas turbines engines and continues with how the basic emissions are formed and how combustor performance can be evaluated. It continues with an introduction of the combustor and its main parts and describes the combustor on the HVL GTE. There is also a short literary review of some articles on the topic of CFD and numerical simulation of combustors. This chapter is provided to give some background information on the topic of this thesis.

2.1 Microturbines

Microturbines are small-scale gas turbine engines, approximately the size of a large household refrigerator [2], with a typical power range of 20 kW on the low end and up to 500 kW on the high end [2, 3]. There are many potential applications for the use of microturbines, such as off-grid power generation in remote areas without a power infrastructure or in mechanical drive scenarios such as the running pumps or refrigeration compressors. Recent advances in control systems also allows for grid-connected microturbines used in distributed power generation [3].

The working principles and thermodynamics of the microturbine are like those of the large industrial gas turbine engines used for power generation and propulsion. The microturbines are usually equipped with centrifugal compressors of a radial design derived from small turboprop engines, turbochargers or auxiliary power units [3].

As their larger counterparts, microturbines are mass flow engines that follow the principle of the Brayton Cycle. To maximize the output power the tip of the compressor rotors and the turbine blades have to move close to the speed of sound [3]. Because of the small size of these devices, meaning the diameter from centreline to the tip of the blades, the rotation frequency has to be as high as 90,000 to 120,000 revolutions per minute (rpm) to reach these speeds [2].

Microturbines are still relatively new to the marketplace and the numbers of installed systems are relatively low. Therefore, the costs associated with the systems are still high compared to reciprocal machines [2, 3]. Some microturbines are equipped with a recuperator; a heat exchanger that transfers heat from the hot exhaust gasses to the compressed air prior to the combustor. This increases overall efficiency [3]. Microturbines can also be combined with high-temperature fuel cell technology in gas turbine fuel cell (GTFC) hybrids. Still expensive and in development, such GTFCs have to the potential of reaching very high fuel to electric power conversion efficiency in addition to very low emission levels [2, 4].

2.2 The Brayton Cycle

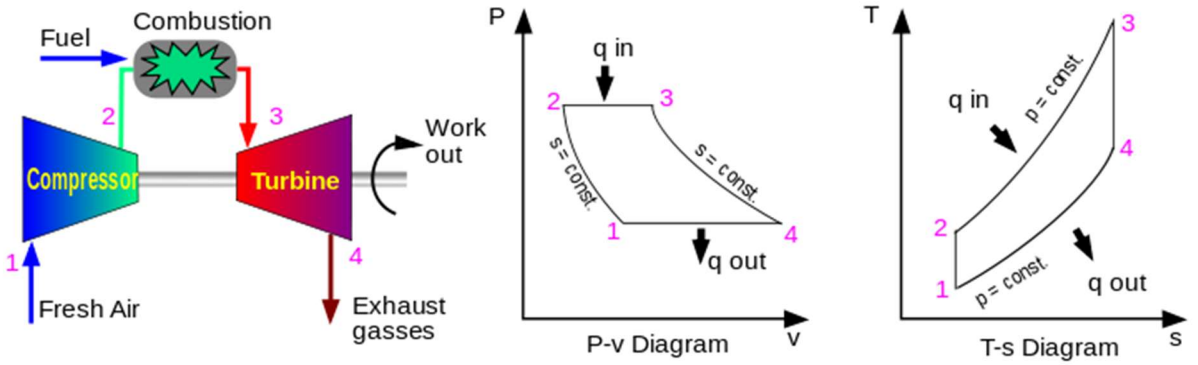

Figure 1: *This figure shows the principle of a simple cycle gas turbine engine and the corresponding pressure-volume (P-v) and temperature-entropy (T-s) diagram. Image courtesy of Wikipedia [5].*

Figure 1 shows the Brayton Cycle. The heat input to the Brayton Cycle for the GTE is provided by the combustor. Prior to combustion, the flow of air is compressed and accelerated by the compressor. This process increases the temperature and the total pressure of the airflow [6].

Gaseous fuels can be mixed with a portion of the compressed air prior to entering the combustion chamber. This is called premixed combustion and result in a homogeneous flame. The fuel and compressed air can also enter the combustor separately. This is called non-premixed or partially premixed combustion. The resulting combustion is a diffusion flame which rate of combustion is governed by the diffusion rate of the fuel and air mixture [7].

Inside the combustor, the fuel is burnt close to stoichiometrically with between 8-30 % of the inlet air from the compressor [6]. Close to stoichiometric combustion is necessary because a high temperature is needed for a sufficiently rapid combustion process to occur in the moving air-stream. The combustion process must be completed inside the limited space, and therefore limited timeframe, of the combustor [8].

To expand the available timeframe for complete combustion and to avoid flame extinguishing, the rapid moving airflow from the compressor can be slowed. Therefore, there can be a diffusion stage prior to the combustor that provides a volumetric expansion to slow the incoming airflow from the compressor.

The moving airflow is then mixed with the fuel and burnt either premixed or non-premixed under constant pressure conditions. The desired effect is to raise the temperature of the high-pressure gas [6]. This increase in temperature will cause the gasses to expand, thus providing a rapid flow of hot exhaust gas that drives the turbine.

The air that is not consumed in the primary combustion is mixed with the hot expanding gasses in later steps inside the combustor to protect the combustor liner from high temperature, to dilute the hot gasses and thus controlling the turbine inlet temperature. Another major aspect of the additional airflow is to control emissions formed in the primary combustion zone by reducing temperatures [6].

2.3 Real Cycle with Losses

The actual process that takes place inside the combustor deviates from the idealized Brayton Cycle due to various losses that will change the real-world performance. When comparing the Brayton Cycle in figure 1 with the real cycle, there is no constant entropy and pressure due to irreversibility and losses.

Frictional losses are introduced by turbulence and skin friction. These are major contributors to pressure loss in the combustor. Turbulence is primarily introduced by mixing devices that mix the incoming airflow with the fuel and by the dilution of the hot exhaust gasses needed to provide the right turbine inlet temperature. Effective mixing is needed, and turbulence is needed to provide this effective mixing. However increased turbulence will introduce larger frictional losses. Therefore, a balance needs to be struck to prevent excessive frictional losses due to turbulence effects, but still provide sufficient mixing. Frictional loss due to skin friction come from the interaction between the moving turbulent gas stream and the inner surfaces of the combustor, combustor liner and the transition ducts between the combustion chamber and the turbine inlet. A long transition between the combustor and the turbine inlet will provide a more uniform temperature profile to the turbine but increase the frictional loss. Here a balance must also be struck between pressure loss due to friction and the needed temperature profile [8].

Pressure loss is also due to a physical phenomenon called fundamental loss. An increase in the temperature of the gasses gives a decrease in density. The gas is expanded, resulting in an increase of the velocity and momentum of the gas stream. Considering the principle of conservation of momentum, a force is needed to provide this change in momentum. This force is provided by a pressure drop over a given area ($\Delta P \times A$). Because of this a pressure drop due to fundamental loss is unavoidable. In scale it is however much lower than the pressure loss introduced by turbulence and skin friction with a factor of about between 10 to 20 times depending on the design [8].

2.4 The Formation of Pollutants

In the early days of gas turbine engine research, the primary focus in combustor development was on increasing combustion efficiency, improving flame stability and the prevention of visible smoke. These design goals led to higher pressure ratios, higher combustion temperatures and higher turbine inlet temperatures. The consequence was an increase in Nitrogen Oxides (NO_x) emissions [8]. The mechanisms of NO_x formation were not thoroughly understood, and the reduction of NO_x was not a driving factor in development. This would change with the increasing problems of visible air pollution and the ratification of stricter environmental regulations.

Today reduction of emissions is the most important factor influencing the design of gas turbines in general. An overview of the major emissions is presented in table 2.

Table 2: *Table containing a short overview of the products of emissions and the resulting undesired effects. The content of the table is from [8].*

Emission	Short description of the undesired effect
CO_2	Greenhouse gas which formation is a by-product of combustion. The amount of CO_2 formed is directly related to the carbon content of the fuel consumed in the combustor. It cannot be reduced by combustor design although after-treatment is a topic for future research and innovation. Higher thermal efficiency will reduce CO_2 emissions with regards to power output because less fuel is needed for the same output.
NO_x	Nitrogen Oxides formed during combustion. NO_x in combination with heat and sunlight creates smog. It can also cause acid rain and depletion of ozone at high altitudes. NO_x is poisonous for humans to inhale.
CO	Carbon Monoxide (CO) is a by-product of incomplete combustion due to inadequate temperatures or to short timeframe to form the end-product CO_2. CO is poisonous to inhale.
UHC	Unburnt hydrocarbons are a product of incomplete combustion. The type of UHC emitted from the combustion is fuel dependent. Some UHCs can cause cancer, others are potent greenhouse gasses.
SO_x	Sulphur Oxides (SO_x) are formed by the sulphur content of the fuel during combustion. It is known for causing acidic rain when reacting with water in the atmosphere. SO_x is quite easily remedied by using fuel that has the sulphur content reduced to insignificant levels.

There are three sources that form NO_x during combustion. There is thermal NO_x, prompt NO_x and fuel NO_x. As indicated by its name, thermal NO_x is formed by the presence of the high temperatures that are needed to drive the chemical reactions [7]. The formation of NO_x varies exponentially with the flame temperature. The higher the temperature, the more NO_x is formed [8]. Both the oxygen and nitrogen that react in this chemical process originate from the air itself and the NO_x is formed following the Zel'dovich mechanism of Nitrogen Oxide formation. There are also other more recently discovered mechanisms for thermal NO_x formation. Thermal NO_x is the major contributor to total NO_x formation in the combustion process [7].

Prompt NO_x is formed by hydrocarbon radicals that react with nitrogen from the air. Formation follows a complex series of reactions. Prompt NO_x is a minor contributor to the total NO_x formation [7].

The third source is fuel NO_x that is formed by nitrogen bound in the hydrocarbon fuel reacting with oxygen from the air. This source of NO_x can be eliminated by using fuel that contains insignificant quantities of nitrogen [7].

2.5 Emissions Control Parameters

In all modern combustors, there is a need to control emissions of NO_x, CO and UHC. Early combustor designs did not operate premixed, resulting in a stable diffusion flame with very high emissions. Modern combustors are lean premixing systems, a design driven by the need to reduce emissions. Lean premixed combustion is more challenging to operate stably, but is necessary from an emissions standpoint [8]. The combustor in use on the HVL GTE is non-premixed, so higher levels of emissions are expected by design.

The key to reducing emissions is closely linked to the combustion temperature and resident time. Various design features influence these properties. In general, there are three main methods of lowering emissions [8]:

1) Flame temperature reduction. The flame temperature can be reduced by dilution. This can be done by the injection of water or steam.
2) Dry low NO_x methods. There are multiple possibilities and combinations under the same nomenclature. One such method is premixing with lean burning, another is rich burning with quick quenching.
3) Exhaust after-treatment. This is an after-treatment of the exhaust gasses and not affecting the combustion directly. One such method is the selective catalytic reduction (SCR).

The flame temperature has a major effect on the formation of NO_x, CO and UHC emissions. The adiabatic flame temperature is the maximum temperature the combustion of a given fuel can reach if no heat is exchanged with the environment. Stoichiometric combustion is close to the adiabatic flame temperature. Combustion at close to stoichiometric conditions will give high-temperature combustion with resulting high NO_x formation. Increasing the air/fuel ratio (AFR) will dilute the mixture and reduce the flame temperature. This will decrease NO_x formation, but as the AFR increases so will CO and UHC due to incomplete combustion.

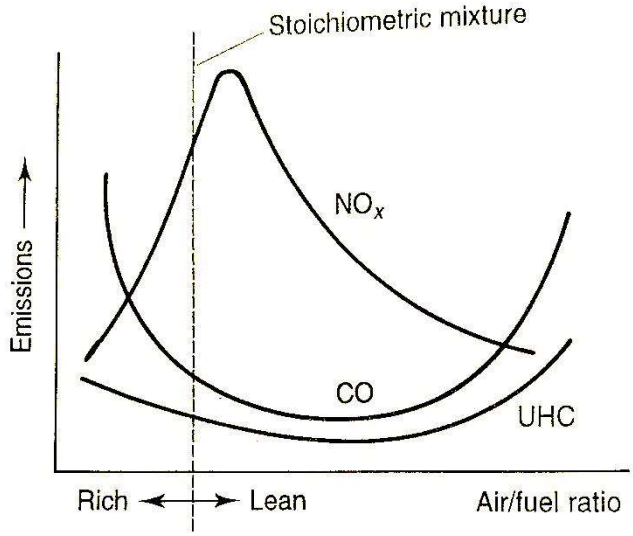

Figure 2: *Figure showing the quantity of emissions formed with regards to air/fuel ratio. Figure courtesy of [8].*

Another means of reducing the flame temperature is to introduce water or steam to the combustion process. The added water will increase the mass flow and the heat capacity of the airstream. This will in turn, reduce the combustion temperature as more heat is absorbed by the stream. However, the amount of water needed is substantial for large-scale gas turbines engines and the water must also be demineralized to avoid scale formation of particles, salts and minerals that will cause long-term damage to the combustor and turbine. Steam can often be generated by waste heat recovery heat exchange with the hot exhaust gasses. It must be injected under pressure into the flow of high pressure compressed air. Adding water or steam will further reduce NO_x formation, but excessive injection can increase CO and UHC formation due to incomplete combustion [8]. For microturbines water or steam injection is impractical due to the added complexity of such systems. Large quantities of demineralized water are also impractical for many applications.

Dry low NO_x is a common denominator for various methods to reduce emissions without water or steam injection. These dry methods are accomplished by manipulating the factors that affect the formation of emissions, such as resident time and air/fuel ratio. The resident time of the chemical reactions inside the combustor affects the total emissions. Changes in the geometry, such as an increase in cross-sectional area, volume or adding an orifice can affect the flow rate and thus affect the resident time.

As can be seen from figure 2, both rich and lean burning can affect emissions. One method is to have a rich burning primary combustion zone, followed by dilution and a secondary combustion zone. However, the most common methods are variants of lean premixing, also possible in primary and secondary combustion zones.

2.6 Combustor Performance Considerations

There are many considerations when evaluating good combustor performance. Important benchmarks are combustion efficiency, pressure loss, outlet temperature profile, combustion stability and combustion intensity.

Combustion efficiency is a measure of the completeness of the combustion. All fuel that enters the combustor should ideally be burnt from both an economic and an environmental or emissions perspective [6]. The slip of unburnt fuel can be challenging to measure accurately due to the high amount of dilution. It is also difficult to take a representative sample. It is, therefore, easier to calculate the combustion efficiency [9]. The combustion efficiency is seldom lower than 98%, so very accurate measurements of pressure and temperature are needed, which is an instrumentation challenge [8].

Combustion efficiency: $$\eta_{combustion} = \frac{\Delta h_{actual}}{\Delta h_{theoretical}} = \frac{(\dot{m}_a + \dot{m}_f) \times h_3 - (\dot{m}_a \times h_2)}{\dot{m}_f \times LHV} \quad (1)$$

Where:

Δh	=	change in enthalpy (heat increase)
h_2	=	enthalpy leaving the compressor
h_3	=	enthalpy entering the turbine
$\dot{m}_a$	=	air mass flow rate
$\dot{m}_f$	=	fuel mass flow rate
LHV	=	lower heating value of the fuel

Pressure loss from turbulence, skin friction and fundamental loss as is a major challenge in combustor design. The pressure loss should be as low as possible but cannot be eliminated. The pressure loss for a good design is usually about 2-4 % of the compressor outlet pressure. Aerodynamic changes caused by erosion or carbon deposits can also cause pressure loss [6].

The outlet temperature profile is also a major design consideration. This includes temperature profile uniformity, temperature gradients and metal temperatures. Temperature profile uniformity at the combustor outlet is essential to avoid damage to highly stressed turbine blades. The traverse number is used to describe the evenness of the profile. The traverse number should have a low value of about 0.05 to 0.15 [6].

Traverse number: $$N_t = \frac{peak\ gas\ temperature - mean\ gas\ temperature}{mean\ temperature\ rise\ in\ the\ turbine\ nozzle} \quad (2)$$

Steep temperature gradients should be avoided to prevent stress and damage to materials. Metal temperatures should also be moderate to avoid damage. This is accomplished by air film cooling of the liner, transition ducts and turbine stators and rotors. Thermal barrier coating is also used [6].

Combustion stability is determined by the region were stable combustion can take place. There is a rich limit with too much fuel compared to air and there is a weak limit where the mixture is too diluted. The result will be flame extinguishing, although combustion instability will occur first. Figure 3 shows a typical stability loop for a combustor, although the values might be different depending on design and size [8].

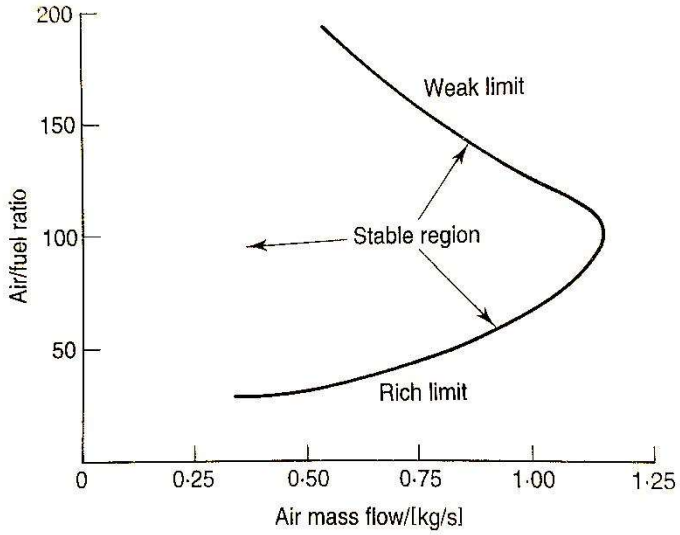

Figure 3: *Figure showing the combustion stability. The stable region is defined with regards to air/fuel ratio and air mass flow rate. Flame extinguishing will occur at both to rich and to diluted fuel and air mixtures. Figure courtesy of [8].*

Combustion intensity is a quality linked to the heat release rate and size of the combustor [8].

Nominal heat release:

$$Nominal\ heat\ release = \dot{m}_a \times AFR \times net\ calorific\ value\ of\ the\ fuel \qquad (3)$$

The required heat release from the combustor is a major factor for determining the size. A large volume will make it easier to design for lower pressure drop, higher combustion efficiency, more uniform temperature distribution and to operate within stability limits. The term combustion intensity is used to describe the relation between heat release and combustor size [8].

Combustion intensity:

$$Combustion\ intensity\ = \frac{heat\ release\ rate}{combustor\ volume \times pressure}\ \frac{[kW]}{[m^3 \times atm]} \qquad (4)$$

2.7 Description of the Main Combustor Parts

Combustors for GTEs typically consist of the same basic parts and working principles. This section provides a short overview of the main components for basic background information.

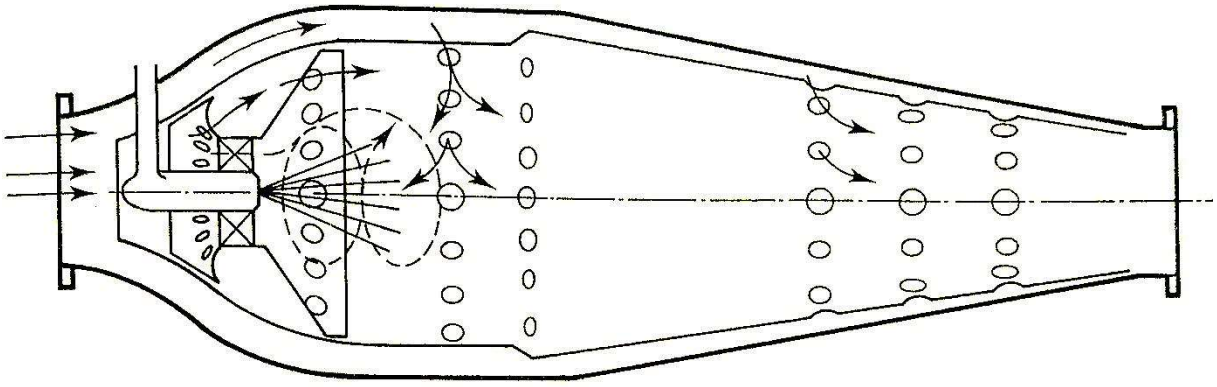

Figure 4: *Example of a combustion chamber with swirler. Figure courtesy of [8].*

The outer wall is called the casing. The main purpose of the casing is to house the combustor and protect if from the outside environment. The inner wall in figure 4 is the liner, in this thesis also referred to as the flame tube. The liner contains the combustion and its inner walls can be exposed to very high temperatures. The liner is perforated to allow for airflow from the volume between the casing and the liner to enter the zones of combustion. The compressed air enters the combustor from the air inlet and is distributed to the various zones. Fuel enters through the fuel inlet and is oxidised in the combustor, releasing heat stored as chemical energy.

The combustor can be sectioned into three main zones. The primary zone is where the combustion takes place. 15-20 % of the air flow is introduced in the primary zone. About 30 % of the air is introduced in the secondary zone through holes in the combustor liner. The secondary air flow completes the combustion process. The holes must introduce the air carefully to avoid local combustion cooling. The secondary airflow can also be used to create an air film that protects the liner metal from elevated temperatures and hot streaks. The tertiary zone is for dilution of the hot gasses. The remaining air enters through the liner to obtain the right combustor outlet and turbine inlet temperature.

It is common for combustors to has devices for flame stabilization. Often there is a diffusor stage before the combustor inlet to slow down the incoming airstream. A swirler is often introduced to create a circulating flow pattering to control and contain the combustion. Pressure differences will direct some of the burning mixture back towards the incoming air and fuel. The swirler also accelerates the mixing of air and fuel in the case of non-premixed combustion. It is common for some of the air to be directed back towards the combustion for flame stabilization.

2.7.1 The Experimental Setup

Details of the experimental setup can be referenced in Mjølhus et al. [10], Leknes et al. [11], Bergquist et al. [12] and Larsson et al. [13]. A short system description is provided here.

The experimental setup of the HVL GTE consists of a centrifugal compressor of radial design. The turbine is also a radial design. These components are sourced from bus and lorry diesel engines. The compressor has been modified with an improved air inlet funnel and the rotating compressor blade assembly has been upgraded and modified for improved performance. The combustion chamber is created from welded 316L stainless steel parts. The setup also has an additional power turbine that can be moved in and out of the setup, so the system can run with or without this turbine. The power turbine is connected to a generator. There is a lube oil circuit for lubrication and cooling of the bearings. The circuit is equipped with a pump to build up supply pressure and a heat exchanger for cooling of the lube oil. The propane fuel is supplied from a portable metal canister. The canister is heated in a water bath to build up gas pressure and to prevent cooldown and reduction of gas pressure when fuel exits the canister. There is a regulator valve to regulate the fuel supply. The fuel inlet hose and fuel nozzle are sourced from as gas burner. The combustor is equipped with a spark plug for fuel ignition.

Instrumentation consists of compressor rotational speed, five temperature measurements points, two pressure measurement points in addition to gauges for lube oil pressure and temperature. The five temperature measurement points measure air inlet temperature, air temperature between compressor and combustor, combustor outlet temperature (T3), turbine outlet temperature and exhaust outlet temperature after the power turbine. Pressure measurement points are located between the compressor outlet and the combustor inlet in addition to the combustor outlet (P3). The pressure sensors measure the stagnation pressure of the flow.

2.8 Literary Review of Combustor CFD Modelling

CFD and combustion modelling is not a new field. Extensive work exists on modelling the combustion of various fuels ranging from hydrogen and methane to heavy hydrocarbons in test burners and using experimental data to develop and validate combustion mechanisms and models. With the arrival of increasingly powerful computer systems and increased availability to researchers, this is a common research topic. One such study has recently been performed at HVL IMM by Munteanu [14].

Due to the limited size of the burner and flame in combination with light-weight chemical mechanisms such research can be performed with computer-intensive methods such as Large Eddy Simulation (LES) and even Direct Numerical Simulation (DNS). For larger and more complicated geometries the RANS method is still prevailing for many industrial applications.

The work presented in this thesis is more related to the industrial application of combustion modelling. Work such as the combustion modelling of a Siemens SGT-100 dry low emissions combustor with swirler performed by Mallouppas et al. [15] presents the state of the art of what is possible with the commercial software code in STAR-CCM+. In this work, premixed combustion with the Flamelet Generated Manifold (FGM) method is compared to the Laminar Flame Concept (LFC) method and both are compared to experimental measurements of CO and NO_x emissions. The work points out some interesting findings such a tendency for overprediction of CO and NO_x from both methods compared to experimental measurements. A significant portion of the NO_x formation also happens just outside the combustor outlet. The model uses a high-resolution mesh with up to 44 million cells for sensitivity analysis solved using the LES method.

A more realistic approach with regards to the available computational power is presented by Calabria et al. [16]. In this work, a Turbec T100 microturbine combustor is modelled using the RANS method with K-Epsilon viscosity. The numerical model contains proximately four million nodes and the calculations are performed in ANSYS commercial software. The boundary conditions for this combustor are significantly larger than for the work in this thesis with approximately four times the air mass flow rate and about double the inlet temperature and pressure. The purpose of Calabria et al. is to model the existing design of the T100 microturbine combustor that runs on gaseous fuel, validate the numerical model with experimental data and create a new design of the microturbine for use with liquid fuel. This is the same approach as in my own work. The article has an interesting finding in that the centre mounted fuel injector with swirler functions well under full operating power but has problems at 80 % and 60 % load.

The work of Enagi et al. [17] is centred around a combustor design quite similar to the HVL GTE. Its design features two straight tubes manufactured from 6 mm stainless steel. The inner tube is perforated with holes in three distinct zones. The fuel inlet is on the centreline on the top and compressed air flows in for one side. There is no swirling device. The combustor is longer and has a wider diameter, but overall this design is very similar to the case presented in my work. The combustor runs on liquid petroleum gas. Enagi et al. used Solidworks software for computer-aided design (CAD) and ANSYS Fluent for CFD simulation using species transport method for non-premixed combustion. A radiation model is also used. Optimization was performed to find the ideal length, diameter and diameter of the holes in the flame tube. The combustor was built, tested and compared to the numerical model.

Krieger at al [18] also features a combustor design with two straight tubes. The design is a counter-flow type, where the air inlet is close to the outlet. This forces the air to pass in the opposite direction than the flow inside the flame tube. This has the advantage of introducing cooler dilution air and pre-heating the air directed towards the primary zone. The design features a swirler device and an orifice. The software used is ANSYS Fluent. The numerical model uses the RANS method and has 3.9 million cells. The numerical model is validated against experimental data. An interesting finding of Krieger at al is that adding heat transfer models to the numerical simulation does not affect sampled temperatures in the model, but it does affect the flow profile. In the article, it is also pointed out that comparison of single measurement points can be misleading. Another interesting finding is that the swirler can be improved by designing it so that air can enter the combustor through the swirler closer to the centre. This makes mixing more effective.

This short literary review has shown that similar approaches to numerical combustor simulation has yielded satisfactory results and is a viable approach. Every design is however unique and numerical modelling can provide insights into parameters and scalars that are difficult to observe or measure in real-world scenarios. This thesis will provide insights specific to the combustor at HVL that are not available from other work. As is also shown by the other work referenced here, it is important to remember numerical simulations have limitations. The insights the model provides is only as good as the quality of the geometry, mesh, boundary conditions and computational methods. Some will yield more accurate results than others. Over- and underpredictions should be expected.

3.0 Turbulent Combustion Modelling

3.1 Governing Equations

The content of this section is based on [9, 19] in addition to the Star-CCM+ software documentation. However, as pointed out in [19] these sections appear quite similar in most literature and articles. For turbulent reacting flows, some of the fundamental Navier-Stokes equations for non-reacting turbulent flows need some additional terms to accommodate the chemical reactions taking place. The main differences can be summarized as follows [9]:

1) Reacting gas is non-isothermal. It contains a mixture of species that must be tracked individually and the heat capacity changes significantly with change in temperature and composition.
2) The species in the flow react chemically, and the reaction rate must be considered.
3) The gas is a mixture of several species. Transport coefficients such as species diffusion and viscosity must be accounted for.

3.1.1 Conservation of Mass (Continuity Equation)

For the fundamental equation for conservation of mass, there are no additional terms in the reacting flow compared to the non-reacting flow. This is because the combustion process does not generate or remove any mass from the flow [9].

Conservation of mass:

$$\frac{\partial \rho}{\partial t} + \frac{\partial \rho u_i}{\partial x_i} = 0 \qquad (5)$$

Where:

ρ = density (m/V, mass per unit volume).

u_i = three-dimensional velocity field.

For a given chemical species, species k, the conservation of mass for this species can be written as the equation 6.

Conservation of species k:

$$\frac{\partial \rho Y_k}{\partial t} + \frac{\partial}{\partial x_i}\left(\rho\left(u_i + V_{k,i}\right)Y_k\right) = \dot{\omega}_k \qquad for\ k = 1, N \tag{6}$$

Where:

Y_k = mass fraction of species k (m_k / m).

$V_{k,i}$ = i-component of the diffusion velocity V_k of species k.

$\dot{\omega}_k$ = the reaction rate of species k.

In the Star-CCM+ documentation, conservation of mass, equation 5, is presented in the following form empathizing the vector-based nature of the CFD numerical calculations [20]:

Conservation of mass:

$$\frac{\partial \rho}{\partial t} + \boldsymbol{\nabla} \cdot (\rho \boldsymbol{v}) = 0 \tag{7}$$

Where:

$\boldsymbol{v}$ = continuum velocity vector.

$\boldsymbol{\nabla}$= Nabla operator = $(\frac{\partial}{\partial x}, \frac{\partial}{\partial y}, \frac{\partial}{\partial z})$.

When integrating the conservation of mass in vector form, equation 7, over a finite control volume, the equation can be written in the form shown below [21].

Conservation of mass:

$$\frac{\partial}{\partial t}\int_V \rho dV + \oint_A \rho \boldsymbol{v} \cdot d\boldsymbol{a} = \int_V S_u dV \tag{8}$$

3.1.2 Conservation of Momentum

As for the equation for conservation of mass, the equation for conservation of momentum is the same for reacting and non-reacting flows. However, even though the momentum equations are the same the flow behaviour can be very different. The combustion will modify the dynamic viscosity, temperature, density and velocities. This causes the local Reynolds number in the reacting flow to vary much more than in a similar setup with a non-reacting flow [9, 20].

Conservation of linear momentum:

$$\frac{\partial(\rho v)}{\partial t} + \boldsymbol{\nabla} \cdot (\rho \boldsymbol{v} \otimes \boldsymbol{v}) = \nabla \cdot \boldsymbol{\sigma} + \boldsymbol{f_b} \qquad (9)$$

Where:

$\otimes$ = tensor product (Kronecker product).

$\boldsymbol{f_b}$ = Resultant of the body forces (per unit volume).

$\boldsymbol{\sigma}$ = Stress tensor.

For a fluid the stress tensor if often written as the sum of the normal and shear stresses [20].

Sum of normal and shear stresses:

$$\boldsymbol{\sigma} = -p\boldsymbol{I} + \boldsymbol{T} \qquad (10)$$

Where:

p = pressure.

T = viscous stress tensor.

The sum of the normal and shear stresses, equation 10, can be inserted into the equation for conservation of linear momentum, equation 9, and integrated over a finite control volume. The final equation can be written in the form below, equation 11, and implemented in the solver [21].

Conservation of linear momentum:

$$\frac{\partial}{\partial t}\int_V \rho \boldsymbol{v} dV + \oint_A \rho \boldsymbol{v} \otimes \boldsymbol{v} \cdot d\boldsymbol{a} = -\oint_A p\boldsymbol{I} \cdot d\boldsymbol{a} + \oint_A \boldsymbol{T} \cdot d\boldsymbol{a} + \int_V \boldsymbol{f}_b dV \qquad (11)$$

3.1.3 Conservation of Angular Momentum

Conservation of angular momentum requires that the stress tensor is symmetric/transposed [20].

Conservation of angular momentum:

$$\boldsymbol{\sigma} = \boldsymbol{\sigma}^T \qquad (12)$$

3.1.4 Conservation of Energy

Conservation of energy is presented in equation 13 [20].

Conservation of energy:

$$\frac{\partial(\rho E)}{\partial t} + \boldsymbol{\nabla} \cdot (\rho E \boldsymbol{v}) = \boldsymbol{f_b} \cdot \boldsymbol{v} + \boldsymbol{\nabla} \cdot (\boldsymbol{v} \cdot \boldsymbol{\sigma}) - \boldsymbol{\nabla} \cdot \boldsymbol{q} + \boldsymbol{S_E} \quad (13)$$

Where:

E = total energy per mass unit.

$\boldsymbol{q}$ = heat flux.

$\boldsymbol{S_E}$ = energy source per unit volume.

When integrating the equation for conservation of energy, equation 13, over a finite control volume, the equation can take the following form, equation 14. This is used by the STAR-CCM+ solver [21].

Conservation of energy:

$$\frac{\partial}{\partial t}\int_V \rho E dV + \oint_A \rho H \boldsymbol{v} \cdot d\boldsymbol{a} = -\oint_A \dot{q}'' \cdot d\boldsymbol{a} + \oint_A \boldsymbol{T} \cdot \boldsymbol{v} d\boldsymbol{a} + \int_V \boldsymbol{f}_b \boldsymbol{v} dV + \int_V S_E dV \quad (14)$$

3.2 The Main Methods for Numerical CFD Simulations

There are three main methods for solving turbulent flows numerically. These are Direct Numerical Simulation, Large Eddy Simulation and Reynolds-averaged Navier-Stoker. For this work, RANS is used and therefore described in detail. The other methods require a short explanation for perspective and as an argument to why the RANS method was chosen.

3.2.1 Direct Numerical Simulation (DNS)

In DNS the conservation equations for mass, momentum and energy are solved directly without any models for turbulence. The turbulence scales are resolved directly from the initial and boundary conditions. DNS can resolve very fine detail, but this requires a very fine grid and very small time-scale for each step. The grid must be finer than the Kolmogorov length scale [22]. The Kolmogorov scale is the smallest scale in turbulent flow. Viscous forces dominate, and the turbulent kinetic energy is dissipated by conversion into heat. The Kolmogorov scale can be defined for length, time and velocity [19]. Because of the very fine resolution needed, the DNS approach is extremely demanding on computational power and only used when very high accuracy is required and the resources for this are available.

3.2.2. Large Eddy Simulation (LES)

In the LES method, the large turbulent eddies are solved directly, and the smaller eddies are filtered. The smaller eddies can be the most demanding to resolve with regards to computational power, so models are used for these instead of direct solvers [22]. To accurately capture details with the LES method the resolution of the model can be larger than the Kolmogorov length scales. The maximum coarseness of the grid must still be finer than the Taylor microscale to be able to capture the large eddies [23]. The Taylor microscale is the length scale at which viscosity affects the eddies to a significant degree [19]. With more computer power becoming readily available, LES methods are increasingly common. The LES approach can be viewed as an intermediate between the computationally intensive DNS and the least intensive RANS method [22].

3.3 Constitutive Laws

3.3.1 Reynolds-averaged Navier-Stokes (RANS)

The RANS method is the most common approach for numerical CFD simulations. It is the least demanding on computational power and for engineering purposes, it can provide solutions that are adequate in accuracy. With the computing power available today RANS is a good compromise, making CFD simulations more readily available.

In the RANS method, the instantaneous Navier-Stokes equations are solved for mean values for all quantities. This approach to the conservation equations for mass, momentum and energy requires models to bring closure to the various terms. For turbulent reacting flows, the following are minimum requirements [9]:

1) A turbulence model for the flow. One such model is the K-Epsilon viscosity model.
2) A turbulent combustion model for tracing chemical species and heat release. One such method is the Steady Laminar Flamelet model.

To bring closure to the terms in the transport equations with the RANS method, each quantity in the instantaneous Navier-Stokes equations are decomposed into two components. One is the average value and one is a fluctuation value. These quantities are scalars such as velocity components, pressure, energy or species concentration. For steady-state simulations the averaging is time-averaged. By inserting the decomposed averaged components into the fundamental equations for conservations of mass, equation 7, and linear momentum, equation 9, these transport equations can be written as shown in equations 15 and 16 [24].

Mean conservation of mass:

$$\frac{\partial \rho}{\partial t} + \boldsymbol{\nabla} \cdot (\rho \overline{\boldsymbol{v}}) = 0 \qquad (15)$$

Mean conservation of linear momentum:

$$\frac{\partial}{\partial t}(\rho\overline{\boldsymbol{v}}) + \boldsymbol{\nabla}\cdot(\rho\overline{\boldsymbol{v}}\otimes\overline{\boldsymbol{v}}) = -\nabla\cdot\bar{p}\boldsymbol{I} + \nabla\cdot(\boldsymbol{T}+\boldsymbol{T}_t) + \boldsymbol{f_b} \qquad (16)$$

Where:

$\overline{\boldsymbol{v}}$ = mean velocity.

$\bar{p}$ = mean pressure.

I = identity tensor.

T = viscous stress tensor.

$\mathbf{f_b}$ = resultant of body forces.

The mean conservations of mass, equation 15, and mean conservations of linear momentum, equation 16, are very similar to the fundamental equations for conservation of mass, equation 7, and conservation of linear momentum, equation 9. An additional term is added to the momentum equation. This term is known as the Reynolds Stress Tensor ($\mathbf{T_t}$). This tensor defines viscosity with regards to mean velocity in three dimensions and is needed for to bring closure to the instantaneous Navier-Stokes equations. Furthermore, to solve the Reynold Stress Tensor an additional model is required. One such model is the K-Epsilon Eddy Viscosity Model [24].

Reynolds Stress Tensor:

$$\boldsymbol{T_t} = -\rho\begin{pmatrix}\overline{u'u'} & \overline{u'v'} & \overline{u'w'}\\ \overline{u'v'} & \overline{v'v'} & \overline{v'w'}\\ \overline{u'w'} & \overline{v'w'} & \overline{w'w'}\end{pmatrix} \qquad (17)$$

Where:

$\bar{u}$, $\bar{v}$ and $\overline{w}$ = mean velocity components.

3.3.2 K-Epsilon Eddy Viscosity Model

One approach to resolving the Reynolds Stress Tensor in STAR-CCM+ is performed through various Eddy Viscosity Models. In these models, turbulent eddy viscosity (μ_t) is used to solve the Reynolds Stress Tensor, as a function of mean flow. The most common model is called Boussinesq approximation [25].

Boussinesq approximation:

$$\boldsymbol{T_t} = 2\mu_t \boldsymbol{S} - \frac{2}{3}(\mu_t \nabla \cdot \overline{\boldsymbol{v}})\boldsymbol{I} \quad (18)$$

Where:

S = mean strain rate tensor.

Boussinesq approximation assumes that the Reynold Stress Tensor us linearly proportional to the mean strain rate. However, this does not consider the anisotropy of turbulence. To account for this aspect of turbulence the eddy viscosity models solve additional transport equations for scaler quantities to derive the turbulent eddy viscosity. Several two-equation models are available in STAR-CCM+. For the RANS simulations in this thesis the K-Epsilon model for eddy viscosity is used. [25].

The K-Epsilon turbulence model solves transport equations for two scalars, the turbulent kinetic energy (K) and the turbulent dissipation rate (Ɛ). There are several possible approaches to K-Epsilon turbulence models; A high Reynolds number approach, a low Reynolds number approach and a two-layer approach. In addition, there is the standard K-Epsilon and there is the realizable K-Epsilon approach. The realizable approach adds a critical coefficient to the model that is expressed as a function of mean flow and turbulence properties. This is assumed constant in the standard approach. The realizable approach is better than the standard approach for many applications [26].

For the RANS simulations in this thesis, the two-layer approach has been selected. In this approach, the computation is divided into two layers. They layer closest to the wall treats the turbulent dissipation rate and the turbulent eddy viscosity as a function of wall distance. The values are blended smoothly with the values for these scalars in the computational domain far from the wall. The turbulent kinetic energy is solved across the entire flow domain. This two-layer approach works best in STAR-CCM+ for y^+ values below 5 or above 20. The interim y^+ area is preferably to be avoided [26].

High y^+ typically translates to a course mesh with few boundary layers. This is the classic wall-function approach in the original K-Epsilon turbulence model and requires a high Reynolds number for the flow. Wall shear stress, turbulence production and turbulence dissipation are all derived from equilibrium boundary layer theory [27].

Low y^+ typically translates to a fine mesh with many boundary layers, meaning that the viscous sublayer is well resolved by the mesh. This is important if heat transfer across boundary layers is to be considered [27].

For the STAR-CCM+ solver, this translates to either using a small number of boundary layer cells, two to three, or a high number of boundary layer cells, eight and above, depending on the characteristics of the flow and the geometry of the area in question. The interim region between a small number of boundary layers and a high number of boundary layers should preferably be avoided for the solution to provide accurate results.

Initialization of the K-Epsilon model is provided by boundary conditions specified at the boundaries of the model [28]. For the models in this thesis these boundary conditions are specified by turbulence intensity and turbulence length scale. The absolute values of these scalars are unknown, but a value was selected based on common practice. The selected values are provided under boundary conditions

in the model description, sections 3.7.4.1-2. To allow for a fully developed flow to be established before the fluids enter the computational domain of interest, the inlets and outlet have a length of eight times the diameter prior to entering the combustor and after exiting the combustor.

3.3.3 Reacting Turbulent Flow

A reacting flow in STAR-CCM+ is when chemical species mix and then react when conditions allow for the reactions to take place. Such flows are modelled by coupling species with energy transport equations and chemistry solvers.

A reacting flow starts with reactants that mix and form intermediate species. The intermediate species again react with the reactants and other intermediate species, until relatively stable end products are reached. In reacting flow the timescales can vary greatly [29], depending on the species participating in the reactions in question, the turbulence, mixing quality, temperature, pressure and other variables. Thus, most reacting flows are computed using models that simplify the process and the computing power required.

Combustion in a turbulent flow is a two-way interaction between chemistry and turbulence. Turbulence is modified by the combustion due to the acceleration of the flow induced at the flame front by the heat release. The turbulence generated is called flame-generated turbulence. On the other hand, the structure of the flame is affected by the turbulence. The turbulence may enhance the chemical reactions but can also quench the flame in extreme cases [9].

The Damköhler number is an important non-dimensional number in reacting flows. It indicated the ratio between the physical timescale (T_{phys}) of the turbulence and the chemical timescale (T_{chem}) of the chemical reactions [9].

Damköhler number:

$$Da = \frac{\tau_{phys}}{\tau_{chem}} \qquad (19)$$

Various definitions of these timescales exist. Especially the chemical timescale can be hard to define. The chemistry of combustion has many intermediate stages, where some reactions are fast while others are slow. In addition, the concentrations of the species change during the reactions which again affects the timescales. As a guideline, the chemistry is very slow compared to the turbulence if the Damköhler number is much smaller than 1. If it is much larger than 1, the chemistry is much faster than the turbulence. However, in real chemistry, a combination of timescales exists. One such example is the formation of NO_x emissions. The combustion process itself may be defined as fast, but the formation of NO_x can be slow [9]. For simulation purposes, the Damköhler number serves as a criterium for determining the right combustion model for the simulation case.

3.3.4 Complex Chemistry with Chemical Mechanisms

STAR-CCM+ includes a library of common fluids and gasses with material properties for simulation purposes. For these, stochiometric reactions need to be defined for simple simulations. However, combustion chemistry is complex, and the entire reaction goes through many sub-reactions that include sub-species with different reaction rates, timescales, chemical and energy equilibriums. Not all the reactions are completely understood and have not been thoroughly researched.

STAR-CCM+ incorporates the ability to import complex chemical mechanisms into the software. These mechanisms cover some of the important sub-species and sub-reactions needed for more accurate results than the built-in library provides. These mechanisms are significant for the prediction of the formation of pollutants such as CO and NO_x. The combustion mechanisms serve as the basis for the creation of Flamelet tables in the case of Flamelet methods being used.

There are several chemical mechanisms available that include the oxidation of propane:

1) The San Diego Mechanisms developed by the Combustion Research Group at University of California San Diego. The latest revision is dated 14.12.2016.
2) AramcoMech2.0 developed by the Combustion Chemistry Centre at National University of Ireland Galway. The latest revision is dated 2016.
3) GRI-Mech 3.0 developed by the Gas Research Institute (GRI) developed by The University of California at Berkeley, Stanford University, The University of Texas at Austin, and SRI International.
4) Mechanisms developed by the Combustion Kinetics Laboratory at University of Southern California et al.
5) Various attempts at making more lightweight chemical reaction mechanisms that require less computational power yet yield accurate results.

The Mechanisms developed at the University of Southern California by Wang et al. [30] are from the year 2000 and seem to have been incorporated and surpassed by later mechanisms such as GRI-Mech 3.0. GRI-Mech 3.0 is commonly used for research and engineering purposes. However, the mechanisms are focused on the combustion of natural gas and are designed to only handle propane as a minor species. Thus GRI-Mech 3.0 complex chemistry is not suitable for propane only combustion simulation. There are two recognized mechanisms that include the oxidation of propane as a major species. These are the San Diego Mechanisms and AramcoMech2.0. Both have been updated in 2016 and both mechanisms have been used by researchers to develop lighter mechanisms, aimed at reducing the computational power needed for CFD with species transport models. In species transport, the chemical reactions are computed directly for each node in the computational domain, which is very demanding on computational power. Such efforts are described by Lin et al. [31]. These efforts strengthen the validity of both the San Diego and the AramcoMech2.0 mechanisms. The San Diego mechanisms contain 57 species and 268 reactions. The AramcoMech2.0 contains 493 species and 2716 reactions. Flamelet tables were generated with both mechanisms. As expected, the San Diego mechanisms were significantly less demanding on computational power and therefore chosen for this work.

3.3.5 Flamelet Methods

To deal with the second requirement for solving the transport equations with the RANS method a combustion model is needed. The purpose of the combustion model is to close the term for the mean reaction rate for a given chemical species in the conservation of mass equations. The mean reaction rate is described by $\dot{\omega}_k$ in the equation for conservation of species k, equation 6.

One such combustion model is the Flamelet method. There are different Flamelet methods that deal with various types of combustion such as premixed and non-premixed. These Flamelet models are however only valid when the chemical reaction timescale is smaller than the physical turbulence timescale [29]. This equates to a high Damköhler number and translates to the chemical reactions being unaffected by the turbulence. In simplified terms, the turbulent flow only serves as a transport that moves the chemical reaction without affecting the reactions.

In STAR-CCM+ the combustion with the Flamelet method is pre-calculated prior to simulation and generated into a Flamelet table with customizable resolution. During simulation, the solver collects the pre-generated scalars from the Flamelet table and insert these values into the solver. This method allows for much faster computing times than resolving a complete set of chemical reactions for each node in the mesh.

According to the STAR-CCM+ documentation, the Flamelet method is suitable for steady-burning devices such as gas turbine combustors running at full load conditions. Flamelet models are however not suited for combustors with dynamically changing loads, changing environmental conditions and transient combustion simulation with effects such as flame extinction and re-ignition [29].

3.3.5.1 Steady Laminar Flamelet (SLF) for Non-premixed Combustion

In STAR-CCM+ several Flamelet methods are supported. For this thesis, SLF is chosen because the combustion process to be simulated if of a non-premixed nature. The oxidiser and fuel are supplied into the combustion chamber through separate feed lines, one for the oxidiser and one for the fuel. The mixing of the species happens in the combustion chamber itself and the combustion is a diffusion flame.

In the Steady Laminar Flamelet, combustion is a function of the mixing fraction (Z) and a probability density function (PDF). In the RANS method, there is a mean mixture fraction in addition to a mixture fraction variance (Z_{var}) that needs to be solved. The sum of all the species at any given mixture fraction is always one and the variance is treated as the mixture fraction minus the variance.

The concept of starting the combustion process by ignition does not exist in the SLF combustion model. Combustion is purely a function of the mixture fraction and variance. No ignitor is needed in the numerical model.

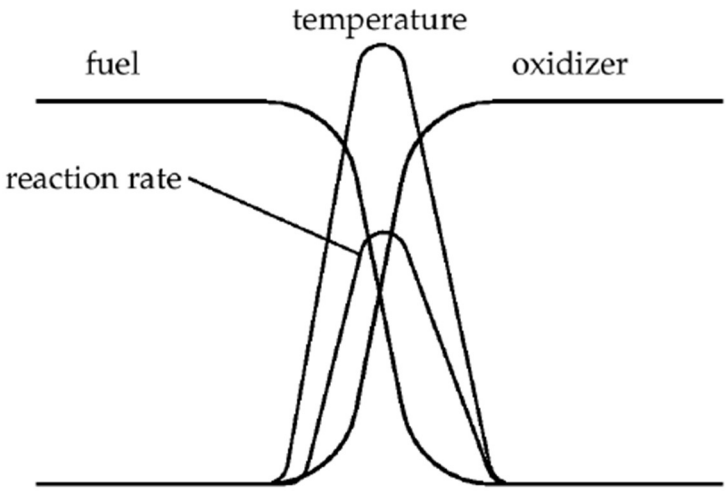

Figure 5: *This figure shows the principle of combustion with a laminar diffusion flame. Fuel, oxidiser, reaction rate and temperature are linked. Image courtesy of [22].*

3.3.6 The Steady Laminar Flamelet Table

The Steady Laminar Flamelet table is generated by the software from the San Diego mechanisms imported into STAR-CCM+. Default settings were used, except for the listed parameters.

Fluid Streams:

Oxidiser:

Fluid Stream Components:	N_2 = 0.767
	O_2 = 0.233
Composition Specification:	Mass Fraction
Temperature:	387.05 K

Fuel:

Fluid Stream Components:	C_3H_8 = 1.0
Composition Specification:	Mass Fraction
Temperature:	318.15 K

Parameters:

Absolute Pressure:	101325.0 Pa
Species for Tabulation:	C_3H_8, CO, CO_2, H_2O, N_2, O_2
Emissions:	Thermal NO_x (for use in the NO_x emissions model)

The SLF table was generated using 202 grid points for mixture fraction, 31 points for mixture fraction variance and 14 points for scalar dissipation rate. Non-adaptive gridding was used to keep the error rate below 1 %. This comes at the cost of longer computational time for the table generation and a larger file size for the combustion table.

To check the validity of the chemical mechanisms used, two additional tables were generated. One table for the oxidiser and fuel with 298.15 K temperature at 1.0 bar absolute pressure and one table for the oxidiser and fuel with 343.0 K temperature at 1.0 atm. absolute pressure. The first table uses input values from Law [32] and the second table from Gong et al. [33]. Since the graphs below are generated from the same chemical mechanisms and SLF table setting, they track very similarly. The pressure differences are negligible. The graphs are only affected by the difference in oxidiser and fuel temperatures. A detailed view of the top of the same graph is provided in figure 7.

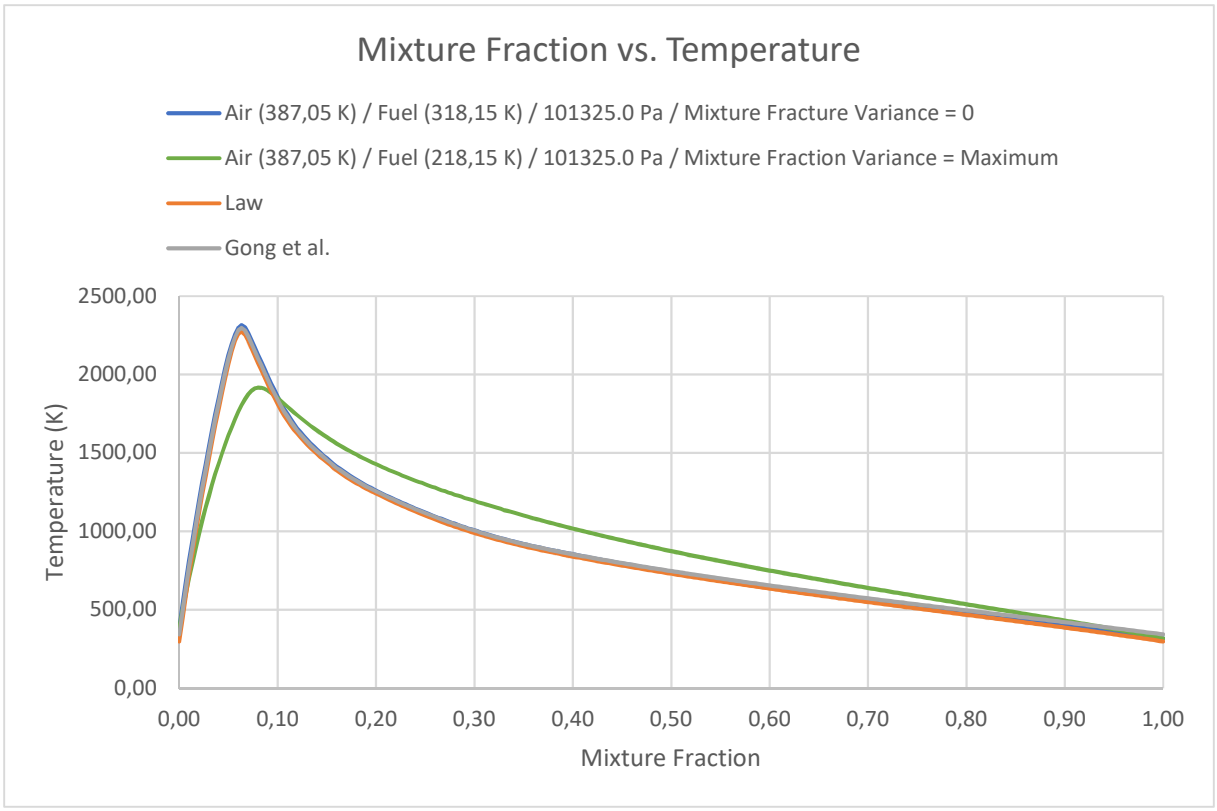

Figure 6: *This figure shows the graphs for mixture fraction versus temperature plotted for three different oxidiser- and fuel stream temperatures. The pressure differences are negligible. Also, note the lower and upper temperature limits created by the mixture fraction variance. Any reaction temperature will be within these boundaries for a given mixture fraction.*

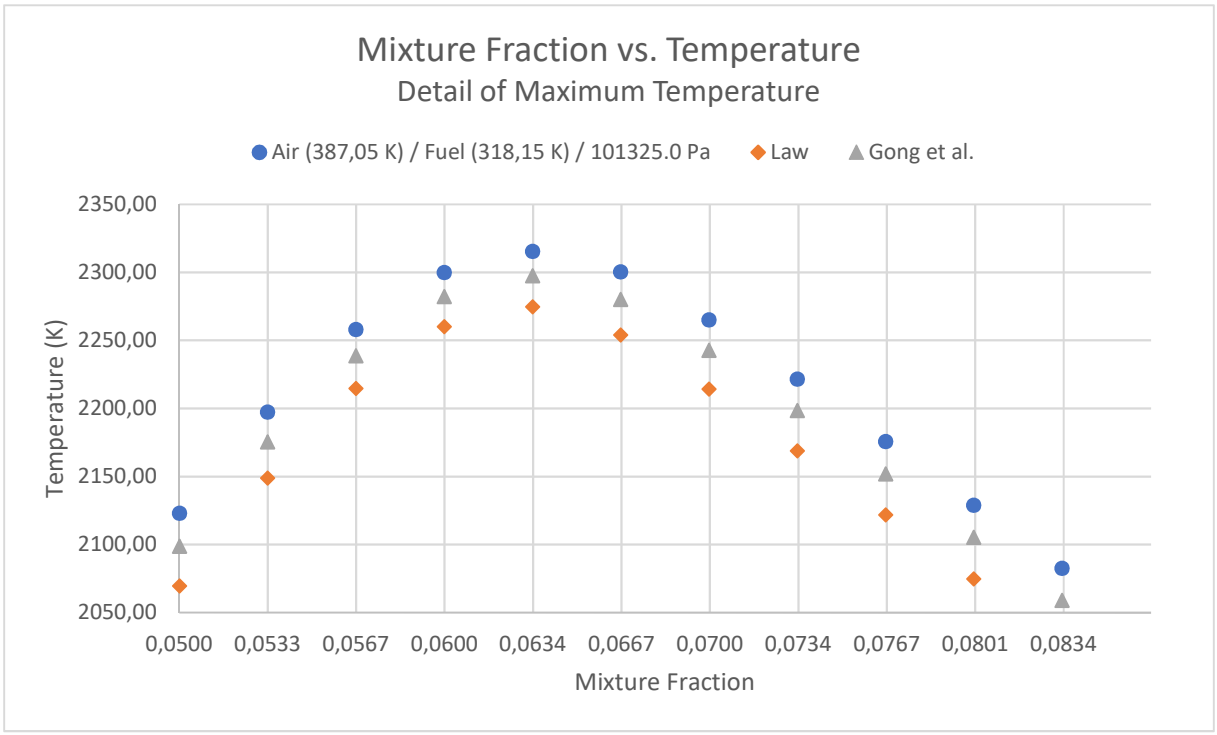

Figure 7: *The figure shows a detailed view of the top of the mixture fraction versus temperature plotted in figure 6.*

Calculations, equation 28, shows that the peak temperature should occur at a mixture fraction of approximately 0.0602 at reference conditions for temperature and pressure. Reference temperature for oxidiser and fuel is 298.15 K and 1.0 bar [7]. The detailed view of the top of the SLF tables graphs shows that there is no data point for this exact position for Z in the SLF table. However, the table has good resolution with data points for Z at 0.0600, 0.0633 and 0.0667. The peak temperature occurs in the SLF tables at mixture fraction 0.0633. This is a deviation of approximately 1.8 % for mixture fraction. A doubling of grid points for mixture fraction would provide data for a point at 0.06165 which would be even closer. 202 points were however considered adequate for this simulation and within an acceptable margin of error. The temperature deviation between SLF table values and values collected from literature is also within acceptable error, showing a maximum error of 1.82 %. This is shown in table 3.

Table 3: *The table shows the maximum temperature at stoichiometric combustion from literature versus temperature from STAR-CCM+ generated SLF tables.*

	Reference temperature	**Reference pressure**	**Maximum temperature from literature**	**Maximum temperature SLF table**	**% Temperature deviation**
Law [32]	298.15 K	1.0 bar	~2235 K	2275.75	~1.82%
Gong et al. [33]	343 K	1.0 atm	~2305 K	2297.62	~0.03%
SLF table for this work	Air: 387.05 K Fuel: 318.15 K	101325.0 Pa	-	2315,56	-

The species selected for tabulation are plotted in figure 8. The plot shows the change in the mass fraction of the species as the mixture fraction develops. A mixture fraction of zero corresponds to pure oxidiser as defined in the oxidiser stream. For this case that is an oxygen and nitrogen mixture corresponding to air. A mixture fraction of one corresponds to pure propane fuel. The graph shows the development of species with the change in mixture fraction. The graph is plotted with mixture fracture variance set to zero. It was also plotted with the maximum mixture fraction variance. The figure can be found in the appendix.

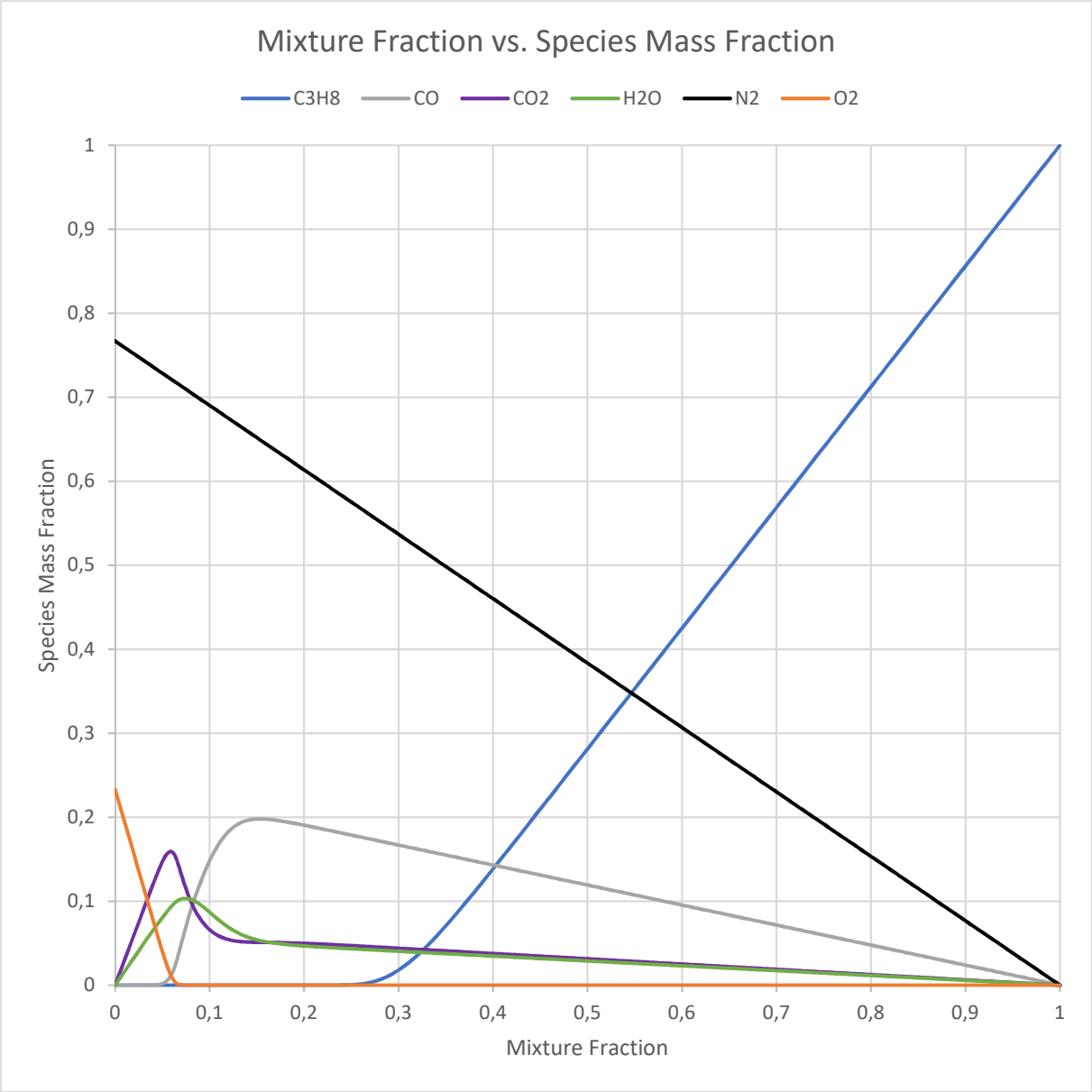

Figure 8: *All species selected for tabulation in the SLF table. The sum of all mass fractions for the species at a given mixture fraction totals to one. The values for mixture fraction are plotted with mixture fraction variance set to zero.*

The formation of NO_x is also an engineering scalar of interest, but these are not selected for tabulation. NO_x formation has a long reaction rate timescale compared to the timescale of the turbulence in the reacting flow. This corresponding to a low Damköhler number. The Flamelet method is therefore not suitable by itself for predicting NO_x. Separate NO_x models have been developed for STAR-CCM+ for this purpose and are activated as a model. The species of NO_x do not exist in the SLF table as plotted in figures 8 and 9.

Figure 8 is a smoothed graph, so it is important to check the resolution of the data points. This is especially critical in the narrow bands for mixture fraction were the species have steep gradients. This is to make sure that the generated table has adequate resolution to track rapid changes in species mass fraction as a function of a small change in mixture fraction. If the species mass fraction development is not adequately resolved a new Flamelet table must be generated with additional data points to capture the changes. As can be seen in figure 9 the 202 grid point resolution for mixture fraction adequately captures the changes in the species selected for tabulation.

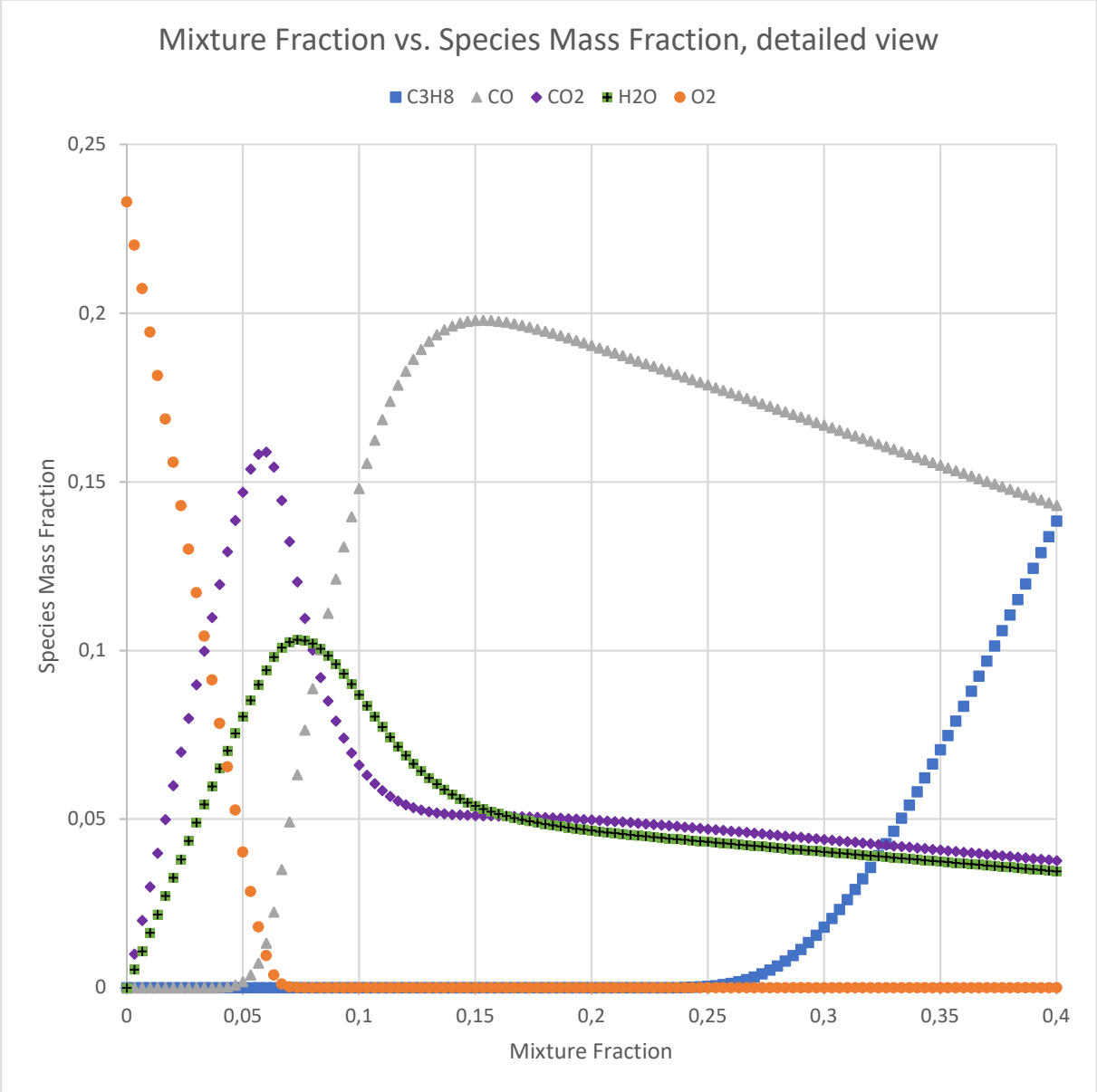

Figure 9: *A detailed view of a part of figure 8. Small changes in mixture fraction can have a significant impact on species mass fraction. The resolution of the data points is adequate to capture these changes.*

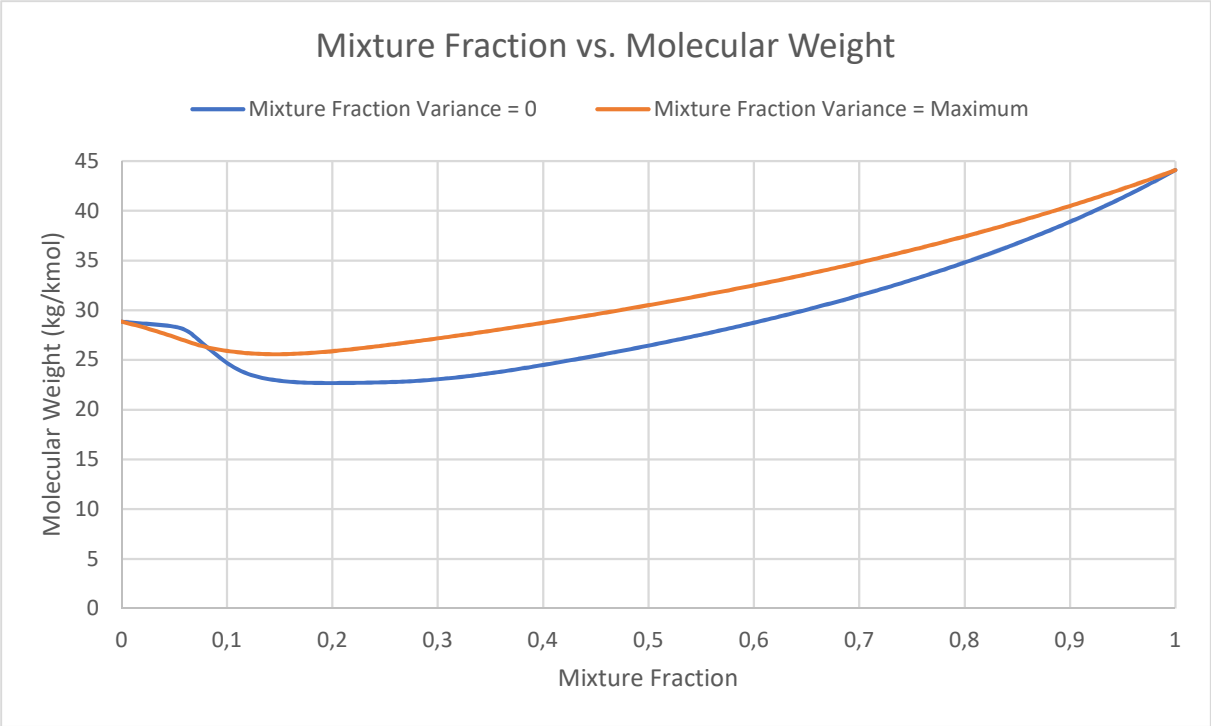

Figure 10: *The figure plots the molecular weight of the reacting flowing in the SLF table with regards to mixing fraction. Note that a mixture fraction of zero corresponds to the air mixture as defined in the oxidiser stream and a mixture fraction of one to pure fuel as defined in the fuel stream.*

Considering that the San Diego complex chemistry mechanisms used are well established and recognized as credible for propane combustion, and that the plots from the table for temperature, species mass fraction, grid resolution and molecular weight are credible, I have concluded that the SLF table can be considered accurate for the use in the CFD simulation work of this thesis.

3.3.7 Boundary Conditions

3.3.7.1 Mass Flow Inlet

Mass flow inlets in STAR-CCM+ can be considered either incompressible or compressible. The following variables are input by the user for mass flow inlets:

- Total mass flow rate ($\dot{m}$).
- Supersonic static pressure (P_S^{ext}). The supersonic static pressure is only available for compressible flows.
- Total temperature (T_t).
- Inflow direction.

The software computes the following values for the mass flow inlet boundary face [34]:

- The mass flux is evenly distributed over the boundary face of the mass flow inlet.
- Static pressure (P_S).
- Velocity (**v**).
- Static temperature (T_S).

3.3.7.2 Wall Conditions

At the wall boundary faces STAR-CCM+ computes the wall static pressure (P_S), wall fluid velocity (**v**) and wall static temperature (T_S). The static pressure at the wall boundary face is extrapolated from the interior domain [35].

Static pressure at wall boundary: $$P_S = P_S^{ext} \quad (20)$$

The walls in the simulation are treated as non-slip walls. The wall fluid velocity for non-slip wall conditions specifies that the fluid at the wall moves with the same velocity as the wall. The fluid velocity relative to the wall velocity is zero.

The wall static temperature is set to adiabatic. This does not allow for heat transfer across the boundary. The fluid temperature, density and total enthalpy at the wall are extrapolated from the interior of the fluid domain and not affected by the external side of the wall boundary [35].

The fluid temperature at wall boundary: $$T_S = T_S^{ext} \quad (21)$$

The fluid density at wall boundary: $$\rho = \rho^{ext} \quad (22)$$

The fluid total enthalpy at wall boundary: $$H_t = H_t^{ext} \quad (23)$$

3.3.7.3 K-Epsilon Wall Treatment (Wall y^+)

The purpose of wall treatment in the K-Epsilon model is to specify a value for the reference velocity (u*) and to compute a value for turbulent production (G_k) and turbulent dissipation rate. The concept of wall y^+ is commonly used in the theory of boundary layers. It describes the relationship between the reference velocity and the distance to the wall. Wall y^+ is a dimensionless number [36].

Wall y^+: $$y^+ = \frac{u^* y}{\nu} \quad (24)$$

Where:

u* = reference velocity.

y = distance to nearest wall.

ν = kinematic viscosity.

When using the K-Epsilon model in STAR-CCM+ the turbulent production, turbulent dissipation and reference velocity are calculated differently based on the wall treatment model selected [36]. It is therefore important to mesh the boundary layer so that it corresponds to the wall treatment model. Both high y^+ and low y^+ options are available. There is also a hybrid model available called all y^+, which is the one used for this work. This model gives an accurate result for both high and low y^+, although there is an intermediate zone for y^+ from approximately 5 to 30 that should be avoided. This corresponds to a blended region between the linear development of velocity relative to wall distance

in the viscous sublayer, the lower boundary layer, and the logarithmic development of velocity and wall distance in the upper boundary layer. The relationship between velocity relative to wall distance in the intermediate zone is difficult to describe accurately mathematically and should be avoided [37].

3.3.8 Ideal Gas

For this simulation work, the fluid is treated as an ideal gas.

3.4 Siemens Simcenter STAR-CCM+

The main body of work in this thesis is a numerical study of turbulent reacting flows. For this work Siemens Simcenter STAR-CCM+ software is used. The software can model a wide range of physical phenomena, including fluid mechanics, chemical reactions and heat transfer. The mathematical models in the software that describe the physics are derived from the fundamental conservation principles. An Eulerian implementation is chosen, meaning that the control volume represents a portion of space where material can flow through [20].

The fundamental equations are presented in a differential form for an infinitely small control volume. These partial differential equations cannot be solved directly, because the total number of unknowns exceed the number of equations. To solve these equations the various terms in them need to be closed. To provide this closure additional equations are needed. These are the constitutive laws and are supplements to solve the partial differential equations [20].

To obtain a solution the software uses discretization. The simulation domain is divided into a finite number of subdomains called cells. Together these cells form a mesh. The unknowns to be computed are stored for a specific location of the mesh; in cell centroids, in face centroids, vertices and edges. These form sets of discrete algebraic equations that can be solved using finite volume methods [20].

The software generates the mesh of cells by first populating the walls of the geometry and then growing the volumetric cells from the surface. The Surface Remesher is used to provide this base layer on the surfaces. The critical boundary layers are generated by the Prism Layer Mesher and the surface cells serve as a basis for this. The prism layer cells are mostly rectangularly in shape, with customizable size, aspect ratio and growth rate, depending on the needs for computing the boundary layer effects. The remaining volume is populated by the Polyhedral Mesher. The polyhedral cell is a many-faced cell that is favoured by the software for reasons of computing power [38]. It is worth noting that other specialized meshers also are available, though not used in this work.

3.5 Software and Hardware

All simulations were performed with Siemens PLM Software Simcenter Star-CCM+ version 13.02.011 for Microsoft Windows with single precision. The converged solutions were also run on the double precision version of the software to check if convergence could be improved. This did not yield any improvement in convergence or reduction in residuals. It did increase the solver time per iteration significantly. The single precision software was thus deemed suitable for this study.

All simulations ran on a dual Intel Xeon CPU setup with 12 cores per CPU to a total of 24 cores. Each core ran at 2.7 GHz. 23 cores were used by the solver. The last core was available for other tasks. The system used 64 GB ECC RAM running at 2133 Mhz speed. More than 800 hours of simulation time has been performed in this work.

3.6 Workflow for Convergence

To achieve convergence in CFD, the model must be of a certain quality. There are several crucial factors that need to be considered to achieve this. My workflow has been as listed below. Each point will be discussed in more detail for the simulation cases.

Workflow:

1) Geometry creation.
2) Physics setup.
3) Initial conditions setup.
4) Boundary conditions setup.
5) Mesh creation.
6) Mesh quality check and improvement.
7) Initiate the simulation and run for a reasonable number of iterations.
8) Check the boundary layer wall y^+ values and improve mesh quality of needed.
9) Setup the monitors and plots for values of interest.
10) Run the simulation until convergence is achieved.
11) Perform mesh sensitivity analysis with various mesh sizes.
12) Extract results from simulation.

3.7 Case 1: CFD Setup

Case 1 is the numerical simulation of the existing combustor that is installed in the faculty gas turbine engine. The purpose of this simulation is to setup, run, validate the model and examine the results for the existing design. This is a steady state simulation of non-premixed combustion using RANS with the K-Epsilon model and the Steady Laminar Flamelet model for combustion.

3.7.1 Geometry

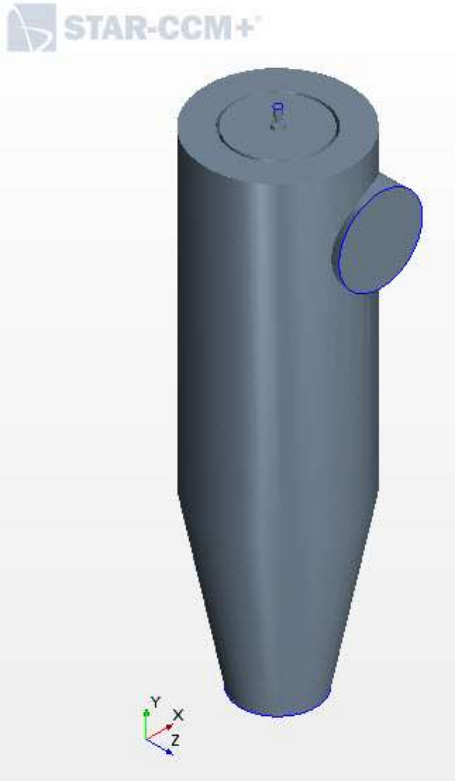

Figure 11: *The figure shows an isometric view of the fluid volume of the combustor. The fuel inlet is centred on the top and the air inlet off-centred towards the positive X-direction. A small gap can be seen between the flame tube fluid volume and the liner fluid volume. This is the 2 mm thick walls of the flame tube.*

This paragraph presents the geometry of the model as created with the built-in CAD module of STAR-CCM+. The model represents the fluid volume of the existing combustor as built by Mjølhus and Andreassen in 2012 [10] as closely as possible. It is based on the 2D CAD drawings and specifications presented in their thesis.

The combustor is a silo type combustor with fuel injection centred on the top of the combustor and the compressed air entering from the side. The hot exhaust gasses are ejected from the bottom of the combustor with only a short clearing distance to the turbine required by the thickness of the flanges that connect the combustor and the turbine inlet.

The fuel is supplied by a 6.3 mm inner diameter flexible hose. The hose is connected to a nozzle with 3 mm internal orifice. The nozzle is obtained from a Sievert model 294302 gas burner. The exact internal shape of the nozzle is not known in detail, thus the shape in the model is a close approximation. The nozzle is screwed onto the top of the combustion chamber. The compressed air is supplied through a 72 mm inner diameter 316L stainless steel pipe. The pipe is welded onto the combustor with the centre of the pipe 66 mm below the fuel injection nozzle. The pipe is offset to one side of the vertical centreline of the combustor by 22 mm, a design choice that makes CFD simulation more CPU-intensive as there are no possible symmetry planes.

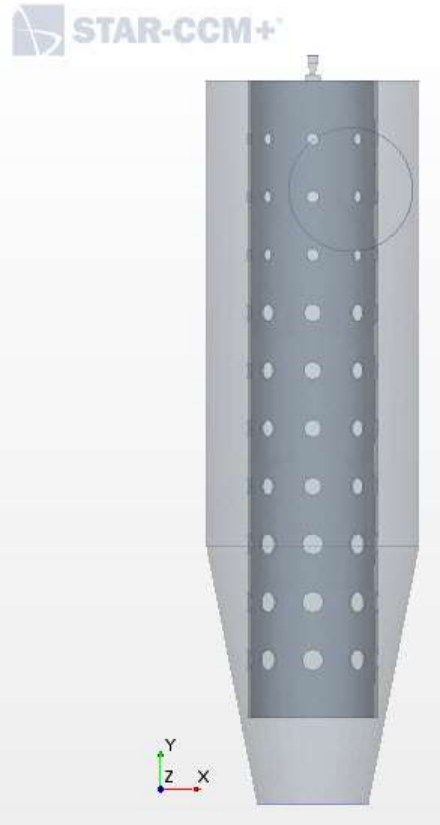

Figure 12: *The figure shows an isometric transparent view of the combustor fluid volume. The purpose of this figure is to illustrate the perforated flame tube. The air inlet is shown in the positive Z-direction facing outwards.*

The combustor itself is made from two 316L stainless steel pipes, one with an inner diameter of 72 mm and the second with an inner diameter of 124 mm. The inner pipe has a length of 370 mm and a thickness of 2 mm. The outer pipe has a total length of 420 mm. At 270 mm in negative Y-direction, the pipe was cut and bent inwards, reducing the internal volume into the shape of a converging nozzle. The nozzle section of the outer pipe has a length of 150 mm and reduces the diameter from the original inner diameter of 124 mm to 65 mm. This is the outlet diameter of the combustor.

The outer pipe serves as the combustor casing and the inner pipe as the wall for the flame tube. The inner pipe is perforated by 10 rows of circular holes spaced evenly along the length of the pipe. Each row consists of 8 holes spaced evenly circumfixing the pipe. The holes in rows 1 to 3 have a diameter of 7 mm, rows 4 to 7 a diameter of 10 mm and rows 8 to 10 have 12 mm diameter. As seen in figure 12, there is also a small gap between the bottom of the flame tube and the liner/outer wall.

For model convergence purposes the fuel inlet, air inlet and the exhaust outlet were extended outwards to a length of 8 times the diameter. This feature is not in the real-world combustor but was done to ensure that a proper flow profile was established in the simulation prior to the fluids entering the combustor. This would also prevent backflow at the combustor outlet.

3.7.2 Active Models

This paragraph provides an overview of the active models that were used in the STAR-CCM+ simulation. This is important to include to understand the basis of the simulation and its limitations. The models are listed alphabetically below. Default values were used unless otherwise specified.

Active models:

Cell Quality Remediation	Non-Premixed Flame
Exact Wall Distance	Reacting
Flamelet	Realizable K-Epsilon Turbulence
Gradients	Reynolds-averaged Navier-Stokes
Ideal Gas	Segregated Flow
K-Epsilon Turbulence	Segregated Fluid Enthalpy
Multi-Component Gas	Steady
NO_x Emissions	Steady Laminar Flamelet
NO_x Prompt	Three Dimensional
NO_x Thermal	Turbulent
NO_x Zeldovich	Two-Layer All y+ Wall Treatment
Non-Adiabatic	

3.7.2.1 NO_x Emissions Model

The NO_x emissions models were set to activate after 1,000 iteration. The engineering scalars in the simulation will fluctuate in the first steps as the simulation calculates the fluid movement from the boundaries into the simulation domain. The flows are initially affected by the initial conditions of the fluid domain and this will cause results to fluctuate before reaching steady state. Because this is a steady state simulation there is no effect in activating the NO_x emissions models at the start of the simulation, because the emissions will be calculated from scalars that are far from converging. This also saves CPU solver time in the initial steps.

3.7.2.2 Simplifications

There are several models available in STAR-CCM+ that could have been activated for this simulation case. As for all models, these come at the cost of additional computational time. Some of the models also require user settings for which data was not available. The model was simplified by omitting the following physics:

1) Soot model; Soot formation was not to be examined in this thesis
2) Radiation; No radiations models were activated due to the computational cost and the uncertainty of the user input variables. Radiation can cover both radiation inside the simulation domain and external radiation to the environment. Dissipation of energy in the form of radiation from the combustor to the environment was not to be considered.
3) Conjugate Heat Transfer; Heat transfer through solids such as the wall of the flame tube was omitted from this simulation. Conjugate Heat Transfer in STAR-CCM+ requires the modelling of the solid material with its own separate models, material properties and mesh with interfaces between the fluid volume and the solid volume. This was attempted but attaining a good mesh and a good interface was too time-consuming to be covered in this thesis.
4) Convection; Heat transfer by convection from the combustor to the environment was also not considered due to limited available data.

3.7.3 Initial Conditions

For a steady-state simulation, the initial conditions should be set in such a way that they are not too far from the expected results. Steep gradient between initial conditions, boundary conditions and expected results can cause the simulation to diverge and cause a floating-point calculation error in the solver. The initial conditions can also affect the number of iterations needed to reach convergence and steady state.

The expected results for the simulation are however not uniform across the entire fluid domain, so choosing parameters for initial conditions must be weighted. Scalars such a temperature and velocity will vary greatly based on location in the simulation domain. For this simulation initial conditions reflecting the real-world physical setup were chosen. The initial conditions used are presented in table 4. These initial conditions proved to be within an acceptable range from the boundary conditions and the results. The solver did not diverge.

One challenge at the start of the simulation was that the mixture fraction was set to 0.0 for the entire domain. This translates to pure oxidiser, in this case an oxygen and nitrogen mixture corresponding to air. These initial conditions filled the entire fluid domain, including the fuel inlet pipe. As the simulation starts pure fuel enters the fuel inlet boundary and starts defusing with the oxidiser present from the initial conditions. The concept of ignition does not exist in the SLF combustion model. Combustion is purely a function of mixture fraction. As fuel and oxidiser diffused in the fuel inlet piping the solver started simulating combustion in these first steps in this confined space. This caused some problems for the solver and temperature had to be limited to maximum values for many cells. This was overcome as the initial front of the fuel from the boundary moved inwards towards the combustor. If possible a local zone with different initial conditions could be useful here.

Table 4: *This table shows the initial conditions for simulation case 1.*

Parameter	Value	Unit	Comment
Mixture Fraction Profile	0.0	dimensionless	Pure oxidiser in the fluid volume
Mixture Fraction Variance	0.0	dimensionless	No mixture fraction variance
Nitrogen Oxide	0.0	-	No NO_x as initial condition
Pressure	101325.0	Pa	Atmospheric pressure
Static Temperature	294.15	K	Ambient temperature
Turbulence Intensity	0.0	-	No turbulence as initial condition
Turbulence Length Scale	0.0	m	No turbulence as initial condition
Velocity	0.0, 0.0, 0.0	m/s	No velocity initially

3.7.4 Boundary Conditions

The boundary conditions for case 1 are given in tables 5, 6 and 7. They are presented here, because the boundary conditions are essential for outcome for the simulation.

3.7.4.1 Fuel Inlet Boundary Conditions

The fuel inlet boundary conditions are given in table 5. The length of the fuel inlet is set to eight times the diameter, 50.4 mm. This is to ensure that the flow is fully developed before entering the combustor.

Table 5: *Table showing the boundary conditions for the fuel inlet boundary.*

Parameter	Value	Unit	Comment
Type	-	-	Mass Flow Inlet
Mixture fraction	1.0	dimensionless	Pure fuel
Mass flow rate	0.00212	kg/s	Measured value
Supersonic Static Pressure	7	Bar	Maximum supply pressure of the regulator valve
Total temperature	318.15	K	Measured value
Turbulence Intensity	0.05	dimensionless	STAR-CCM+ recommended value
Turbulent Length Scale	0.315	mm	STAR-CCM+ recommended value

3.7.4.2 Air Inlet Boundary Conditions

The air inlet boundary conditions are given in table 6. The length of the air inlet is set to eight times the diameter, 576 mm. This is to ensure that the flow is fully developed before entering the combustor. The pipe is made straight even though that is not the case in the real-world setup.

Table 6: *This table shows the boundary conditions for the air inlet boundary.*

Parameter	**Value**	**Unit**	**Comment**
Type	-	-	Mass Flow Inlet
Mixture fraction	0.0	dimensionless	Pure air mixture
Mass flow rate	0.1949	kg/s	Measured value
Supersonic Static Pressure	2.21	Bar	Maximum supply pressure of the regulator valve
Total temperature	387.05	K	Measured value
Turbulence Intensity	0.05	dimensionless	STAR-CCM+ recommended value
Turbulent Length Scale	3.6	mm	STAR-CCM+ recommended value

3.7.4.3. Outlet Boundary Conditions

The exhaust outlet boundary conditions are presented in table 7. The outlet pipe length is set to eight times the diameter of the outlet, 520 mm, to make sure there is no backflow at the outlet during simulation. In the real-world setup, the distance between the outlet and the turbine is only the thickness of the flanges connecting the parts.

The only user input for the outlet boundary is that it is defines as an outlet and that 100 % of the flow goes through it, split ratio 1.0. A basic outlet was chosen for the simulation because no other parameters were known for this boundary.

Table 7: *Table showing the boundary conditions for the exhaust outlet boundary.*

Parameter	**Value**	**Unit**	**Comment**
Type	-	-	Outlet
Mass Flux Specification	-	-	Specified Split Ratios
Split Ratio	1.0	-	There is only one outlet

3.7.4.4 Wall Treatment Boundary Conditions

All internal walls of the simulation domain are smooth non-slip walls. The walls are treated as adiabatic and there is no heat flux across the walls. A solid domain for the material of the walls has not been created, so there is no conjugate heat transfer. All wall values are left at default values.

3.8 Mesh Sensitivity

A mesh sensitivity check was performed by running the simulation several times with an increasing number of computational nodes. The simulation ran four times to 10,000 iterations. Due to long solver time, a fifth and sixth run was made with fewer iterations. The fifth run ran for approximately 6,000 iterations and did achieve convergence. The sixth run was stopped prior to convergence and only serves to map the limits of the computer system.

The only change made to the model was the cell base size for the mesh. This alters the total number of computational nodes in the domain, hereunder the total number of cells, faces and vertices. Each change in base size resulted in between 40-70 % increase in the total number of cells in the domain.

Table 8: *Base size and total cell count in the computational domain for case 1.*

Base size:	3.5 mm	3.0 mm	2.5 mm	2.0 mm	1.75 mm	1.5 mm
Cell count:	5,155,962	7,972,990	12,627,867	20,739,190	29,017,681	48,944,439
% increase in cell count:	-	~55 %	~58 %	~64 %	~40 %	~69 %

There was a close to linear development in solver iteration time per CPU-core with regards to the number of cells in the computational domain. The sixth run with very high cell count resulted in a clear increase in solver iteration time, exposing the limits of several components in the system. It also resulted in sluggish system response, so the solver was stopped prior to reaching convergence. There is a clear advantage to keeping the cell count as low as possible with regards to computing resources available, especially if optimization requires the simulation to be run many times. The engineering scalars for the NO_x models required the most iterations before converging for all grid resolutions. The iteration time per CPU core is presented in figure 13.

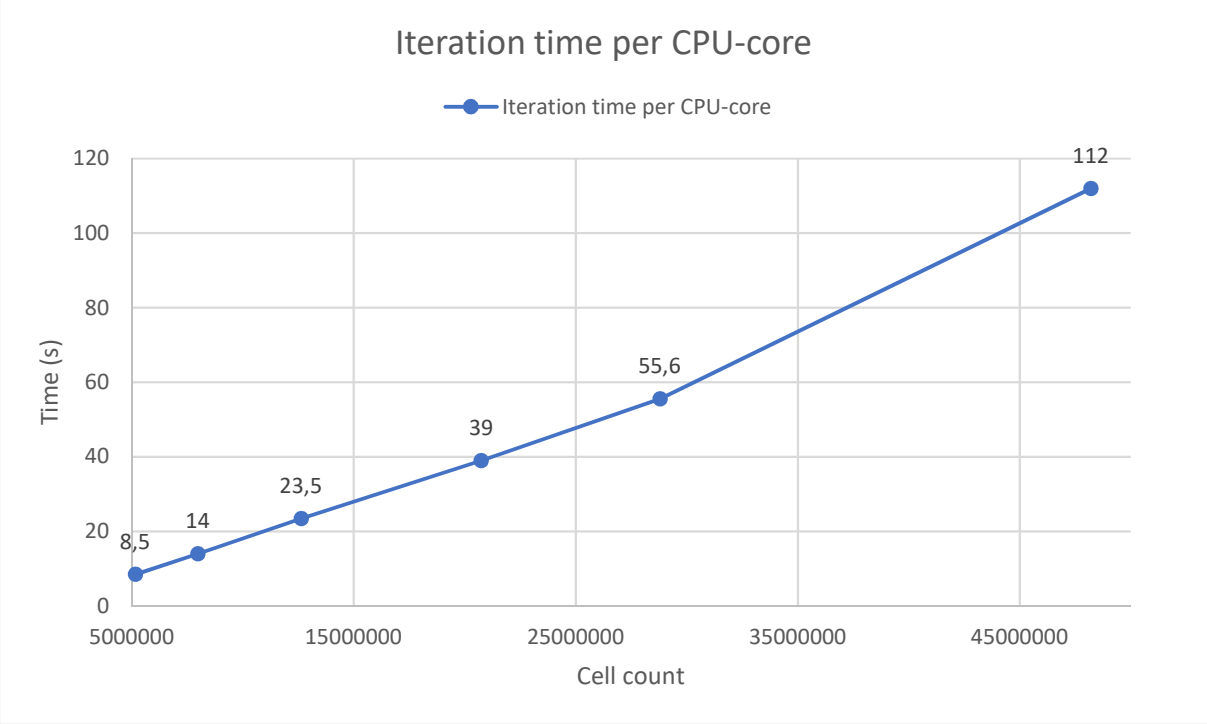

Figure 13: *The figure shows the time for one computational iteration to complete with regards to the total number of cells in the computational domain. The number of seconds provided are approximations as the solver time fluctuates somewhat for each iteration. The iteration time shows linear development until the cell count reaches the system limit.*

Several of the engineering scalars of interest were examined with regards to the total number of cells. An average of the five simulation runs was calculated and the deviation from this average was plotted for the various scalars. The scalars examined were pressure and temperature for the P3 and T3 measurement points. For the combustor outlet the minimum, average and maximum temperature were examined. Additionally, the scalars for the minor chemical species of unburnt propane, CO and NO_x were also examined.

The P3 pressure measurement points showed almost no change with an increase in cell count and are insensitive to resolution. The plot is provided in the appendix. The minimum temperature at T3 measurement points exhibited a quite substantial change with cell count. The data from the simulation comes from 15 single point measurements. This could be an explanation for the quite large changes as they can be affected by a change in the single computational node. The combustor outlet temperatures were more linear with regards to cell count. This is probably because they are averaged over the entire combustor outlet which consists of far more computational nodes. The minor species exhibit the largest sensitivity to increased grid resolution. They required a base size of 2 mm which corresponds to approximately 20.7 million cells before flattening out.

Based on this the 20.7 million cell count simulation seems to be the best compromise between computing resources and good mesh-independent results. However, if the minor species are not of interest, more global parameters can be examined with a less resolved grid.

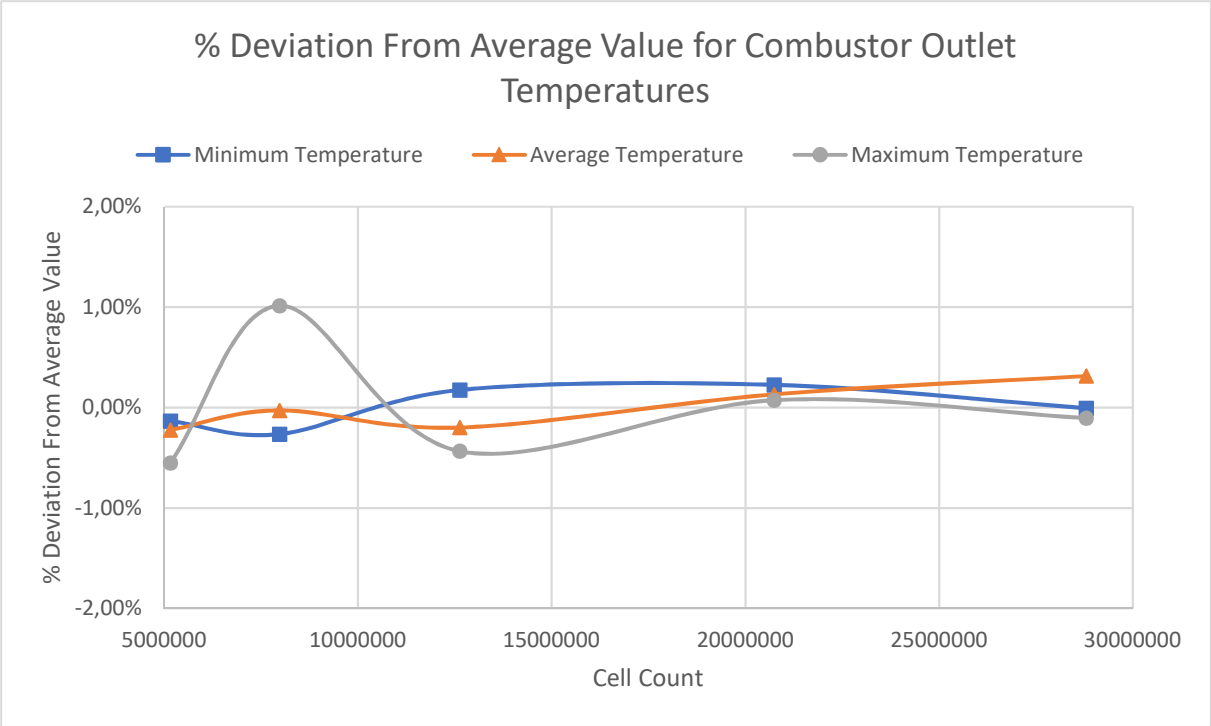

Figure 14: *The figure shows a graph for the percentage of change in engineering scalars for combustor outlet temperature, when compared to the average value of the five simulation runs performed in the mesh sensitivity check. The graph uses smoothed lines to show the trend. There is not much deviation in the results with regards to cell count.*

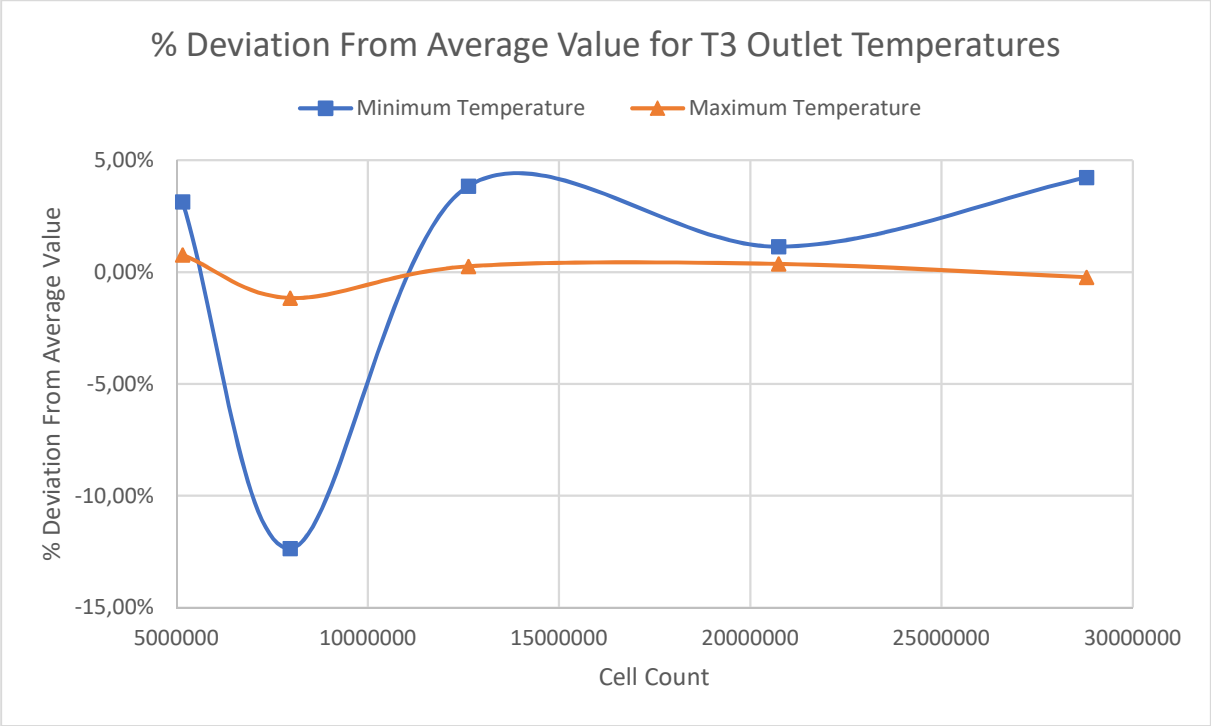

Figure 15: *The figure shows a graph for the percentage of change in engineering scalars for T3 temperature measurement points, when compared to the average value of the five simulation runs performed in the mesh sensitivity check. The graph uses smoothed lines to show the trend. There is a quite large deviation in the T3 minimum temperature. These values are gathered from 15 single points in the grid and the values are more prone to fluctuations compared to the combustor outlet temperature measurements.*

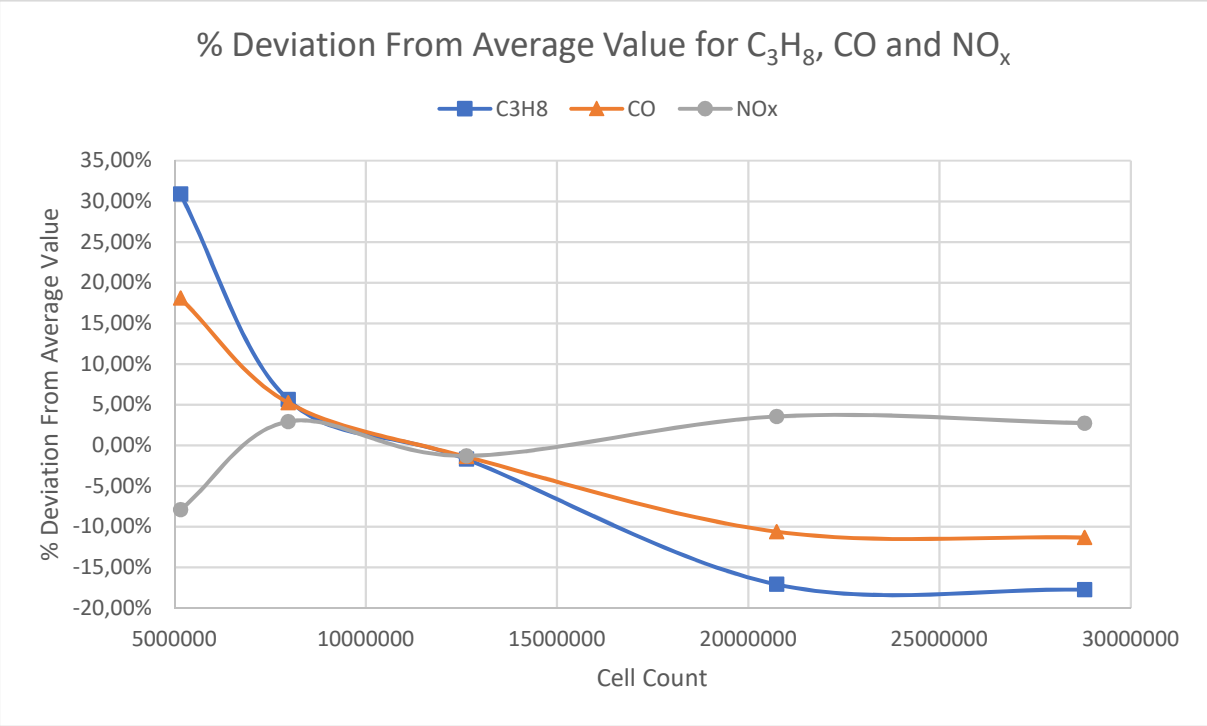

Figure 16: *The figure shows a graph for the percentage of change in engineering scalars for C_3H_8, CO and NO_x when compared to the average value of the five simulation runs performed in the mesh sensitivity check. The graph uses smoothed lines to show the trend. There are quite large variations in the results between the meshes. These scalars need a finer mesh than the outlet temperatures before flattening out.*

3.9 Convergence

The goal of any numerical simulation is to have the iterative process converge to a solution. For a steady-state simulation, this equates to a specific value for each of the engineering scalars to be examined. Convergence was determined by examining the residuals plot and the engineering scalars. All examined values converged. To ensure steady-state values, each simulation ran for 10,000 iterations before the engineering scalars were sampled.

A check was also performed with the double precision version of the software, because the added precision sometimes can affect the results. There was no change compared to the single precision version, only an increase in computing time for each iteration of approximately 25 %.

The residuals plot in figure 17 shows the residuals for the various terms in the conservation equations. The residuals plot shows convergence for all terms. Momentum, dissipation rate, kinetic energy and energy all show strong convergence with residuals below 1e-07. Continuity also exhibits quite strong convergence with residual at about 1e-06. Mixture fraction and mixture fracture variance shows weak convergence, though acceptable for this simulation. The residuals for NO_x also converged, however with a high value. The residual was high for all resolutions.

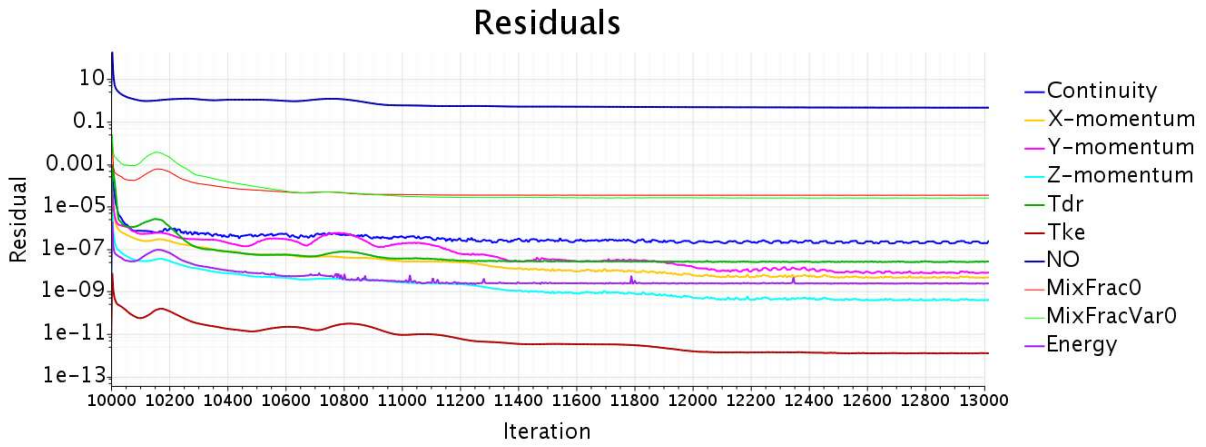

Figure 17: *The residuals plot from STAR-CCM+, showing convergence for all terms for case 1.*

It is worth noting that the simulation with 20.7 and 29.0 million cells had to be initiated from a converged solution of lower cell count. STAR-CCM+ will extrapolate data from the nodes of the lower resolution solution into the nodes of the higher resolution model. This will overcome problems with steep gradients between initial- and boundary conditions. This suggests that some details in the mesh setup ideally should be changed as the cell count is increased significantly. However, the higher resolution models converged without problems when initiated from a lower resolution model.

3.10 Mesh

The model is meshed by the Surface Remesher, Prism Layer Mesher and the Polyhedral Mesher. The base size for the mesh was 2 mm with 3 prism layers. However, several areas in the model required additional refinement with regards to both base size, the number of prism layers and the total thickness of the boundary layer. The geometric features that required refinement were the fuel injection nozzle, the spray area from the nozzle and into the flame tube, the top of the flame tube and the bottom of the flame tube. Each region had its own requirement to obtain a quality mesh and targeting the correct wall y^+ values. Default settings and values are used except when otherwise noted.

Settings for the global mesh:

- Base Size: 2.0 mm
- Target Surface Size: 100 % of base
- Minimum Surface Size: 10.0 % of base
- Surface Growth Rate: 1.3
- Number of Prism Layers: 3
- Prism Layer Near Wall Thickness: 1.0 mm
- Prism Layer Total Thickness: 70.0 % of base

3.10.1 Nozzle Refinement

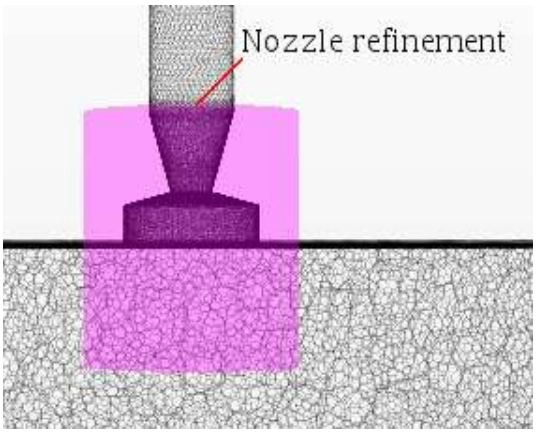

Figure 18: *The nozzle required a refinement that created a very fine volumetric mesh with a well resolved boundary layer to capture the velocity of the fuel through the nozzle and the orifice. The coloured area shows the refinement zone.*

The nozzle required a refinement that created a very fine volumetric mesh with a well-resolved boundary layer to capture the velocity of the fuel through the nozzle and the orifice. The volumetric dimensions are also very small compared to the overall dimensions of the combustor, which requires a fine mesh to capture the details. This is the origin for the injection-spray of the fuel.

Settings for Nozzle Refinement:

- Custom Size: 2.5 % of base
- Number of Prism Layers: 13
- Prism Layer Near Wall Thickness: 0.01 mm
- Prism Layer Total Thickness: 100 % of base

3.10.2 Injector Spray Refinement

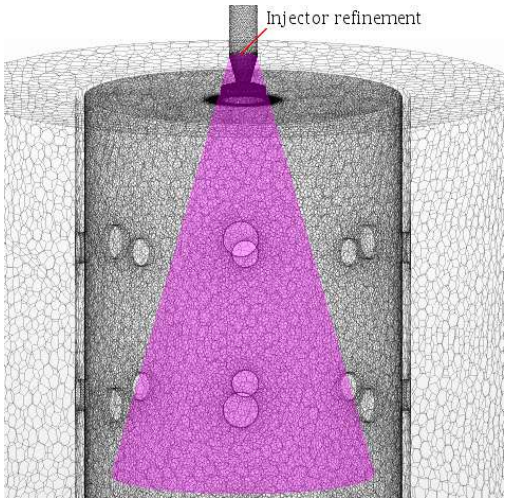

Figure 19: *The injector spray required a very fine volumetric mesh to resolve the spray of fuel into the combustor. The coloured area shows the refinement zone.*

The injector spray required a very fine volumetric mesh to resolve the spray of fuel into the combustor. The selected custom size is double that of the nozzle refinement. This created a good blending and limits the cell count somewhat. The spray volume is much larger than the nozzle volume. The prism layer count is still high but only affects a small area near the wall on the top of the combustor.

Settings for Spray Refinement:

- Custom Size: 5.0 % of base
- Number of Prism Layers: 11
- Prism Layer Near Wall Thickness: 0.05 mm
- Prism Layer Total Thickness: 100 % of base

3.10.3 Flame Tube Refinement

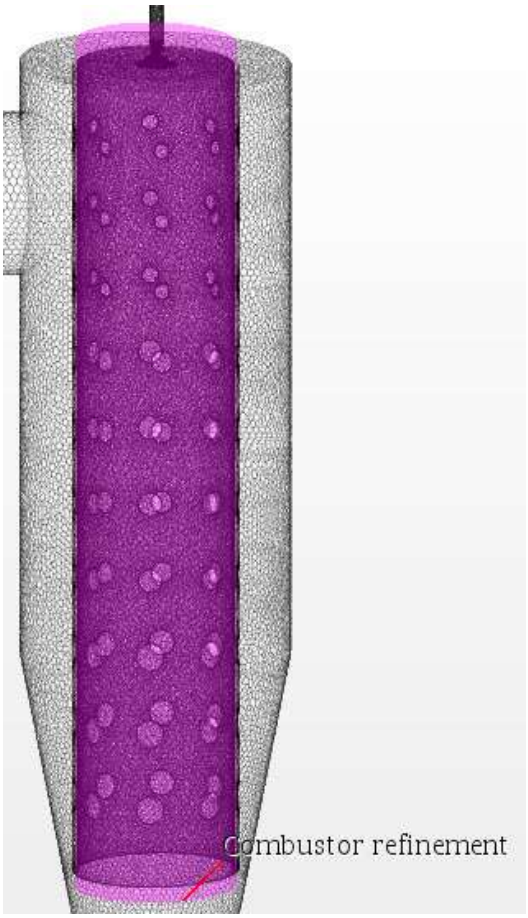

Figure 20: *The combustor flame tube required a well-resolved boundary layer to resolve the boundary layer of the air entering through the holes in the flame tube, the combustion and the acceleration of the fluid due to the heat release from the reacting flow. The coloured area shows the refinement zone.*

Figure 21: *The bottom of the flame tube required additional refinement of the boundary layer mesh so that it could resolve the higher fluid velocities closer to the combustor outlet. The coloured area shows the refinement zone.*

Settings for Combustor Refinement:

- Custom Size: 25.0 % of base
- Number of Prism Layers: 11
- Prism Layer Near Wall Thickness: 0.05 mm
- Prism Layer Total Thickness: 100 % of base

Settings for Bottom Refinement:

- Custom Size: 25.0 % of base
- Number of Prism Layers: 13
- Prism Layer Near Wall Thickness: 0.01 mm
- Prism Layer Total Thickness: 100 % of base

3.11 Mesh Quality

Several parameters are required for a good quality mesh. With complicated geometries such as for this case, these parameters must be balanced against each other as one setting can affect several parameters. It is very difficult to achieve perfect cell quality; though it is important to keep the number of good quality cell very high compared to those of less quality. Cell Quality Remediation was activated to compensate somewhat for a few bad cells. The function of this model is to suppress the effect of the bad quality cells on the overall solution.

3.11.1 Volume Change

When examining volume change the volume of each cell is compared to the cells neighbouring it. The cells should not be widely different in volume as this will lead to problems for the solver, inaccurate result and divergence. A volume change of 0.01 and below as considered to be bad cells. The model only has a very few number of bad cells. The model statistics are presented in table 9.

Table 9: *This table shows the model statistics for volume change between neighbouring cells for case 1.*

Volume Change between	Number of Cells	Percentage of Total Cells
1.0 – 0.1	20559179	~99.132 %
0.1 – 0.01	179981	~0.868 %
0.01 – 0.001	30	~0.000 %
0.001 and below	0	0.000 %

3.11.2 Face Validity

Face validity refers to the three parameters listed below:

1) Free edges are cell faces that are not connected to a neighbouring face.
2) Non-manifold edge is a cell face that is connected to two or more edges.
3) Pierced faces refer to a cell face that has one or more edges piercing it.

If face validity is to low, the volumetric mesher will not be able to produce the volumetric mesh [39]. The face validity of the model is good.

Table 10: *This table contains the model statistics for face validity of cell faces for case 1.*

Face Validity between	Number of Cells	Percentage of Total Cells
1.00	20739159	~100.000 %
0.95 – 1.00	28	~0.000 %
0.90 – 0.95	3	~0.000 %
0.90 and below	0	0.000 %

3.11.3 Skewness Angle

The skewness angle refers to how the normal of the cell faces are angled with regards to its neighbours. High skewness angles of above approximately 85° should be avoided if possible. There is a very low count of high skewness angle faces in the model. The faces with high skewness angle are mostly located close to sharp edges such as the bottom of the flame tube. Such areas proved difficult to mesh without some cells having a high skewness angle. The total number of high skewness angle cells are still very low compared to the total number of cells. Increasing mesh resolution improved this parameter compared to the lower cell count models.

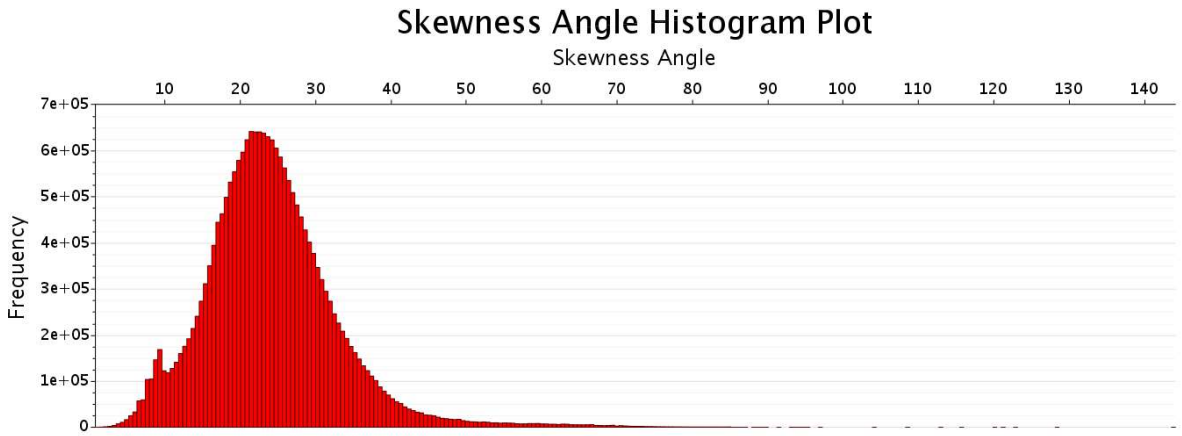

Figure 22: *This histogram plot shows the skewness angle of the cell faces plotted against frequency. There is a very low number of cell faces with high skewness angle.*

3.11.4 Wall y^+ Boundary Layer Resolution

The wall y^+ values of the model were checked to examine if the right wall treatment model had been selected for the K-Epsilon eddy viscosity model. Several iterations with various boundary layer resolutions had to be tried before a good wall y^+ distribution was found. This is an iterative process because the simulation needs to be run for the wall y^+ values to be calculated. Then one needs to go back and remesh, check mesh quality and rerun the simulation if improvements are needed.

Low wall y^+ values signify a high number of prism layers which translates to a high-resolution boundary layer. This adds significantly to the computational cost of the model. A high number of prism layers was prioritized at the nozzle and the inside walls of the flame tube. These are the places were the most accuracy is needed, and the expected velocities are the greatest. As explained previously, for the Two-Layer All y+Wall Treatment model to give accurate results the wall y^+ value should ideally be below 5 or above 30. The wall y^+ distribution is given in figure 23.

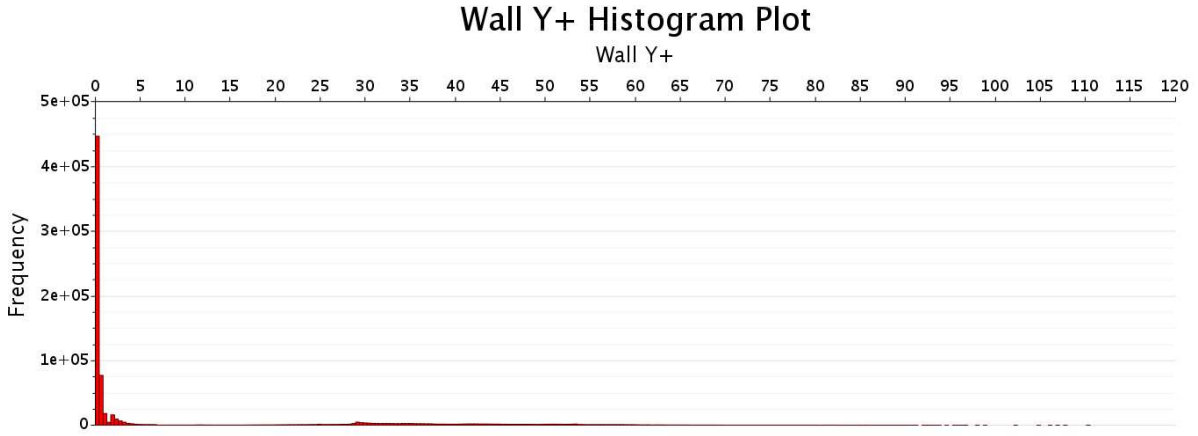

Figure 23: *Wall y^+ values from the simulation. The target was to create a boundary layer mesh that targets low (less than 5) and high (more than 30) wall y^+ values corresponding to the recommendations for the Two-Layer All y+ Wall Treatment model. The values between 5 and 30 should ideally be avoided for accurate results due to the transitional nature of this region were the velocity with regards to wall distance goes from logarithmic to linear development. In the wall y^+ region between 5 and 30 velocities will not be calculated accurately. Low wall y^+ has computational cost because of the additional boundary layer cells needed.*

3.8 Case 2: CFD Setup

Case 2 features the same model setup as for case 1. It is a steady-state simulation using the RANS method with the K-Epsilon model for eddy viscosity and the Steady Laminar Flamelet non-premixed combustion model. The purpose with case 2 is to make design changes to the original design and observe the relative changes between the models for the engineering scalars in question. The model uses the same boundary conditions to avoid introducing too many changes and making relative comparisons relevant. The meshing of the model is performed using the same principles, but some changes are introduced because of the more complex geometry. The design changes made to the model can be summed up as follows:

1) Increased the diameter of the combustor. This is introduced to prevent contact between fuel and wall, to avoid local quenching and hot streaks.
2) Addition of a swirler device. This is introduced to increase turbulence for faster mixing of fuel and air. This should provide improved combustion.
3) Orifice with holes that direct air back into the primary combustion zone.
4) Larger holes for air dilution placed in three distinct zones.
5) The air supply is split into two pipes mounted on separate sides of the combustor. The total cross-section is equal to the single inlet pipe in case 1. This is introduced to see if this will reduce the asymmetry observed in case 1.
6) The air inlet pipes have been moved down towards the dilution zone of the combustor. This should provide more effective dilution of the hot gasses.

The setup for case 2 will not be provided in the same level of detail as case 1, because much of the setup is similar. The following overview is provided for reference:

- Active Models, reference section 3.7.2.
- NO_x Emissions Model, reference section 3.7.2.1.
- Simplifications, reference section 3.7.2.2.
- Initial Conditions, reference section 3.7.3.
- Boundary Conditions, reference section 3.7.4.
    - Fuel Inlet Boundary Conditions, reference section 3.7.4.1.
    - Outlet Boundary Conditions, reference section 3.7.4.3.
    - Wall Treatment Boundary Conditions, reference section 3.7.4.4.

3.8.1 Geometry

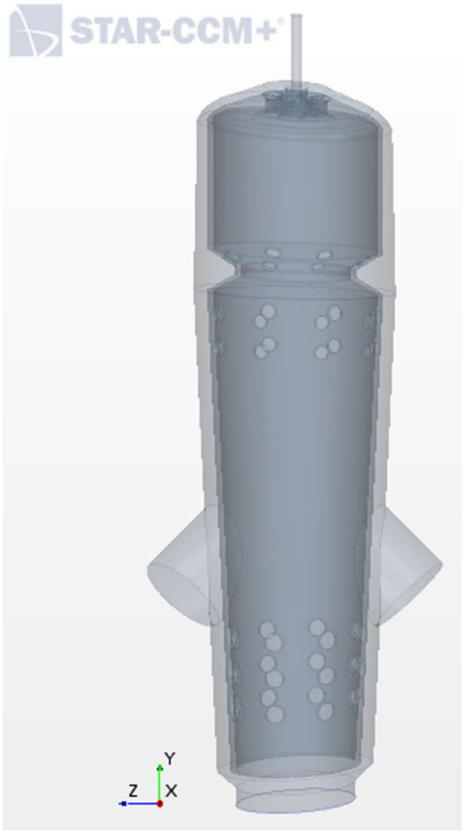

Figure 24: *Transparent isometric view of combustor model for case 2.*

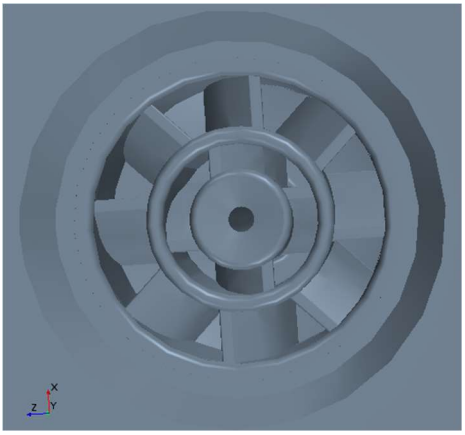

Figure 25: *Swirler designed for case 2.*

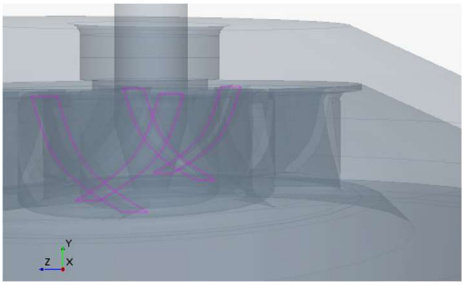

Figure 26: *Side view of the swirler guide vanes. The figure shows the profile shape.*

Figure 24 provides a transparent isometric view of the fluid volume of the geometry designed for case 2. The fuel inlet boundary is still on the top of the combustor and the dimensions of the piping and inlet nozzle are unchanged. There are two air inlet boundaries, one on each side of the combustor. These have an 45° angle of attack. The inner diameter of the air inlet piping is 25.5 mm. This equates to a total inlet cross-section similar to case 1. The outlet diameter is the same as in case 1, 65 mm.

The inner diameter of the top section of the flame tube is 90 mm. At the orifice the diameter is reduced to 60 mm. The orifice starts at y = -78 mm and has an angle of attack of 59° compared to the Y-axis. The orifice ends at y = -102 mm. From this point the flame tube has the shape of a convergent nozzle starting with a diameter of 90 mm and converging to a diameter of 65 mm. The total length of the flame tube is 370 mm. This is the same length as in case 1. The walls of the flame tube are 3 mm thick, though only the fluid volume has been modelled and not the solid.

The casing has an inner diameter of 110 mm. This leaves a 7 mm gap for the airflow between the flame tube and the casing. This gap is constant for the entire bottom part of the combustor. At the end of the flame tube at 370 mm, the casing converges to the outlet diameter of 65 mm over a length of 10 mm in the negative Y-direction. The combustor outlet plane is defined here.

Moving upwards, the gap between the outer walls of the flame tube and the inner walls of the casing is 7 mm. When the gap reaches the orifice, it narrows to 5 mm towards the top of the combustor and this 5 mm channel is extended to the air intake of the swirler.

The swirler, figure 25, has the fuel injection nozzle at its centre. It is surrounded by two circles with guide vanes. The innermost has four vanes leading in one direction. The second has eight vanes leading in the other direction. The profile of the guide vanes can be seen in figure 26. The angle changes from top to bottom. It is close to 45° on average. The overall height of the swirler is 10 mm. From the centre of the fuel injection nozzle there is a 6 mm radius to the inner diameter of the first set of vanes. The thickness of the air gap for this set of vanes is 3 mm. The radius of the outer set of vanes is 11 mm. Here the air gap is 6 mm. It is worth noting that swirler modelling could be a whole thesis by itself. This design should be considered somewhat rudimentary

Compared to the combustor in case 1, this combustor is divided into three distinct zones. The primary zone is at the top. Here the air enters through the swirler. Air is also supplied though eight holes spaced evenly around on the orifice. The holes have a diameter of 8 mm. The air to secondary zone is provided by two rows of 8 mm diameter holes, 16 in total. These start just below the end of the orifice and are separated by 18 mm from centre to centre. At the bottom of the flame tube there are three rows of 10 mm in diameter holes for dilution air, 24 in total. They are spaced 20 mm apart (centre to centre) and the bottom hole is placed 38 mm from the bottom of the flame tube (edge to centre).

3.8.2 Boundary Conditions

No changes are made to the fuel inlet and the air inlet boundary conditions. The air inlet has been split into two pipes supplying the air. These total cross-section of these two pipes is equal to the cross-section of the single air supply pipe in case 1. This change has been added to see how this will affect the visible asymmetry observed in case 1. No changes were made for outlet boundary conditions.

3.8.2.1 Air Inlet Boundary Conditions

There is only on change to the air inlet boundary conditions compared to case 1. The turbulent length scale is set to 2.55 mm. This is 5 % of the inlet diameter as recommended by STAR-CCM+. For other values reference section 3.7.4.2.

3.8.3 Mesh Sensitivity

Case 2 was run with four different resolutions. The base size and cell count is shown in table 11.

Table 11: *Base size and total cell count in the computational domain for case 2.*

Base size:	3.5 mm	3.0 mm	2.5 mm	2.0 mm
Cell count:	6,787,046	10,546,611	14,813,174	26,629,474
% increase in cell count:	-	~55 %	~40 %	~80 %

A mesh sensitivity was performed for case 2 and the same scalars were checked as for case 1. The same procedure was performed, and the data processed in the same manner, reference section 3.8. For case 2 each simulation ran for 8000 iterations. Some of the scalar values were not steady-state. An average of the last 1,000 iterations was used to sample values for mesh sensitivity. The results for mesh sensitivity for case 2 is presented as a short summary.

- The pressure measurement for P3 showed almost no sensitivity to mesh resolution.
- The minimum and maximum temperature measurements for T3 both followed a similarly shaped curve and trend. The scalars had a flattening tendency, but ideally an even higher resolution mesh should be examined.
- The combustor outlet minimum and average temperatures showed little sensitivity to cell count and are insensitive to mesh resolution. The maximum temperature should ideally have been checked with a higher cell count.

- Mass Fraction C_3H_8 at the combustor outlet had a flattening trend from 2.5 mm base size to 2.0 mm base size.
- Mass Fraction CO at the combustor outlet was insensitive to increased cell resolution above 14.8 million cells and showed very little change.
- Mass Fraction NO_x at the combustor outlet should ideally have been check with an even higher resolution mesh. Mesh sensitivity was inconclusive for this scalar.

Ideally an even high resolutions mesh should have been checked. However, this was not possible within the time constraints and the computational power available. Based on the experience from case 1, insensitivity to mesh resolution was found from 2.0 mm base size. The conclusion from the mesh sensitivity check for case 2 was to use the 2.0 mm base size model with 26.6 million cells. For the scalars for NO_x and maximum outlet temperature mesh independence cannot be guaranteed because higher resolutions could not be checked.

3.8.4 Convergence

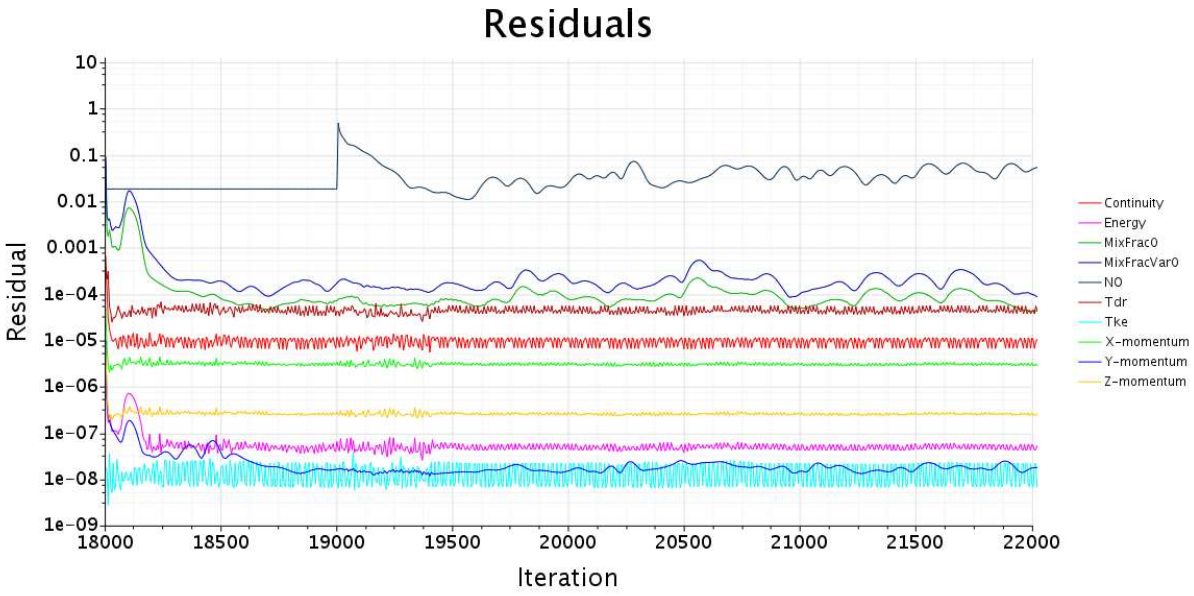

Figure 27: *The residuals plot from STAR-CCM+, showing residuals for case 1. Mixture fraction and mixture fraction variance showed some unevenness, likely caused by the introduction of the swirler device.*

The residuals dropped to strong convergence below 1×10^{-6} for turbulent kinetic energy and Y-momentum. X-momentum dropped to below 1×10^{-5}. Turbulent dissipation rate showed weak convergence at 1×10^{-4}. Mixture fraction and mixture fraction variance showed some oscillation at a little over 1×10^{-4}. NO_x residuals were high as for case 1 and did not completely stabilize. To me the residuals plot suggests that there is some room for improvement in mesh quality. Further improvement was not possible within the timeframe with the available computer resources.

Not all engineering scalars reached complete steady-state. This can be linked to what is reflected in the residuals plot. However, it might also suggest that the design has unsteady combustion, perhaps because of too much turbulence generated by the swirler, orifice and air directed at the primary combustion zone. This will be a topic for closer examination in the results chapter. For the engineering scalars average value were used based on the last 1,000 iterations when needed.

The solver iteration per CPU core, figure 28, showed close to linear development. The system limits were not reached when running the highest resolution model. The system utilizes 23 cores for the solver. This results in a total simulation time of approximately 105 hours for 8000 iterations with the highest resolution model.

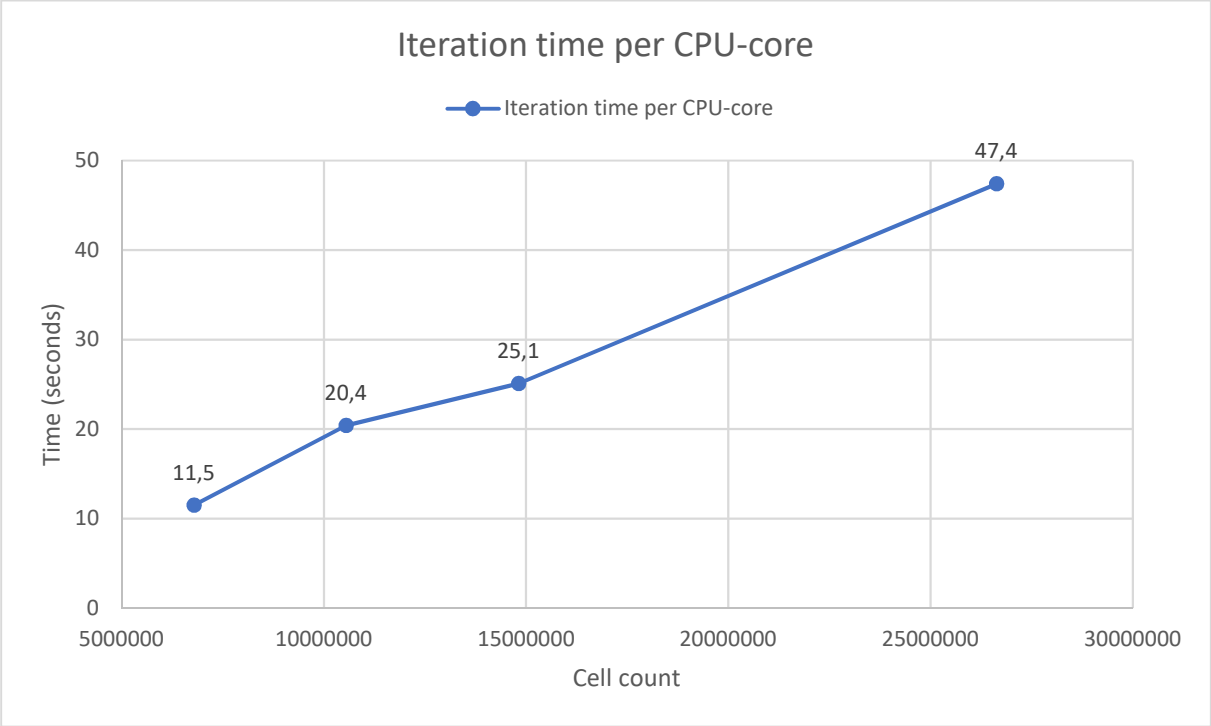

Figure 28: *Figure of solver iteration time. The solver iteration time per CPU core showed close to linear development. System maximum was not reached. This would have been indicted by the change in the linear development.*

3.8.5 Mesh

The same global mesh setting were adopted for case 2 as in case 1. These global settings can be reference in section 3.10. The same layout for the zones of refinement were also used. The refinement zone for the top part of the flame tube was changed to follow the shape of the walls of the orifice. Because the diameter of the new design is larger, computational constrains forced a change in the target cell size for the refinement zones. The target size was increased by a factor of 1.5. All other setting remained the same as for case 1 and can be referenced in sections 3.10.1-3. The new target size for the refinement zones are as follows:

- Nozzle Refinement, relative to base: 3.75 % (up from 2.5 %).
- Spray Refinement, relative to base: 7.5 % (up from 5.0 %).
- Combustor Refinement, relative to base: 37.5 % (up from 25.0 %).
- Bottom Refinement, relative to base: 37.5 % (up from 25.0 %).

3.8.6 Mesh Quality

Mesh quality is assessed on the same basis as for case 1. Volume change, face validity, skewness angle and wall y^+ has been examined. The Cell Quality Remediation was also activated for case 2 supress the

effect of a small number of bad cells. Based on the results presented below the overall quality of the mesh for case 2 is slightly lower than for case 1. This is due to the more complicated geometry of case 2 that requires additional detail to mesh operation.

3.8.6.1 Volume Change

Volume Change is given in table 12. All cells should ideally be over 0.01. The model contains 42 cells that can be considered as bad cells.

Table 12: *This table shows the model statistics for volume change between neighbouring cells for case 2.*

Volume Change between	Number of Cells	Percentage of Total Cells
1.0 – 0.1	26274510	~98.667 %
0.1 – 0.01	354993	~1.333 %
0.01 – 0.001	41	~0.000 %
0.001 – 0.0001	1	~0.000 %
0.0001 and below	0	0.000 %

3.8.6.2 Face Validity

Face validity was good. The mesher did not encounter any errors during meshing. There is a small number of cells with face validity below 1 when compared to the first case.

Table 13: *This table contains the model statistics for face validity of cell faces for case 2.*

Face Validity between	Number of Cells	Percentage of Total Cells
1.00	26629474	~100.000 %
0.95 – 1.00	58	~0.000 %
0.90 – 0.95	13	~0.000 %
0.90 and below	0	0.000 %

3.8.6.3 Skewness Angle

The skewness angle histogram plot is presented in figure 29. The plot is quite similar to the plot for case 1. The majority of cell are in the good region. There is a small number of high skewness angle cells. This should ideally be avoided.

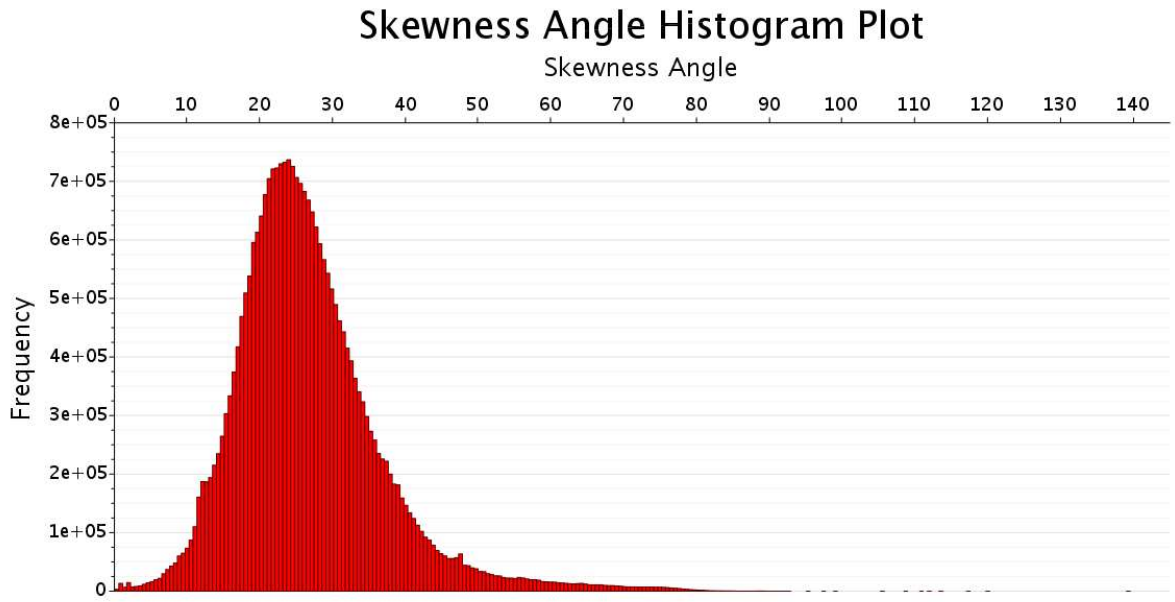

Figure 29: *This histogram plot shows the skewness angle of the cell faces plotted against frequency. There is a very low number of cell faces with high skewness angle.*

3.8.6.4 Wall y^+ Boundary Layer Resolution

The wall y^+ values of the numerical model for case 2 are presented in figure 30. The range of values for wall y^+ is shifted slightly towards higher values when compared to case 1. This is a consequence of the larger cell target size which causes the boundary layer to be less resolved. Most of the cells still have a value of lower than 5 and above 30. Shifting the results towards lower values will require a more resolved boundary layer. This comes at the cost of higher cell count and computational cost.

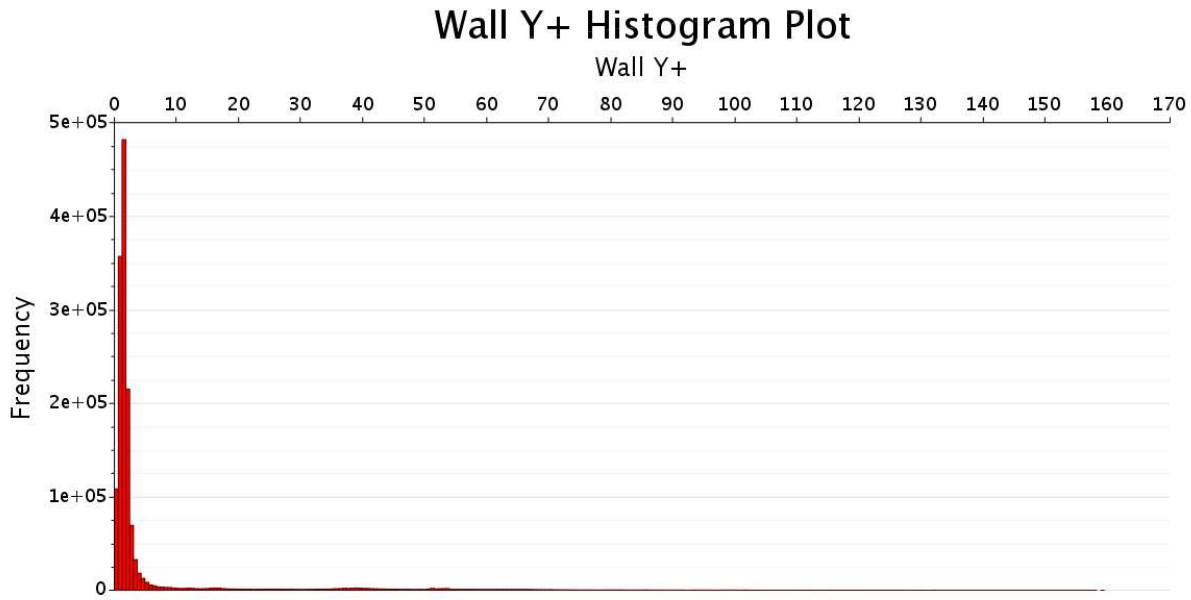

Figure 30: *The figure shows the wall y^+ values from simulation case 2. Because of the increase in target cell size there is a slight shift towards higher wall y^+ values for case 2 compared to case 1. There is still only a small number of cells with wall y^+ that are positioned in the interim region ranging from 5 to 30. Ideally the boundary layer could have some additional resolution. This would come at the cost of increased cell count.*

4.0 Results and Discussions

This chapter contains the results from the numerical simulations, presented as case 1 and 2. Both cases are steady state simulations using RANS method with K-Epsilon viscosity and the Steady Laminar Flamelet model for simulating combustion. Case 1 is a simulation of the existing combustor. Case 2 is a new design suggestion.

4.1 Results of Case 1

The simulation is a steady-state simulation were all the engineering scalars in question have converged to single values. It is possible to gather a lot of data from the numerical model in STAR-CCM+. The results presented in this chapter are a selection of the data that is available from the model. Only the most important data has been selected for presentation. This gives a good overall view of the design.

4.1.1 Sampling Points

In the numerical model, sampling points are needed for collecting data. In this work these sampling points are single probe points, probe lines with several probe points a plane section cutting through the geometry.

Figure 31 shows the location of the probe lines used for sampling data. The lines are placed in 100 mm steps along the length of the combustor, in the negative Y-direction. Y = 0 mm is at the top of the combustor. The probe lines are placed on a 2D plane section in the Y- and Z-axis through the centre of the combustor. Each probe line consists of 144 sampling points. In addition, there are plane sections at the same negative Y values as the probe lines.

Figure 32 shows the placement of the sampling points used to simulate the placement of measurement points for pressure and temperature on the real combustor. The exact location of P3 and T3 cannot be accurately placed in the model because on the real combustor the depth and angle will vary each time the instruments are mounted. To accommodate for this weakness in the design, a rectangular grid with many points has been set up in the model. These points are separated by 10 mm in all directions from a centre point on the centreline of the combustor. Data is sampled from these points simultaneously and presented as the pressure and temperature measurement. Minimum and maximum values are collected.

There is an outlet plane section for data collection at the combustor outlet. The plane surface is used for several measurements. This is also shown in figure 32.

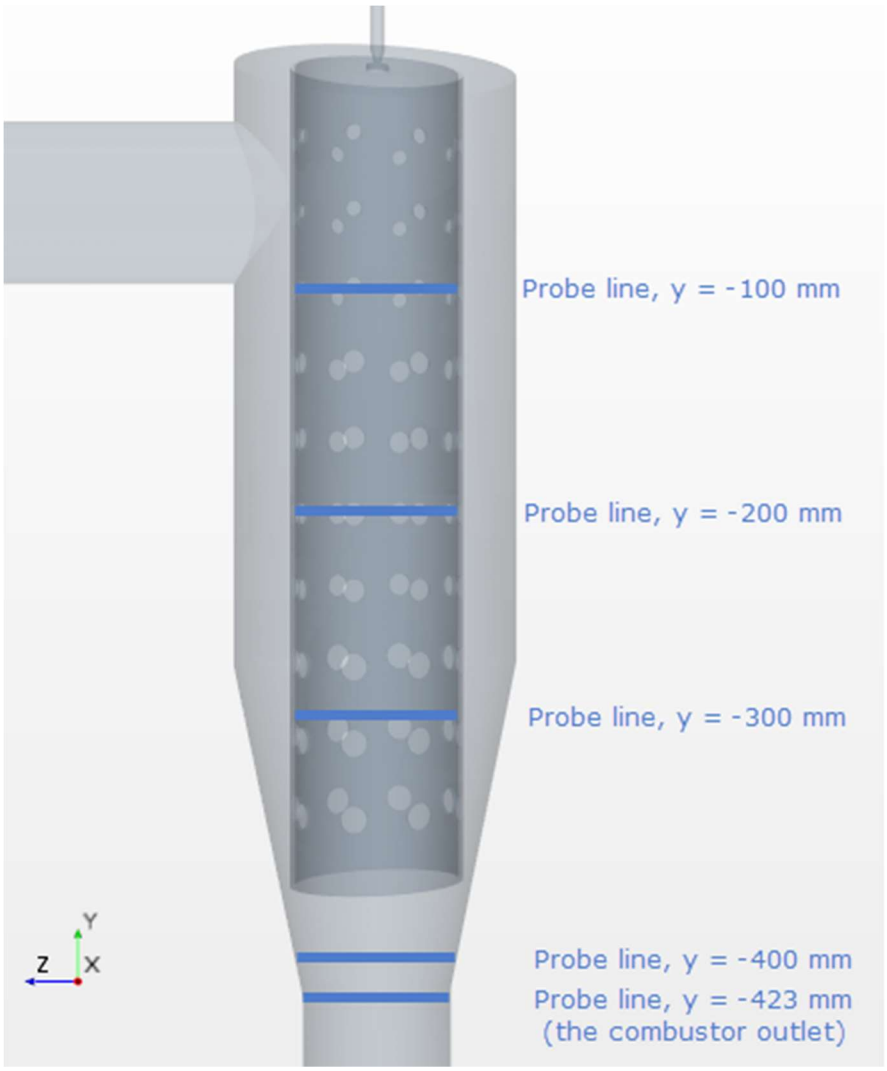

Figure 31: *The figure shows the location of the probe lines used for sampling data. The lines are placed in 100 mm steps along the length of the combustor, in the negative Y-direction. Y = 0 mm is at the top of the combustor. The probe lines are placed on a 2D plane section in the Y- and Z-axis through the centre of the combustor. In addition, there are plane sections at the same negative Y-values as the probe lines.*

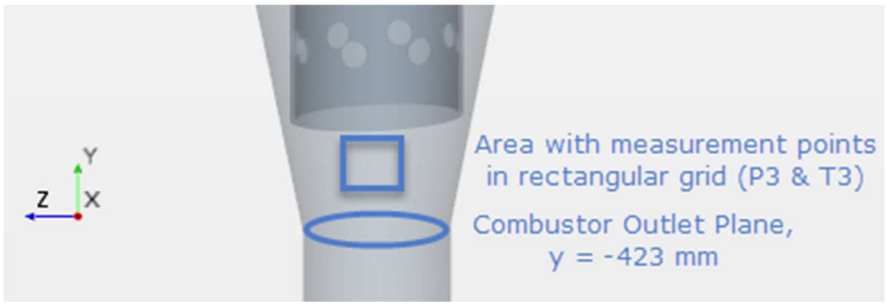

Figure 32: *This figure shows the placement of the sampling points used to simulate the placement of measurement points for pressure and temperature on the real combustor. The exact location of P3 and T3 cannot be accurately placed in the model because on the real combustor the depth and angle will vary each time the instruments are mounted. To accommodate for this weakness in the design, a rectangular grid with many points has been set up in the model. These points are separated by 10 mm in all directions from a centre point on the centreline of the combustor.*

4.1.2 Converged Values for the Engineering Scalars

For the selected engineering scalars, the simulation converged to the values given in table 14.

Table 14: *The table provides the converged values for selected engineering scalars from simulation case 1.*

Parameter	**Location**	**Value**	**Unit**
Minimum absolute pressure	Measurement points	200,650	Pa
Maximum absolute pressure	Measurement points	201,089	Pa
Minimum absolute pressure	Combustor outlet plane	200,144	Pa
Average absolute pressure	Combustor outlet plane	200,751	Pa
Maximum absolute pressure	Combustor outlet plane	202,213	Pa
Minimum temperature	Measurement points	1273.7	K
Maximum temperature	Measurement points	2001.5	K
Minimum temperature	Combustor outlet plane	388.7	K
Average temperature	Combustor outlet plane	878.5	K
Maximum temperature	Combustor outlet plane	1970	K
Minimum velocity	Combustor outlet plane	100.3034	m/s
Average velocity	Combustor outlet plane	137.9567	m/s
Maximum velocity	Combustor outlet plane	214.1044	m/s
Combustor outlet mass flow rate	Combustor outlet plane	-0.1964917	kg/s
Mass fraction O_2	Combustor outlet plane	0.1929905	Dimensionless
Mass fraction C_3H_8	Combustor outlet plane	3.698223×10^{-6}	Dimensionless
		~3.70	ppmw
		$\sim 7.267 \times 10^{-4}$	g/s
Mass fraction CO	Combustor outlet plane	1.457218×10^{-3}	Dimensionless
		~1457.22	ppmw
		~0.286	g/s
Mass fraction NO_x	Combustor outlet plane	3.866202×10^{-6}	Dimensionless
		~3.90	ppmw
		$\sim 7{,}597 \times 10^{-4}$	g/s

It can be observed from table 14 that the values for minimum and maximum pressures are quite closely grouped. When using the air inlet pressure and the combustor outlet pressure as a basis this translates to a pressure loss of between 18,787 Pa and 20,856 Pa. This translates to a pressure loss in the combustor of between 8.50% and 9.44%. As indicated in section 2.6 the pressure loss of a good combustor design should be in the region between 2% and 4%. This design has too high pressure loss to be characterised as good. The simulation is also an ideal case. In the real-world combustor, there are additional sources for potential pressure loss at flanges, threaded connections, gaskets and insertion holes for instrumentation. The pressure loss in the real-world combustor is surely higher than the simulation shows.

It can also be observed that maximum temperatures and that CO emissions are very high. This will be examined in closer detail in separate sections.

4.1.3 Experimental Data

Previous test run performed by Bergquist et al. [12], Larsson et al. [13] in addition to a demonstration resulted in the measurements presented in table 15.

Table 15: *Table provides the converged values for selected engineering scalars from simulation case 1.*

Test run number	Temperature T3 (K)	Pressure P3 (bar a)	Performed by
1	1105.15	No measurement	Bergquist et al. [12]
2	1312.07	1.051	Larsson et al. [13]
3	1359.05	1.052	Larsson et al. [13]
4	1444.39	1.413	Larsson et al. [13]
5	1716.15	No measurement	Demonstration in 2017

4.1.4 Model Validation

Based on the results from the numerical model an attempt to validate the model is performed. This is important to strengthen the credibility of the model. Unfortunately, the current instrumentation of the HVL GTE is somewhat limited. Adding additional instrumentation and performing extra test runs is beyond the scope of this thesis.

The current instrumentation on the combustor consists of a single thermocouple probe for measurement of temperature and a pressure sensor for measurement of stagnation pressure. Both located close to the combustor outlet. The exact location of the measurements cannot be specified, but an approximate position can be taken from pictures of the setup. The pressure sensor was installed by the last group to do work on the gas turbine engine [13], so no stagnation pressure measurements are done by the previous groups [10-12]. The temperature sensor is a thermocouple device that is inserted into the combustor. The insertion depth is not specified, nor is it precisely repeatable because there is very little guidance for the sensing device and the insertion depth can also vary. The jet flame exiting the flame tube has a narrow diameter and temperatures can vary greatly depending of position. This is confirmed by the fact that the various groups have a wide range of temperature values from the different test runs performed. The span between the lowest and the highest measurements taken is 611 K. There is also no confirmation of accurate calibration of the sensing devices in these previous works [10-13] and the last group speculate on the limited accuracy of several measurements [13].

The groups also reported high pressure loss in the combustor due to leakages around the top flange, at the measurements device insertion holes and through the ignition sparkplug hole in the top of the combustion chamber. Due to a defective ignition system, the combustor has to be ignited by a hand-held burner and the spark plug hole could not be properly sealed after ignition of the combustor [13].

All in all, the limited quality of the previous measurements makes it difficult to properly validate the numerical model. This is recognized as a weakness in this work. The stagnation pressure measurements taken by [13] are of very little value, due to high losses in the real-world combustor that cannot be properly modelled. The maximum measured pressure at P3 for one of the test runs is 141,300 Pa. This results in a 59,350 Pa deviation from the lowest value for P3 in the numerical model. This gives a deviation of 29.58 % between the numerical model and the measured results. It is possible that the pressure loss in the real-world combustor is in that range. This measurement is hardly useful for accurate validation.

The measurement points for temperature in the numerical model show that the sampled temperature can vary widely based on grid location. Moving 10 mm from the centreline of the combustor towards the edge gives a temperature difference of as much as 728 K, so the location of the sample point is very important. Since the exact measurement location of previous works [10-13] cannot be properly replicated it is difficult to shown matching values. However, 4 out of 5 measurements taken in the last test runs [13] are within the span given by the measurement grid in the numerical model. This suggests at least some correlation between measurements and model.

4.1.5 Temperature Profile in Vertical Plane Section

The temperature scalar scene, figure 33, shows the fluid temperature on a 2D plane section along the centreline of the combustor. Fuel is injected from the top and air enters from positive Z-direction. The air enters the flame tube through the holes that are visible along the entire flame tube.

Note the asymmetry of the temperature field and the hot streaks along the wall in negative Z-direction. Also, note the asymmetry in the way air enters the flame tube through the holes and the shape of the fuel injection spray. The temperature field shows the development of a jet flame that exits the combustor at the bottom. At the bottom of the flame tube, there is a small gap between the flame tube and the liner wall that creates a thin layer of cool air along the outer wall.

The asymmetry of the temperature field and the bent shape of the fuel injection spray is probably caused by the asymmetry of the design. As can be clearly seen in figure 11 the air inlet piping is located on one side of the combustor and is also offset from the centreline. This probably causes differences in the mass flow of air that enters the flame tube through the various holes. This will cause an asymmetry in the local air/fuel ratio that can explain the temperature field. Areas with high air/fuel ratio will burn leaner and have more dilution. The areas with lower air/fuel ratio will burn richer and this will cause higher combustion temperatures. This explanation is also supported by the mixture fraction vertical plane section, figure 44.

The temperatures and hot streaks along the wall in negative Z direction are too high. This will cause problems with the longevity of the metal because it is not protected by a coating or air film cooling. The hot zones are a source of NO_x emissions.

The temperature profile plane section also shows that the combustor produces a jet flame with a hot core that is almost unaffected by the dilution air. Only centimetres below the combustor outlet are the blades of the turbine. These are rotating at very high speed and should not be exposed to this high-temperature jet flame. Reliability will certainly be affected and break-down of the turbine is expected. This setup will not be able to run for a long time without being damaged by the temperatures.

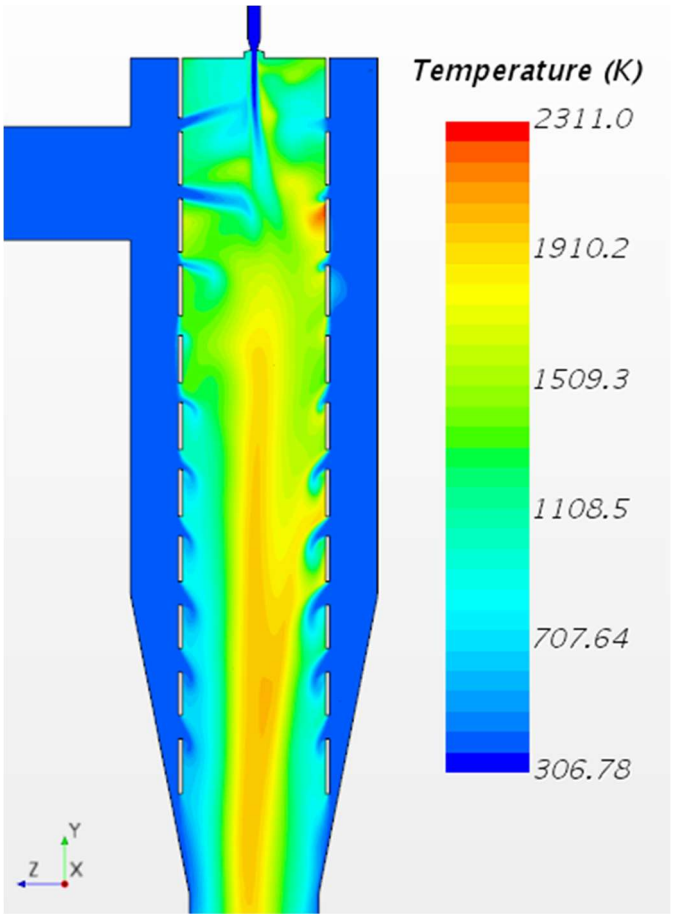

Figure 33: *Scalar scene showing the temperature on a 2D plane section along the centreline of the combustor. Note the asymmetry of the temperature field and the hot streaks along the wall in negative Z-direction. Also, note the asymmetry in the way air enters the flame tube through the holes and the shape of the fuel injection spray. The temperature field shows the development of a jet flame that exits the combustor at the bottom. At the bottom of the flame tube, there is a small gap between the flame tube and the liner wall that create a thin layer of cool air along the outer wall.*

4.1.6 Temperature Profile in Horizontal Plane Sections

Figures 34 to 39 show temperature views of plane sections at y = -100, -200, -300 and -400 mm in addition to the combustor outlet at y = -420 mm. The plane sections shed some additional information on the temperature development. Hot streaks along the walls are clearly visible and suggests a non-uniform combustion especially at y = -100 and -200 mm. Also, the development of the jet flame with a high-temperature core that is mostly unaffected by the dilution air can be seen clearly at y = -300 and -400 mm and also at the combustor outlet. This high-temperature core is a source for NO_x emissions. The lower temperature zones such as those indicated at y = -200 and -300 by teal and blue tinted colours might also indicate excessive quenching of temperature. This might cause incomplete combustions suggested by the very high levels of CO emissions.

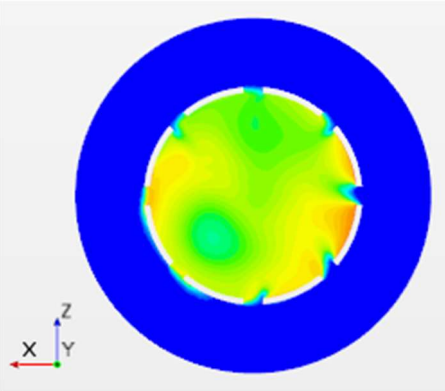

Figure 34: *Temperature at y = -100 mm.*

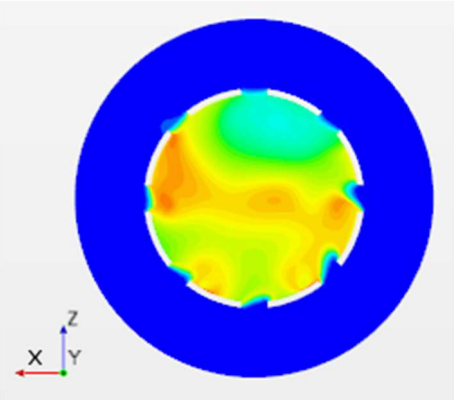

Figure 35: *Temperature at y = -200 mm.*

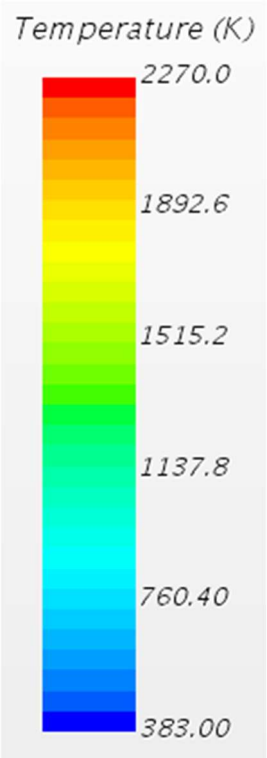

Figure 36: *Temperature scale in Kelvin.*

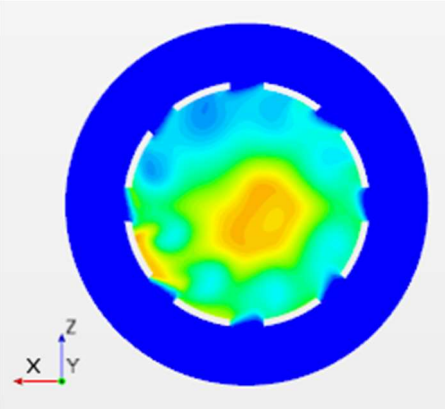

Figure 37: *Temperature at y = -300 mm.*

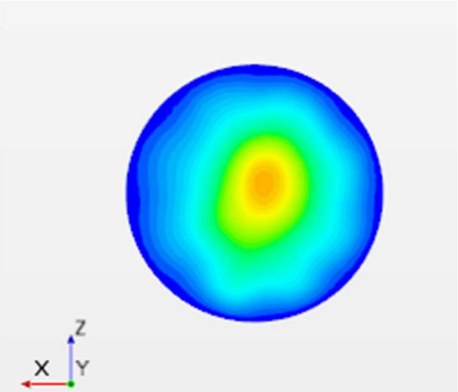

Figure 38: *Temperature at y = -400 mm.*

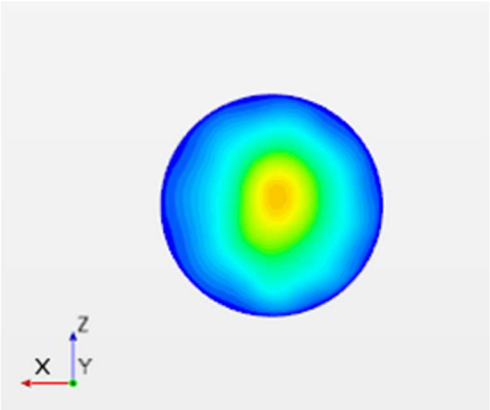

Figure 39: *Temperature at y = -420 mm (combustor outlet)*

4.1.7 Temperature Profile XY Plot

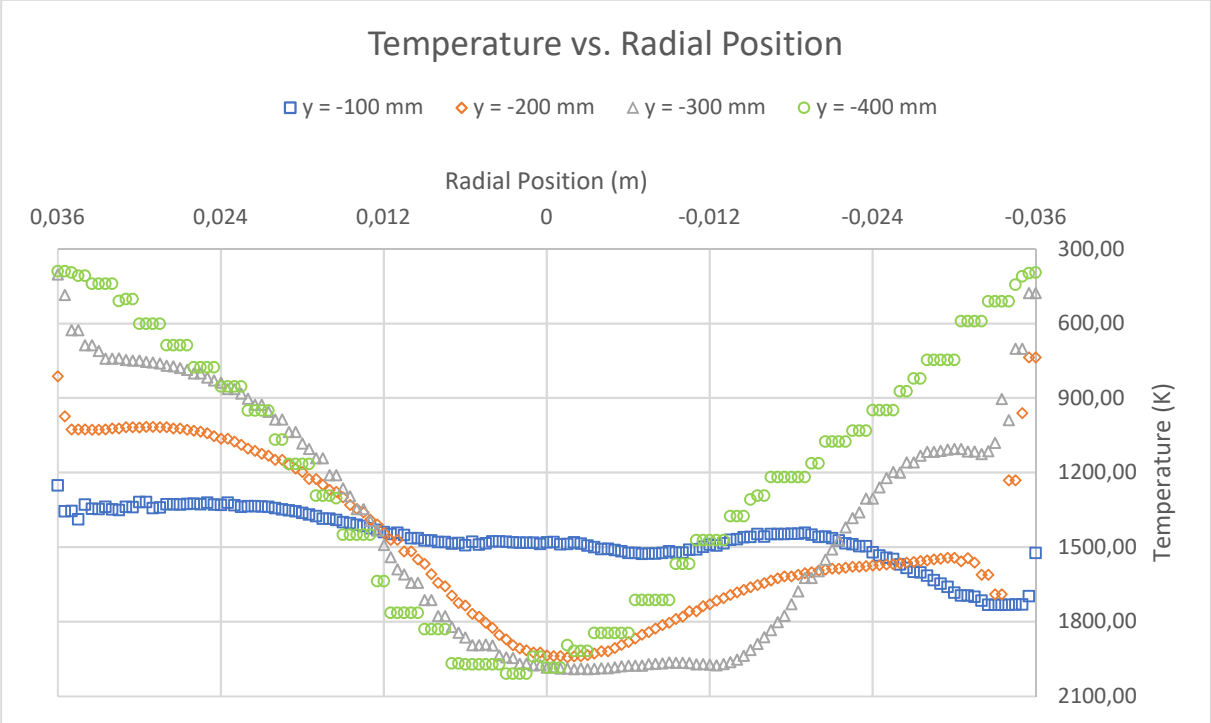

Figure 40: *This figure shows the fluid temperature plotted against the radial distance. The data comes from four plot lines on a 2D plane section. The plot lines are at 100, 200, 300 and 400 mm distance from the fuel injection nozzle at the top of the combustor. The figure shows the development of the temperature profile as the fluid moved down through the combustor. Note the asymmetry clearly visible at 100, 200 and 300 mm. The plot line at 400 mm is close to the combustor outlet and is quite similar to the profile across the combustor outlet.*

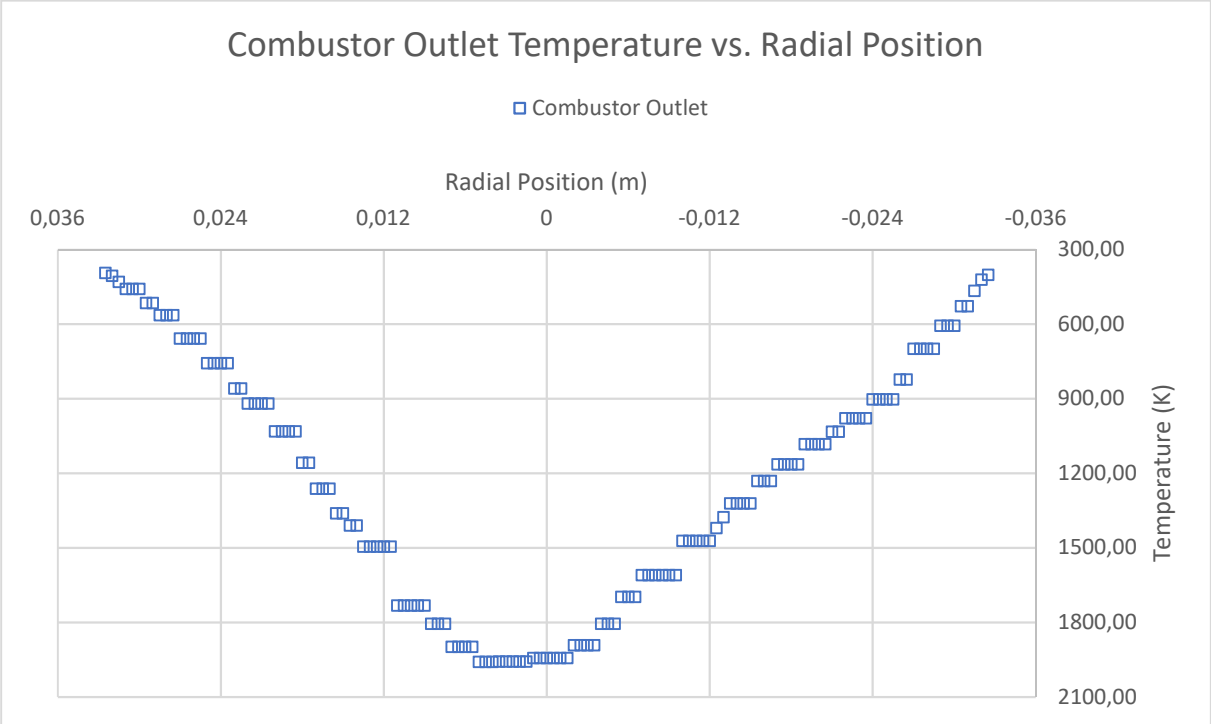

Figure 41: *This figure shows the fluid temperature at the combustor outlet plotted against the radial distance. The data comes from a plot line on a 2D plane section. The plot is close to symmetrical around the centreline of the combustor. The combustor outlet is shown in a separate figure because the data points are very close those at y = -400 mm. For readability and because the combustor outlet temperature is an important specification it is shown separately.*

Figures 40 and 41 show the temperature profile relative to the radial position. This shows the temperatures at the plot lines in more detail than the contoured figures do. The asymmetry in temperature can clearly be seen. It also shows that very high temperatures occur. At y = -100 and -200 mm there are high temperatures along one side and as the flame develops there is a high-temperature core that reaches temperatures of approximately 2000 Kelvin. This will generate NO_x. The temperature drops close to the wall suggests the possibility of flame quenching and incomplete combustion. At the combustor outlet, the temperature profile is almost symmetrical, suggesting that the asymmetry of the construction does not have much influence at this distance from the air inlet. Ideally, the outlet profile should have lower temperatures and be more evenly distributed.

4.1.9 Velocity Profile in Vertical Plane Section

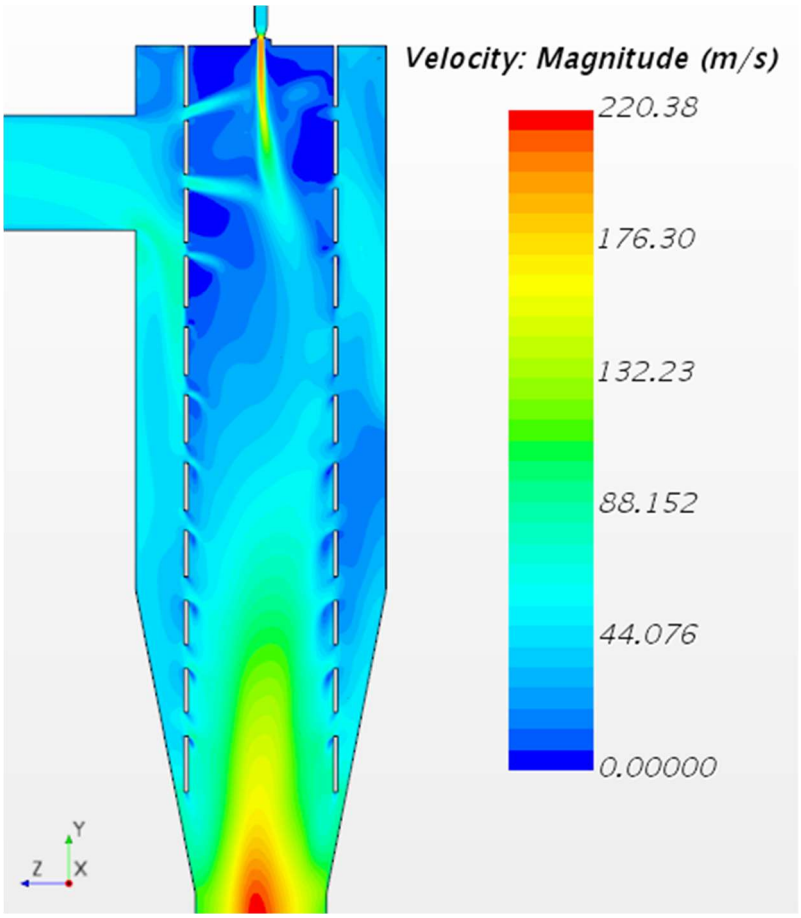

Figure 42: *Scalar scene showing the fluid velocity on a 2D plane section along the centreline of the combustor. Note the very high fuel inlet velocities that likely lift the flame far into the combustor. This is likely contributing to the high CO emissions.*

The velocity scalar scene shows the magnitude of the fluid velocity on a 2D plane section along the centreline of the combustor. Fuel is injected from the top and air enters from positive Z-direction. The air enters the flame tube through the holes that are visible along the entire flame tube. As expected the model shows acceleration of the air as it passes through the holes into combustion zones. The velocity of the air entering through the holes from the positive Z-direction is higher than on the other side.

There is also asymmetry in the velocity field inside the combustion zone as seen by the bent shape of the fuel injection spray. The injected fuel has very high velocity due to the high fuel supply pressure and the nozzle. As noted earlier, the exact shape of the injection nozzle is not modelled, however, the orifice diameter is correct, so the acceleration of the fuel can be assumed. These high speeds will lift the flame from the top of the combustor which can contribute to the very high CO emissions from the combustor. The fuel velocity is too high and the resident time inside the combustor is too low. The combustion process is likely not finished before the fluid leaves the combustor through the outlet.

4.1.10 Velocity Profile XY Plot

Figure 43 shows the acceleration of the fluid as it is expanded by the rise in temperature. The plotline for y = -100 mm has a bump that rises to approximately 50 m/s. This shows that the high-velocity fuel injection has affected one-quarter of way through the combustor. The effect of this is that there is a very short timeframe for the fuel to diffuse and combust in the primary combustion zone.

The plot lines for y = -200 mm and below shows the development of the velocity in closer detail than the contour plane section. At y = -200 mm the casing of the combustor is still straight, so the overall acceleration here should be mostly caused by the expanding hot gasses. At y = -300 and below the casing is formed into a convergent nozzle. The decrease in diameter causes rapid acceleration. High outlet velocity is needed to drive the turbine. The maximum velocity at the outlet is 214.4 m/s which is not surprising. The velocity also seems to be a little less affected by the asymmetry than the temperature, although not completely symmetrical.

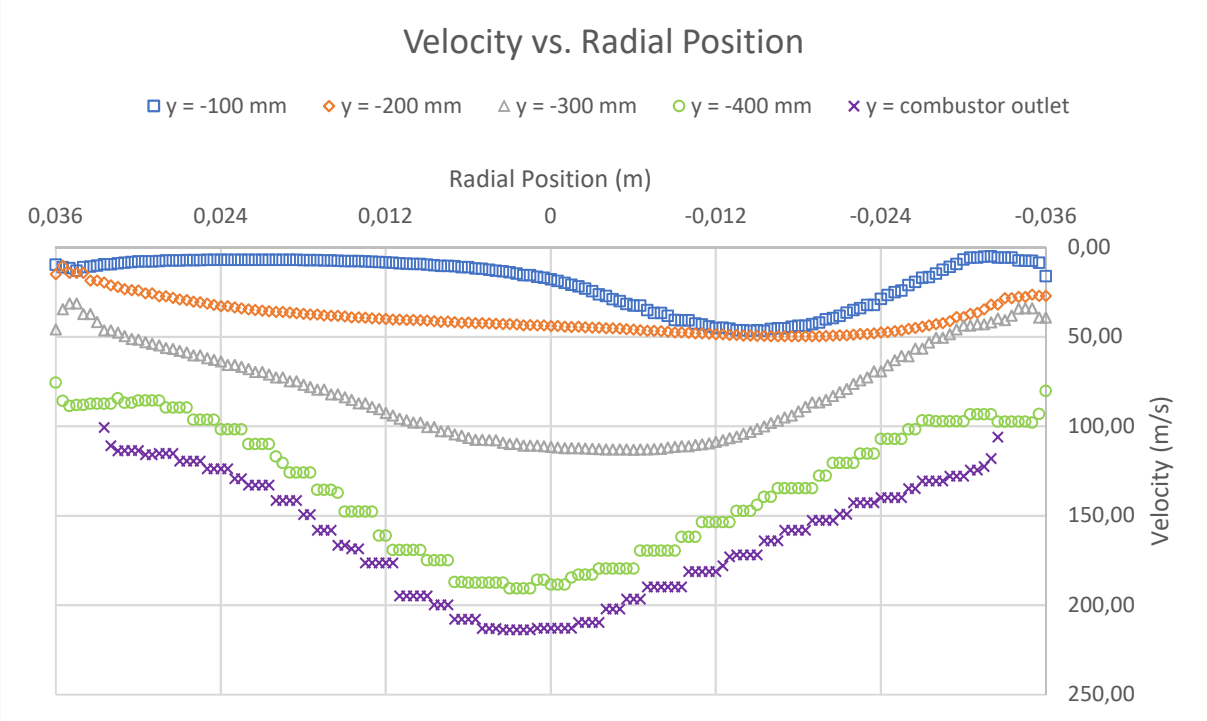

Figure 43: *The figure shows the fluid velocity plotted against the radial distance. The data comes from five plot lines on a 2D plane section. The plot lines are at 100, 200, 300 and 400 mm distance from the fuel injection nozzle at the top of the combustor. The fifth plotline is at the combustor outlet. The figure shows the development of the velocity profile as the fluid moved down through the combustor. Note the asymmetry clearly visible at y = -100 mm. This is likely the effect of the high-speed fuel injection and the asymmetry of the air inlet.*

4.1.11 Mixture Fraction Profile in Vertical Plane Section

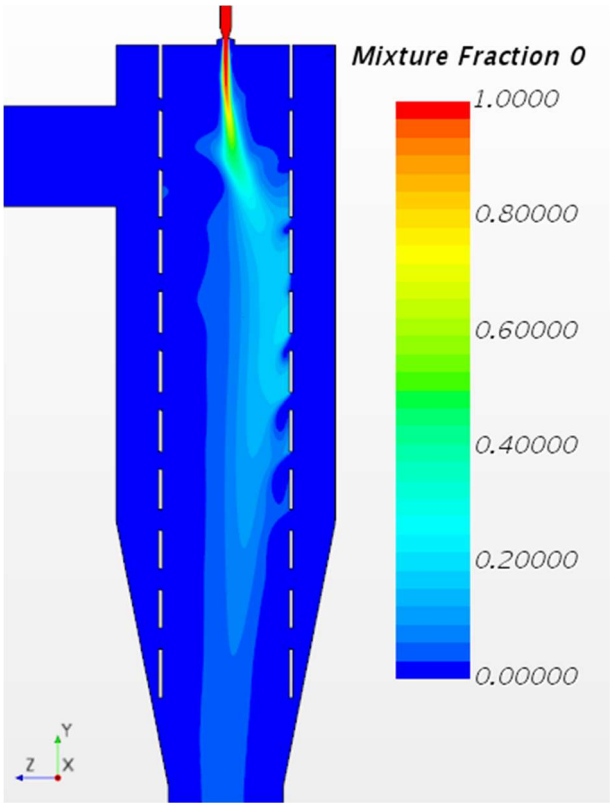

Figure 44: *Scalar scene showing the mixture fraction on a 2D plane section along the centreline of the combustor. This figure clearly shows incomplete combustion of the fuel before the combustor outlet.*

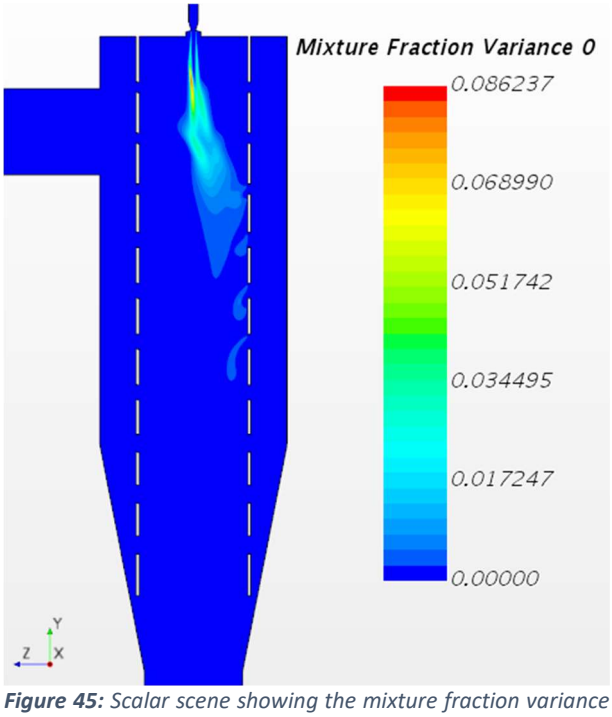

Figure 45: *Scalar scene showing the mixture fraction variance on a 2D plane section along the centreline of the combustor.*

The mixture fraction plane section, figure 44, shows the fraction of fuel and oxidiser. A mixture fraction of 0.0 indicated pure oxidiser as defined in the model. In this case, the oxidiser is an oxygen and nitrogen mixture corresponding to air. A mixture fraction of 1.0 is pure fuel.

The mixture fraction plane section clearly shows that combustion is not complete prior to the fluid exiting the combustor. As expected the mixture fraction variance plane section, figure 45, shows that the area with the highest mixture fraction variance corresponds to the area with high mixture fraction.

From the figures, it seems that the diffusion of the fuel and air is not efficient, as shown by the high mixture fraction concentration at the top of the combustor. The shape of the fuel injection nozzle and spray is essential for obtaining good diffusion between fuel and oxidiser. In this design, the area around the fuel injection does not provide the necessary turbulence to increase the diffusion rate. It is common for combustors to have a swirler device at the fuel inlet that created the needed turbulence to speed up the mixing. This combustor has no such device.

This also illustrates why pre-mixing of fuel and oxidiser has some clear advantages because the mixture will be ready for combustion faster upon entering the combustor.

With this diffusion rate and the velocity of the flow, the resident time for the fuel inside the combustor is clearly too short, resulting in incomplete combustion and unburnt fuel escaping through the outlet. The asymmetry in the diffusion of the fuel caused by the air inlet placement is also very visible in the figures.

4.1.12 Mixture Fraction Profile XY plot

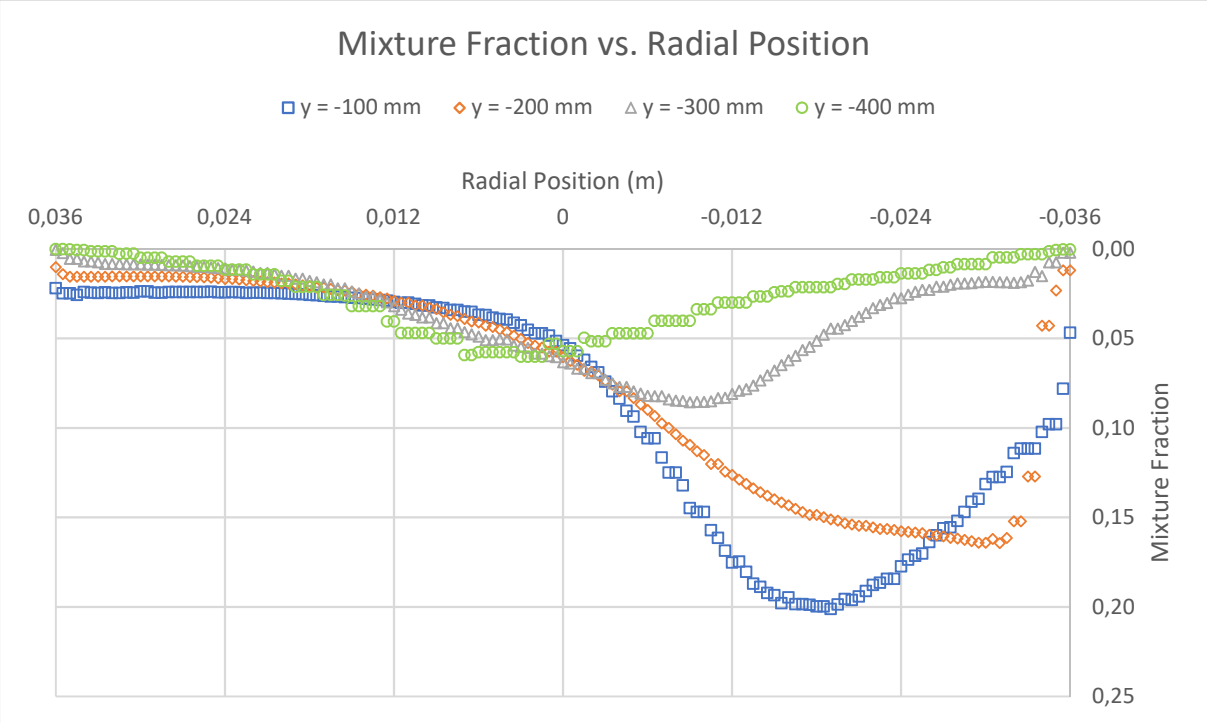

Figure 46: *The figure shows the mixture fraction of the fluid plotted against the radial distance. The data comes from four plot lines on a 2D plane section. The plot lines are at 100, 200, 300 and 400 mm distance from the fuel injection nozzle at the top of the combustor. The figure shows the development of the mixture fraction as the fluid moved down through the combustor. Note the asymmetry clearly visible at y = -100, -200 and -300 mm. The plot line at y = -400 mm is more symmetrical around the centreline of the combustor.*

As calculated previously a mixture fraction of 0.06 indicated close to stoichiometric combustion. The XY plot lines in figure 46 show that combustion is taking place throughout the length of the combustor and that the combustion is not completed even close to the outlet. The XY plot line for y = -400 mm shows that combustion is still happening at this location and that the mixture fraction in the centre of the combustor is close to 0.06. This equates to combustion at close to maximum temperatures which are also shown in the temperature XY plot, figure 40. The plot lines for y = -100 and -200 mm show the asymmetry of the design.

4.1.13 Mass Fraction C_3H_8 Profile in Vertical Plane Section and XY Plot

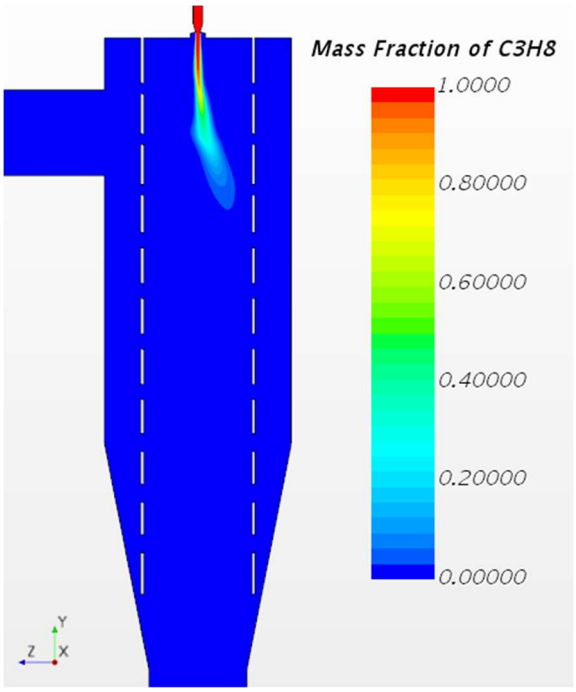

Figure 47: *The figure shows a 2D plane section for mass fraction propane. The resolution of the contours is to coarse to show very low mass fractional values.*

The mass fraction plane section, figure 47, and the mass fraction vs. radial position XY plot, figure 48, are interesting. They show that the mass fraction of fuel is quite rapidly decreasing to close to zero before the fluid reaches y = -300 mm. This is surprising given that the previous plane sections and plots clearly show that the combustion process is still taking place throughout the length of the combustor. This suggests to me that the combustion process has started, but that some intermediate step in the combustion process is dominating. This suggests that it is the resident time for the fluid inside the combustor that is the major contributor to the incomplete combustion rather than the diffusion rate. Ideally, the mass fraction of fuel should be close to zero at y = -200 mm as this is approximately half way through the combustor and past the primary combustion zone. The asymmetry of the design is also visible in the figures.

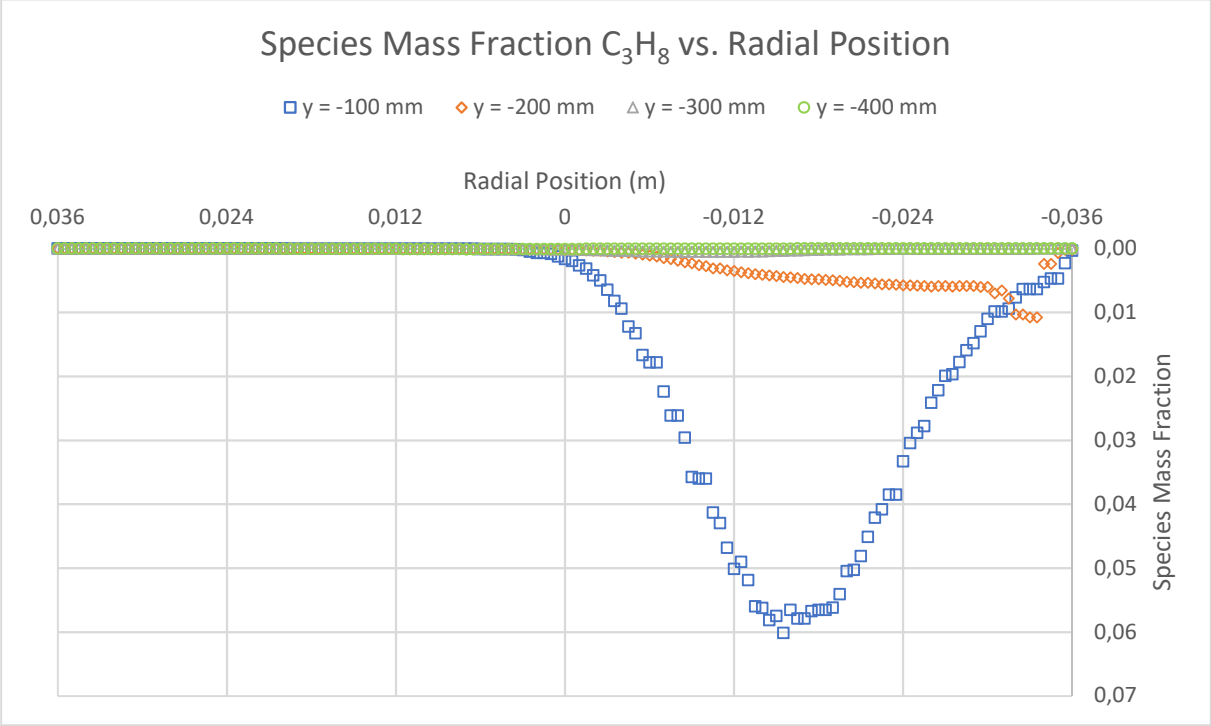

Figure 48: *The figure shows the fuel mass fraction plotted against the radial distance. The data comes from four plot lines on a 2D plane section. The plot lines are at 100, 200, 300 and 400 mm distance from the fuel injection nozzle at the top of the combustor. The figure shows the oxidation of the fuel as the fluid moved down through the combustor. Note the asymmetry clearly visible at y = -100 and -200 mm. The plot lines at y = -300 and -400 mm are close to zero as there is very little fuel left.*

4.1.14 Mass Fraction CO Profile in Vertical Plane Section and XY Plot

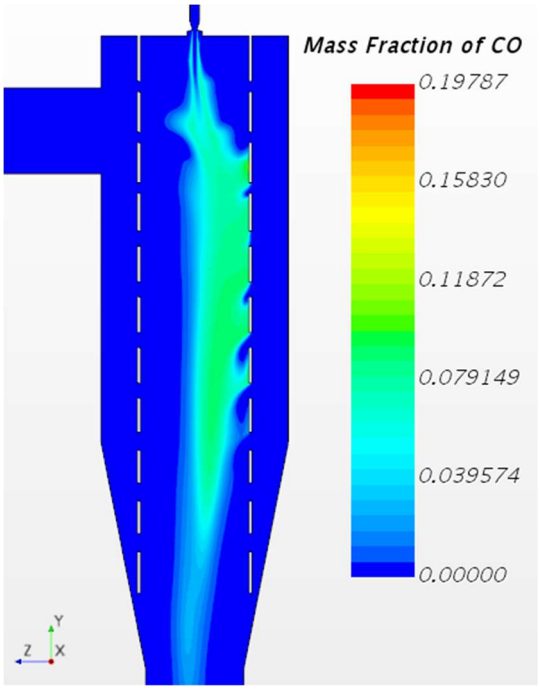

Figure 49: *The figure shows a 2D plane section for mass fraction of CO. CO is an indicator for incomplete combustion.*

As shown by the combustor outlet scaler for mass fraction CO, the combustor has very high CO emissions. This is clearly shown by the 2D plane section, figure 49 and in the mass fraction CO vs. radial position XY plot, figure 50.

CO is an intermediate stage in the combustion process and requires time and heat to completely form into CO_2. The reaction rate is accelerated by higher temperatures. From the XY plot a very fast drop in mass fraction CO can be observed between y = -300 mm and y = -400 mm from about 0.08 to approximately 0.03. This indicates a rapid reaction rate for CO. However, this will not continue through the turbine as temperatures will decrease rapidly once the fluid exits the combustor. Therefore, there is likely also very high emissions of CO from the exhaust outlet of the real-world GTE. Longer resident time for the fluid inside the combustor would reduce the CO by allowing for more complete combustion. The asymmetry of the design is also clearly visible in the figures.

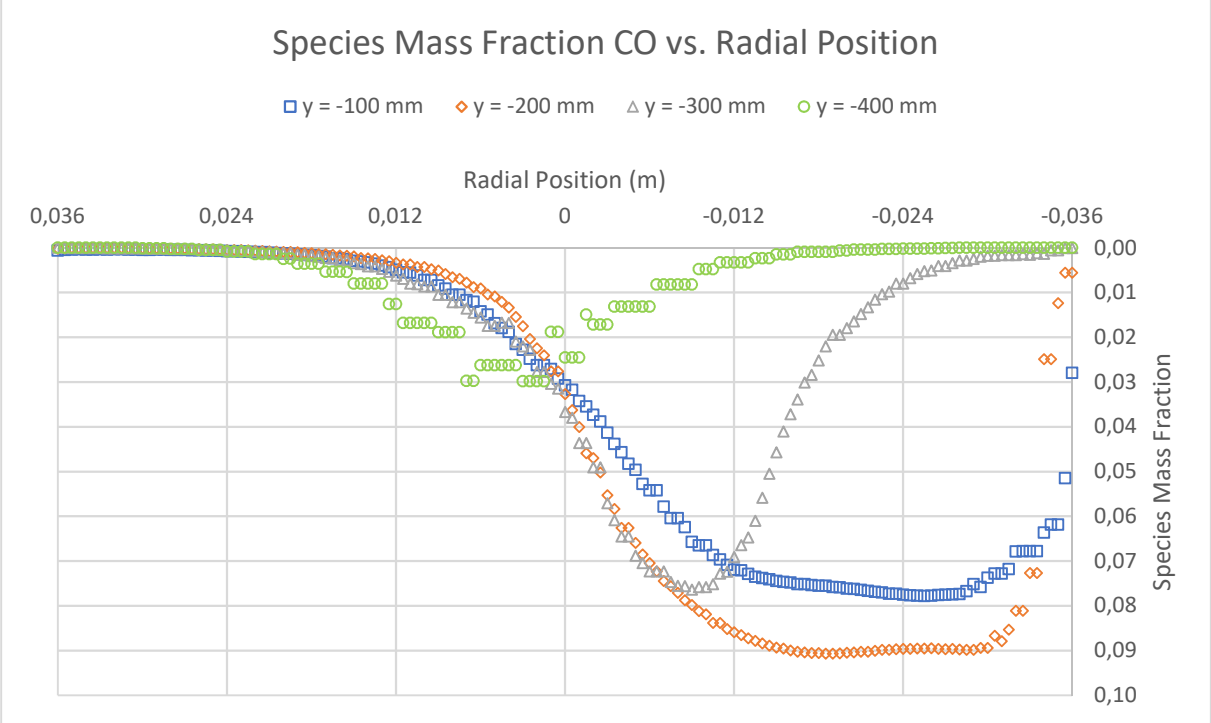

Figure 50: *The figure shows the minor species of CO mass fraction plotted against the radial distance. The data comes from four plot lines on a 2D plane section. The plot lines are at 100, 200, 300 and 400 mm distance from the fuel injection nozzle at the top of the combustor. The figure shows the mass fraction of CO as the fluid moved down through the combustor. Note the asymmetry clearly visible at y = -100, -200 and -300 mm plot lines. Symmetry is mostly restored at y = -400 mm. Although showing rapid reduction in mass fraction CO from y = -300 to -400 mm, there is still approximately a mass fraction of 0.03 CO close to the outlet. Longer resident time could solve this.*

4.1.15 Mass Fraction NO_x Profile in Vertical Plane Section and XY Plot

The NO_x emissions are not modelled by the SLF table. They are calculated by a separate model. The 2D plane section, figure 51, shows that NO_x emissions are formed in high-temperature zones such as in the hot core at y = -200 mm and below. Some NO_x is also formed in the zones were the nitrogen from the air stream comes into contact with the elevated temperatures along the inner walls of the flame tube. The mass fraction vs. radial position XY plot, figure 52, shows that the formation of NO_x seems to be less affected by the asymmetry of the design than the other engineering scalar that has been examined. From the figures it is however very clear that the high-temperature core of the combustor needs to be dealt with if NO_x emissions are to be reduced significantly.

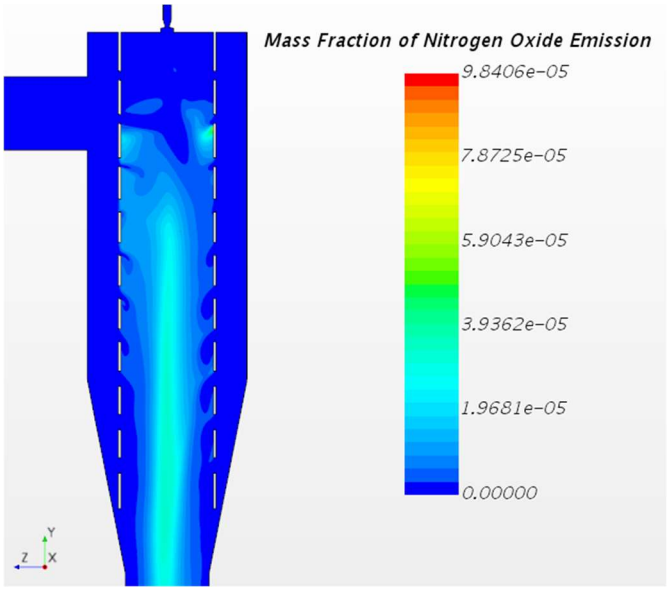

Figure 51: *Figure of 2D plane section showing the formation of NO_x emissions as calculated by the NO_x emissions model.*

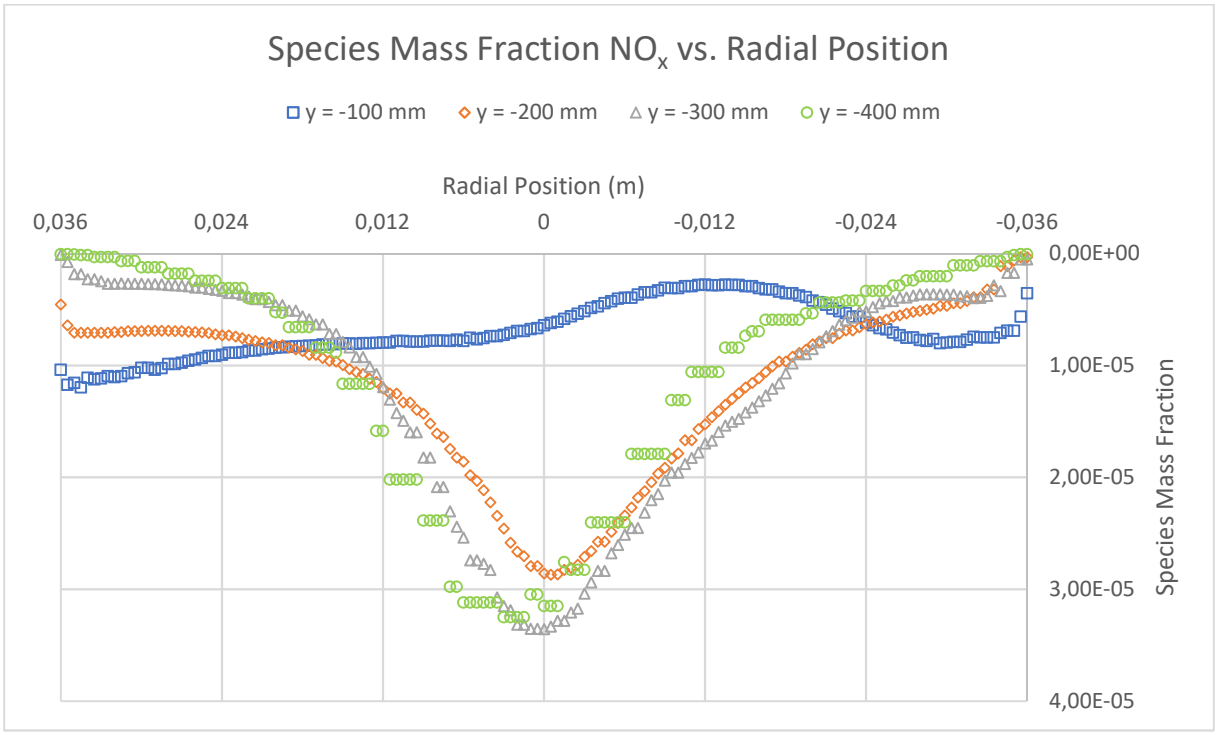

Figure 52: *The figure shows the minor species of NO_x mass fraction plotted against the radial distance. The data comes from four plot lines on a 2D plane section. The plot lines are at 100, 200, 300 and 400 mm distance from the fuel injection nozzle at the top of the combustor. The figure shows the mass fraction of NO_x as the fluid moved down through the combustor. Note how NO_x is formed in the high-temperature core of the flame tube and that much of the NO_x is already formed before the fluid reaches y = -200 mm. This points to very high combustion temperatures.*

4.1.16 Kolmogorov Length Scale & Taylor Microscale

It is common to use a converged RANS solution for initiating a LES or DNS numerical simulation. Initial conditions in the simulation domain will be extrapolated from the RANS solution, speeding up the LES or DNS solution and increase the possibility for a converging solution.

The Kolmogorov length scale and Taylor micro-scales are difficult to calculate prior to model setup. It is common to use a numerical model with RANS to find these scales. This is a useful tool for setting the right cell size to have adequate resolution for capturing the needed details. The Kolmogorov length scale and Taylor micro-scales are provided here to show what is needed for successfully running a LES or DNS numerical simulation. The scale provided here serve as a tool for selecting adequate cell dimensions and time scales. There are also microscales for velocity.

Table 16: *This table provides an overview of the Kolmogorov length scale, time scale and Taylor microscale. The purpose is to show the orders of magnitude difference needed to run LES and DNS numerical simulation accurately.*

Scale	**Minimum**	**Maximum**
Kolmogorov length scale (m)	8.2970×10^{-7}	4.3837×10^{-3}
Tayor microscale (m)	4.0262×10^{-6}	9.6507×10^{-4}
Base cell size in this RANS model (m)	5.0×10^{-5}	2.0×10^{-3}
Kolmogorov time scale (s)	6.9066×10^{-8}	0.60213

The base size for this RANS model is 2.0×10^{-3} m, minimum 5.0×10^{-5} m in the small refinement zone around the fuel injection nozzle with the highest resolution. There are no timesteps in steady-state RANS simulations. Considering the minimum cell size to resolve the Kolmogorov length scale and Taylor microscale it is clear at LES modelling requires on order of magnitude decrease in cell size and DNS requires an additional order of magnitude decrease in cell size. Considering that the numerical model is three dimensional the required cell size would increase by many orders of magnitude. The computer power needed to resolve this is not readily available. If LES or DNS is to be used only a very small section could be examined. Since there are no symmetry lines boundary conditions could be supplied from a RANS simulation and described by field functions.

4.2 Results for Case 2

The results for case 2 will not be presented with the level of detail as case 1. The reasoning behind this is that this is a design suggestion. The model needs additional refinement and optimization. This is an iterative process that has not been possible in the given timeframe. Instead of focusing purely on the results, the data will be presented with regards to relative differences and what can be learned from these differences.

4.2.1 Sampling Points

The sampling points resemble case 1 as closely as possible to make the comparisons relevant. Refer to section 4.1.1 and figures 31 and 32 for placement details. One major change had to be made. The plane section and plot line for y = -400 mm has been removed from the model because the combustor in case 2 is shorter than in case 1. The combustor outlet plane is located at y = -380 mm. This total length is 40 mm less than in case 1. The other sampling points are at the same positions.

4.2.2 Converged Values for the Engineering Scalars

Table 17: *The table provides the values for selected engineering scalars from simulation case 2. Du to some combustion fluctuations the values are an average of the last 1,000 iterations.*

Parameter	**Location**	**Value**	**Unit**
Minimum absolute pressure	Measurement points	197,792	Pa
Maximum absolute pressure	Measurement points	197,852	Pa
Minimum absolute pressure	Combustor outlet plane	194,934	Pa
Average absolute pressure	Combustor outlet plane	197,857	Pa
Maximum absolute pressure	Combustor outlet plane	205,819	Pa
Minimum temperature	Measurement points	1412.6	K
Maximum temperature	Measurement points	1815.6	K
Minimum temperature	Combustor outlet plane	365.8	K
Average temperature	Combustor outlet plane	913.6	K
Maximum temperature	Combustor outlet plane	1812	K
Minimum velocity	Combustor outlet plane	77.9867	m/s
Average velocity	Combustor outlet plane	135.8069	m/s
Maximum velocity	Combustor outlet plane	208.5185	m/s
Combustor outlet mass flow rate	Combustor outlet plane	-0.19421082	kg/s
Mass fraction O_2	Combustor outlet plane	0.19282966	Dimensionless
Mass fraction C_3H_8	Combustor outlet plane	3.5128×10^{-6}	Dimensionless
		~3.51	ppmw
		$\sim 6.822 \times 10^{-4}$	g/s
Mass fraction CO	Combustor outlet plane	1.57367×10^{-3}	Dimensionless
		1574.67	ppmw
		~0.306	g/s
Mass fraction NO_x	Combustor outlet plane	1.1527×10^{-6}	Dimensionless
		~1.15	ppmw
		$\sim 2{,}239 \times 10^{-4}$	g/s

4.2.3 Vertical Plane Sections Scalar Scenes

Scalar scenes from a 2D plane section running through the centreline of the combustor are provided. These scenes are not discussed in detail as for case 1. The reason for this is that case 2 has more focus on comparison with case 1 to evaluate the relative changes in the numerical model. The 2D scaler scenes are not an accurate tool for these comparisons because the geometries are different, and the colour contours do not provide an adequate level of detail. Comparisons would be subjective.

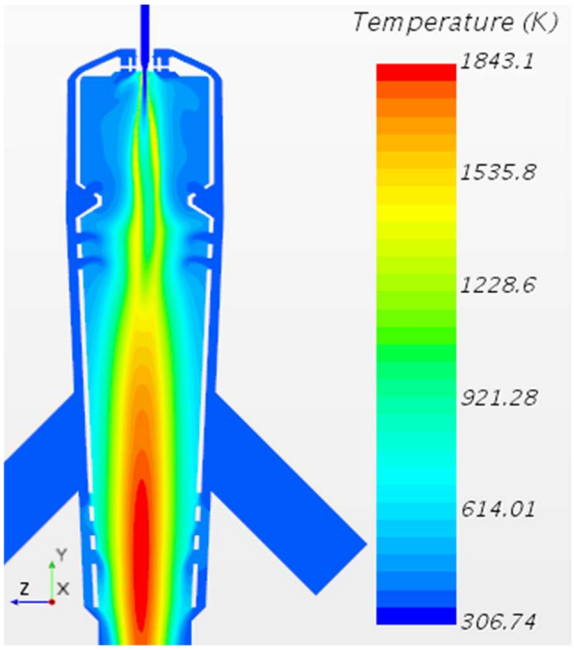

Figure 53: *Temperature plane section scalar scene. Note that the highest temperatures are reached close to the combustor outlet. This suggest insufficient dilution.*

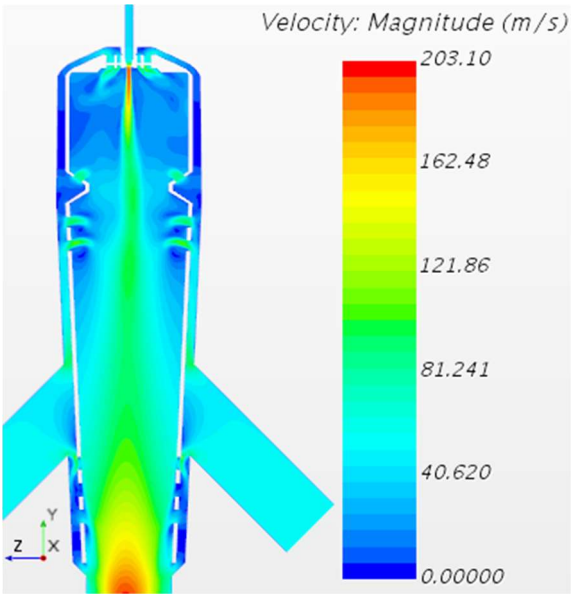

Figure 54: *Velocity plane section scalar scene. Note the symmetry of the field and how the velocity field grows from the primary combustion zone towards the combustor outlet.*

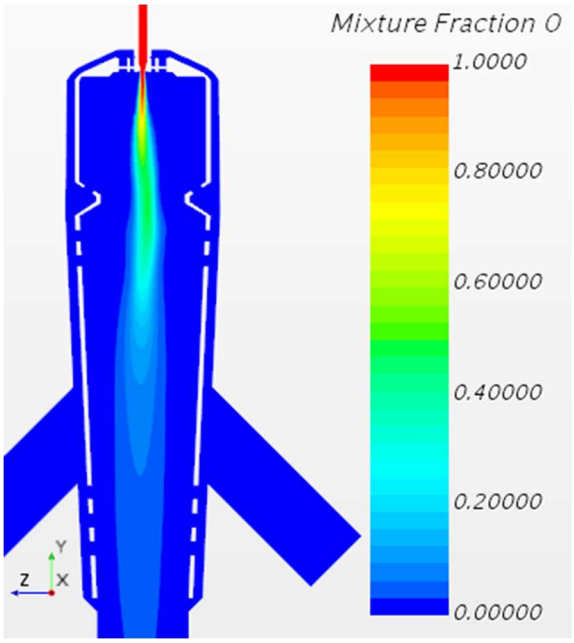

Figure 55: *Mixture fraction plane section scalar scene. Note that the combustion is not contained in the primary combustion zone.*

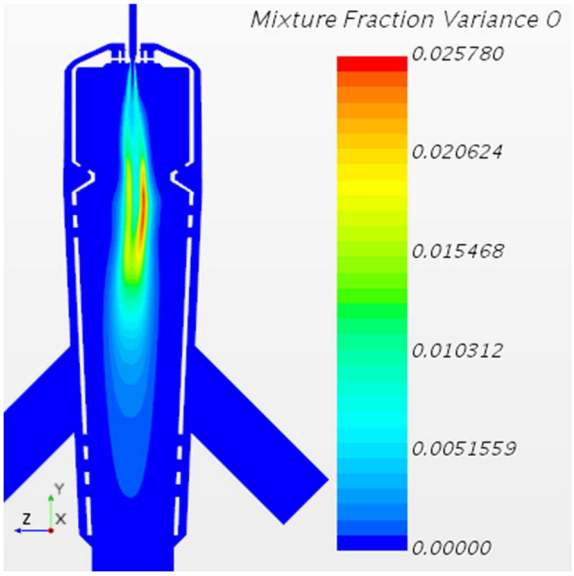

Figure 56: *Mixture fraction variance plane section scalar scene. The variance has the highest value outside the primary combustion zone.*

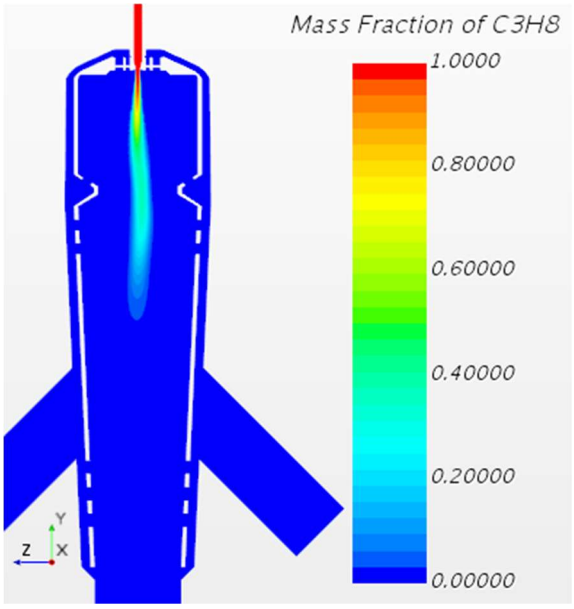

Figure 57: *Mass Fraction C_3H_8 plane section scalar scene. The mass fraction of fuel is still high outside the primary combustion zone.*

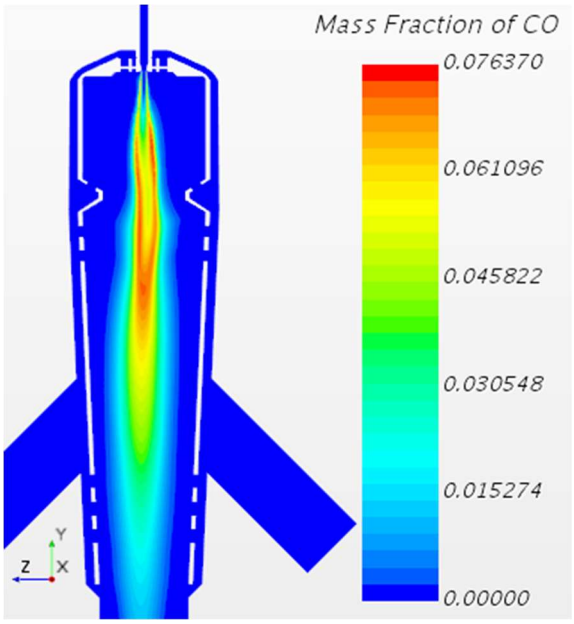

Figure 58: *Mass Fraction CO plane section scalar scene. The mass fraction of CO is a good indication of unfinished combustion. This plane section shows that combustion starts in the primary zone and that it is not contained. This is the reason for the high CO emissions at the combustor outlet.*

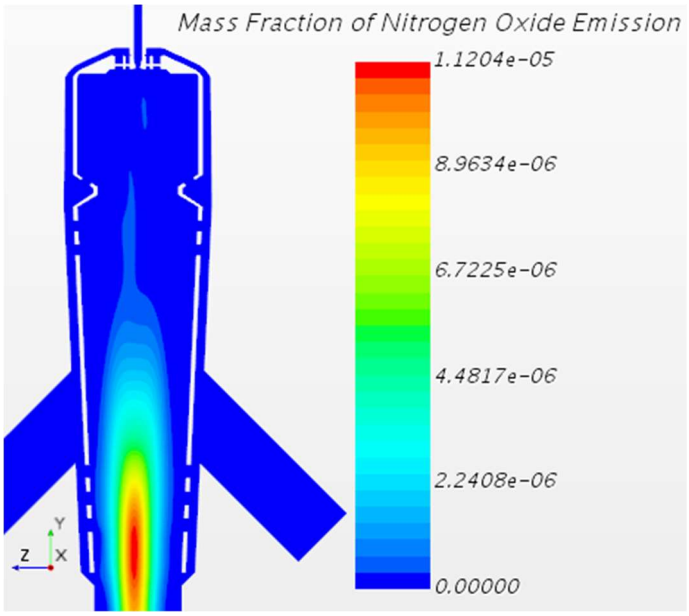

Figure 59: *Mass fraction NO_x plane section scalar scene. The NO_x emissions are primarily formed in the high temperature core close to the combustor outlet. This shows that more dilution air is needed in this region.*

4.2.4 Engineering Scalars Comparison

The engineering scalars have been compared between case 1 and 2. An overview of the comparison is presented in this section.

There is a higher loss of pressure in case 2 compared to case 1. The average values at the combustor outlet shows a pressure drop of 2894 Pa. This corresponds to a change of -1.44 % compared to case 1. When comparing the maximum and minimum values for the combustor outlet with the air inlet pressure, case 2 has a pressure loss of between 6,87 % and 11.79 %. For case 1 the loss is between 8.50% and 9.44%. The higher loss in pressure for case 2 is likely caused by the aerodynamic changes introduced by the more complex geometry and the swirler. These additions result in increased pressure loss due to turbulence effects and skin friction.

For the measurement points the minimum and maximum measurement points show a much smaller span. The span is 403 K, compared to the 727.8 K span for case 1. The maximum temperature is 185.6 K lower for case 2. The minimum temperature is 138.9 K higher for case 2. This suggest that the temperature is better distributed throughout the cross-sectional area of the flame tube in case 2.

The same trend can be seen for the scalar for combustor outlet temperature. Maximum temperature is reduced by 158 K. Average temperature is increased by 35.1 K. The minimum temperature is reduced by 22.9 K. Lower peak and higher average temperatures suggests a more even temperature distribution. Lower peak temperature values will reduce the possibility of damaging the turbine, turbine blades or the metal of the combustor and piping. Because NO_x formation is highly temperature dependent lower emissions are expected.

The combustor outlet velocities are lower for case 2. The maximum velocity is reduced by 5.6 m/s and the minimum by 22.3 m/s. The average outlet velocity is reduced by 2.1 m/s. This is a drop of -1.56 % for average velocity.

The mass fraction of unburnt fuel is very similar for case 1 and 2. There is an insignificant drop from 3.79 to 3.51 ppmw. This is more likely caused by small fluctuations rather than an actual difference. Mass fraction CO is still very high, showing a small increase. This suggest that the swirler and orifice are not successful in increasing the resident time inside the combustor.

Mass fraction NO_x is significantly reduced from 3.90 to 1.15 ppmw. This corresponds to a 70.5 % reduction. This can be a consequence of the observed reduction in peak temperatures. It can also be influenced by the reduced length of the combustor in case 2. Shorter resident time with exposure to high temperature can have an effect. It should however be noted that mesh independence for NO_x could not be confirmed for case 2.

4.2.5 Temperature Profile XY Plot Comparison

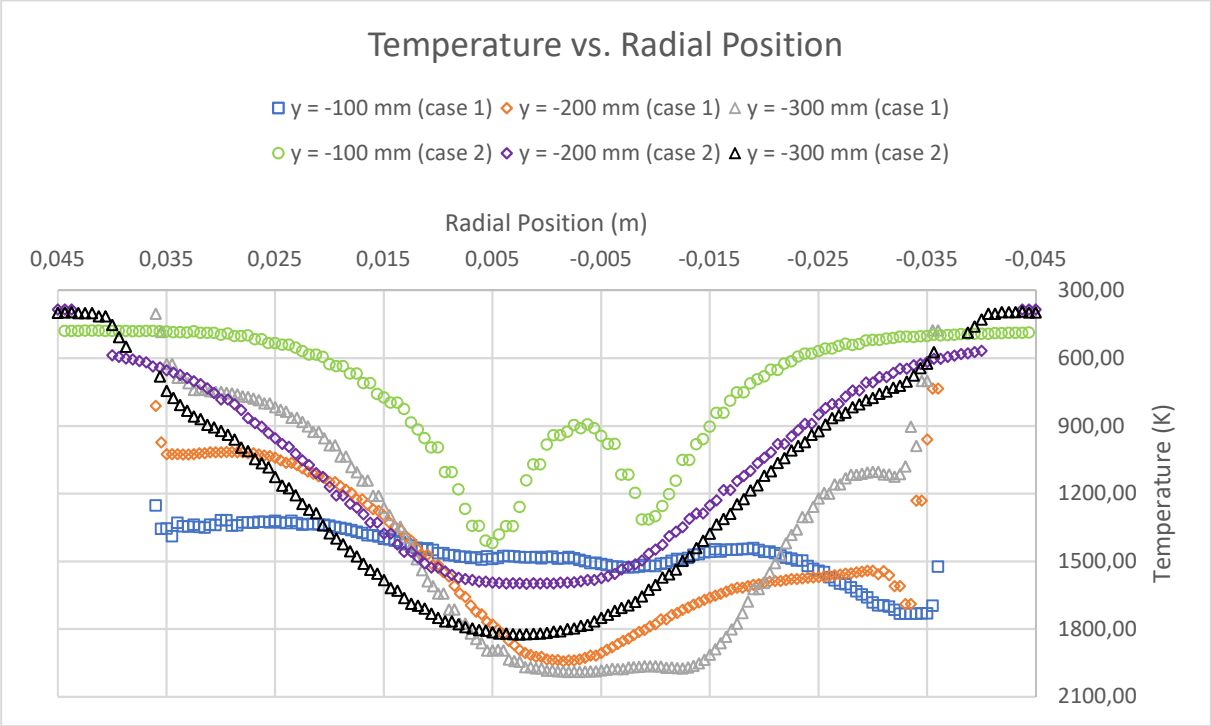

Figure 60: *This figure shows a comparison between the temperature profile from the probe lines at y = -100, -200 and -300 mm for case 1 and 2. Note the lower temperatures for all probe lines for case 2 compared to case 1. The peak temperature for probe line y = -300 mm is still too high with regards to NO_x emissions. Also note the W-shape of the profile at y = -100 mm for case 2. This effect is a result of the swirler device and the air directed towards the primary combustion zone. The symmetry for case 2 is significantly improved compared to case 1.*

The temperature profile from the probe lines show that the temperatures for case 2 are lower for all three positions when compared directly with the same position for case 1. This should affect NO_x generation at all three levels in the combustor. This corresponds very well with the mass fraction NO_x scalar scene, figure 59. The peak temperatures for y = -300 mm are too high and should be reduced by adding additional cooling by dilution air. It is also worth noting that the width of the temperature profile has improved, suggesting a more even temperature distribution and less formation of a jet flame.

The W-shape of the temperature profile at y = -100 mm is also worth noting. This shows the effect of the swirler and the airflow that is directed back at the primary combustion zone. In [15] Mallouppas et al. points out this characteristic shape for the flame on the dry low emissions combustor Siemens SGT-100. Figure 59 indicates that this dry low NO_x feature has the desired effect in case 2.

It is also clear from the comparison that case 2 has superior symmetry compared to case 1. This shows that splitting the air supply from the compressor into two pipes will improve symmetry significantly, especially when mounted in a counter-flow direction. Krieger at al [18] showed that there was still some asymmetry in a similar design with only one air inlet. The temperature profile suggest that two symmetrically mounted air inlet pipes can add additional improvement.

4.2.6 Combustor Outlet Profile XY Plot Comparison

As seen in the engineering scalar comparison the temperature profile at the combustor outlet shows reduced peak temperatures. This effect is desired because these high temperatures will cause the turbine to malfunction. The turbine blades cannot handle the temperature and other parts, such as

bearings and metal surfaces can also be damaged. It is unlikely to be reliable for long operation. Case 2 shows peak temperature of approximately 1800 K. This is also to high. More dilution air is needed to bring the temperatures lower. The combustor outlet temperature should be designed to be within the maximum specifications of the turbine. These specifications are not available for the HVL GTE turbine. This needs to be considered prior to prototyping a new combustor for the GTE.

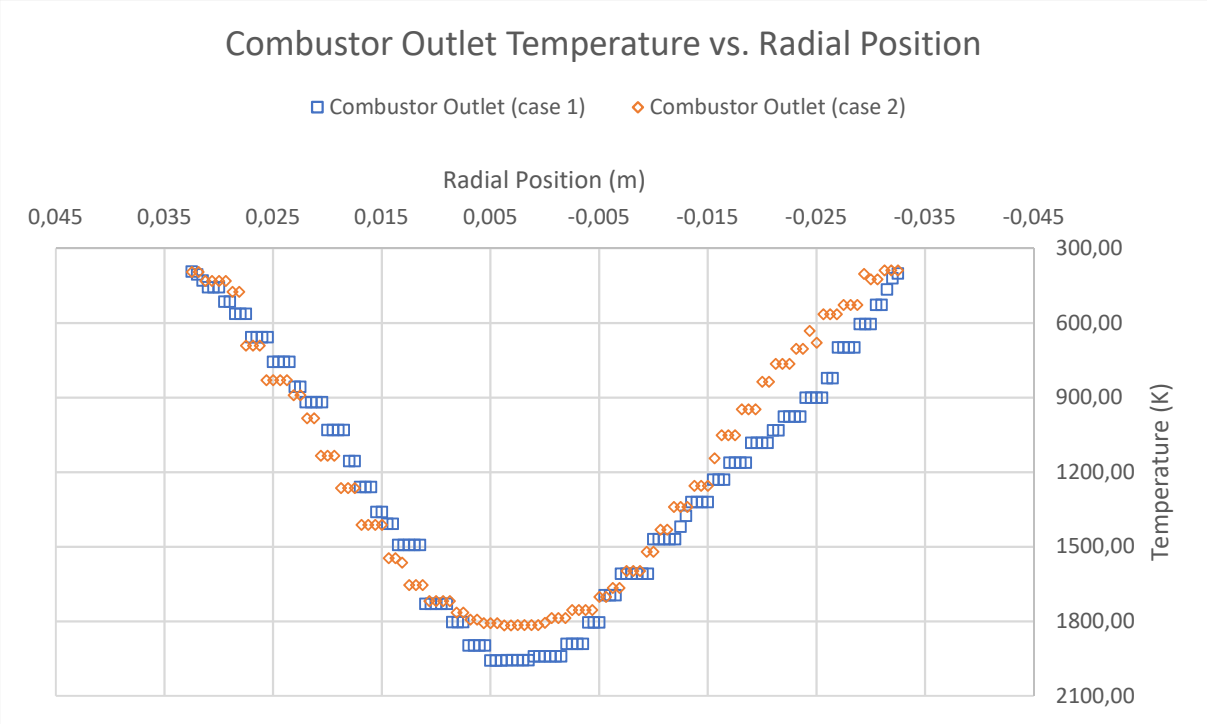

Figure 61: *This figure shows the combustor outlet temperature profile based on the probe lines at the combustor outlet for case 1 and 2. The significant difference is that case 2 has lower peak temperatures than case 1. The peak temperatures are still too high and need to be reduced by additional dilution air.*

4.2.7 Velocity Profile XY Plot Comparison

The velocity profile shows that velocities are higher for all three probe lines for case 2 compared to case 1. The velocity field is also more evenly distributed. The comparison between the probe lines for y = -100 for case 1 and 2 are especially noteworthy of comparison. For case 1 the probe line shows unevenness and asymmetry. For case 2 it is symmetrical. The orifice in the flame tube contributes to the observed acceleration. The acceleration is wanted, but ideally should not happen prior to a majority of the fuel being combusted. In this case the acceleration happens to early. This can also be seen from the mixture fraction profile plane section, figure 55.

The combustor outlet velocity, figure 63, shows that case 1 has higher velocities than case 2. High velocities are wanted to run the turbine. One reason for the observed higher velocities is likely to be the more aggressive convergent nozzle shape of the combustor casing in case 1.

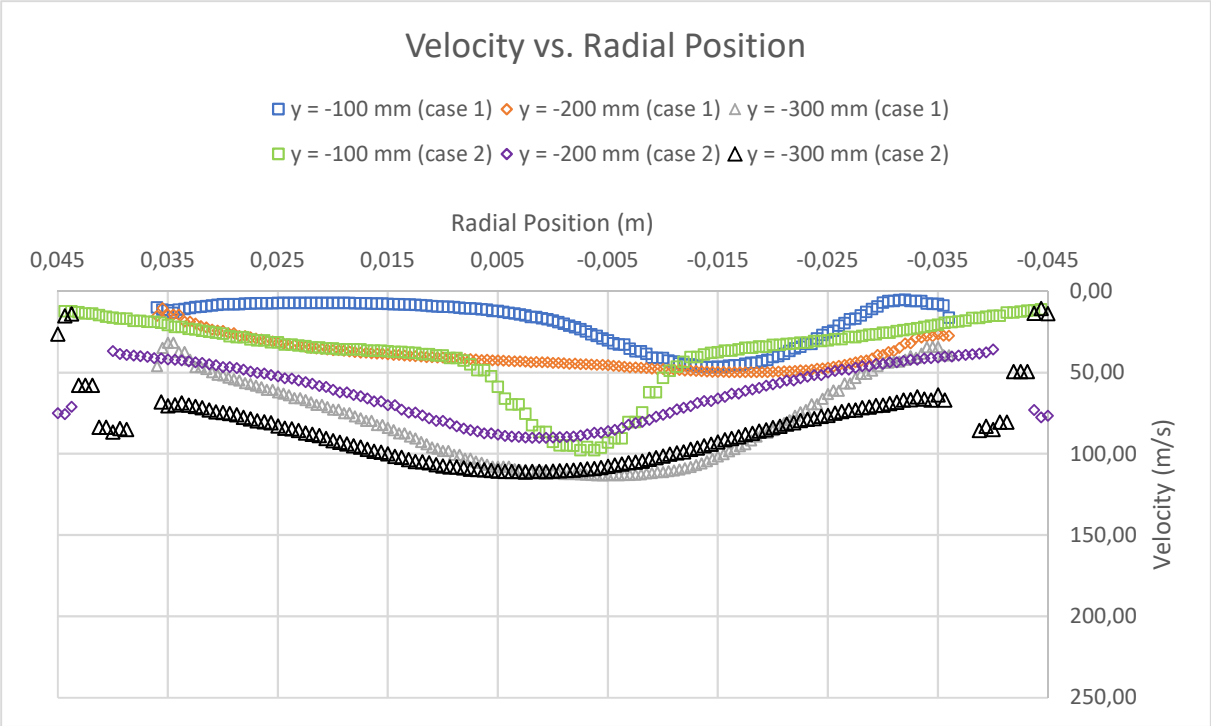

Figure 62: *The figure shows the velocity vs. radial position at the probe lines. Note that velocities are higher for case 2 at all probe lines compared to case 1. The probe lines for y = -100 mm are especially noteworthy due to the asymmetry and unevenness of case 1 and the symmetrical high velocity profile of case 2. For case 2 the acceleration is happening to soon and is prior to adequate combustion of the fuel.*

4.2.8 Combustor Outlet Velocity Profile XY Plot Comparison

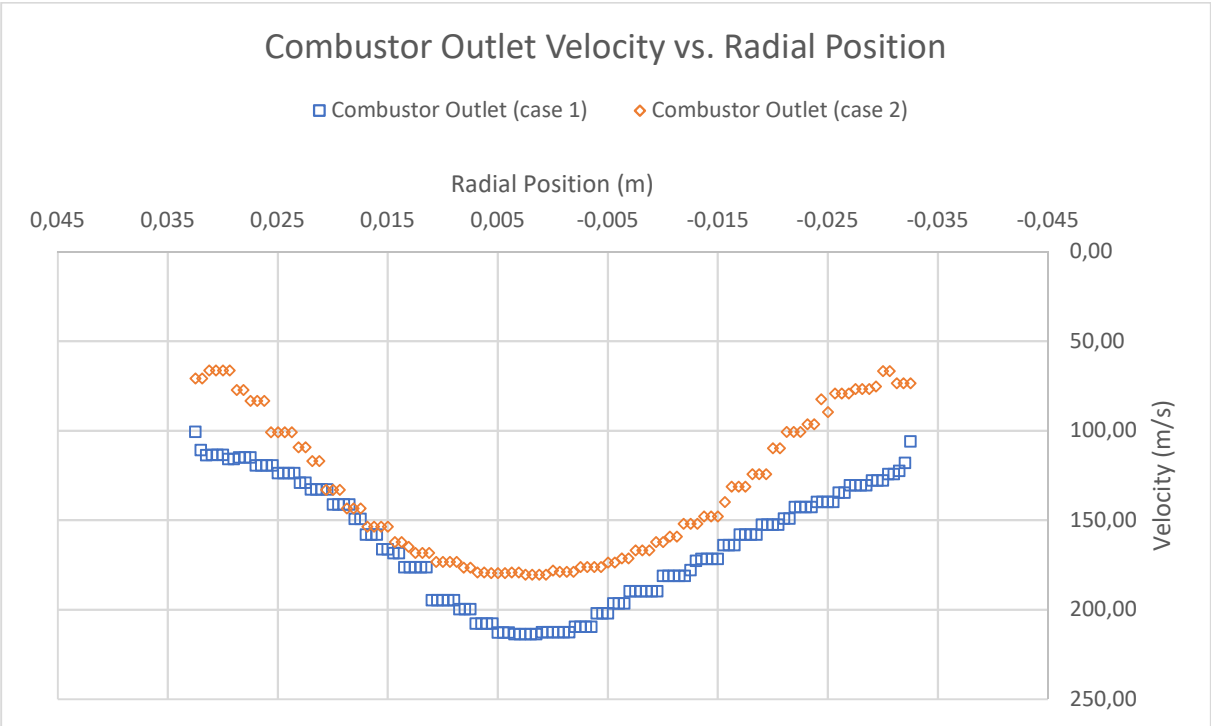

Figure 63: *This figure shows the velocity profile at the combustor outlet. Case 1 has higher velocities than case 2. The difference might be caused by the more aggressive convergent nozzle shape of the combustor casing in case 1.*

4.2.9 Mixture Fraction Profile XY Plot Comparison

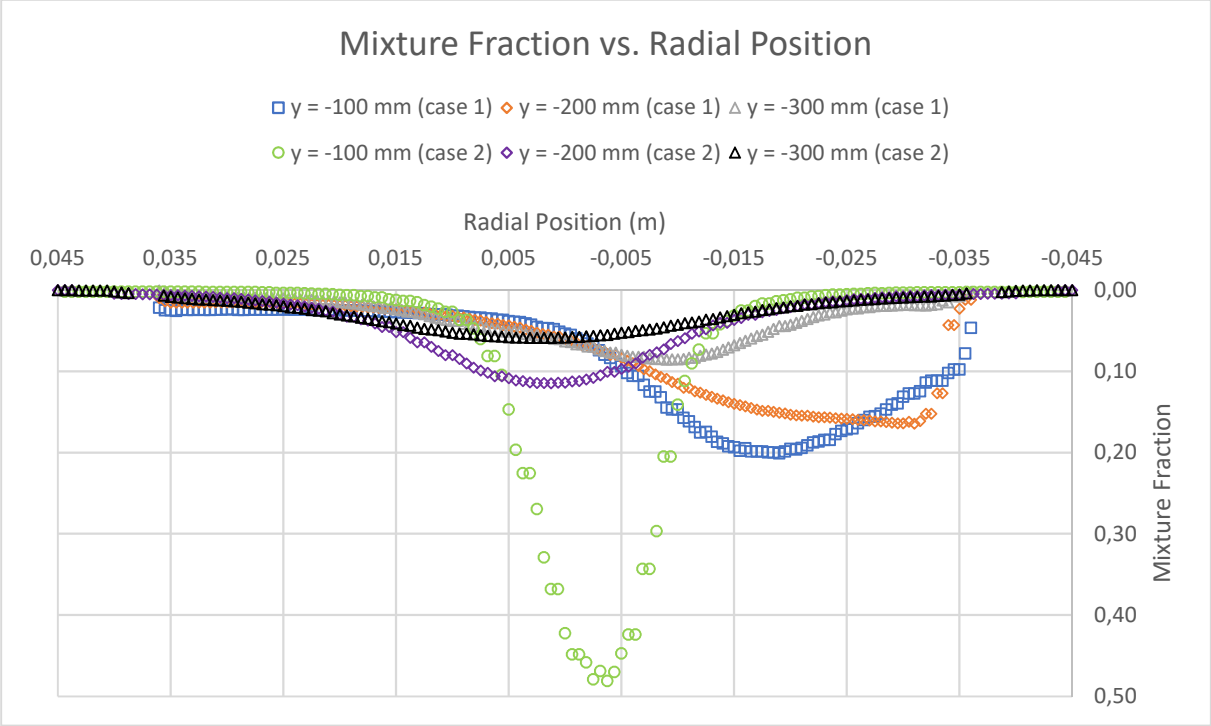

Figure 64: *This figure shows the mixture fraction profile. The most noticeable is the core of fuel rich fluid that passes y = -100 mm and into the secondary combustion zone. This concentration of fuel moved to rapidly for through the primary zone for adequate obtain adequate diffusion for combustion.*

The high mixture fraction at y = -100 mm for case 2 shows that combustion at this location is far from completed and viewed with regards to the high fluid velocities observed at the same position this is not ideal. This shows that much of the combustion process takes place in the secondary combustion zone. The reason for this can be that the swirler device does not create enough turbulence for mixing of fuel and air. There is a concentrated core of fuel that needs more efficient diffusion or additional time to accomplish the same. The observed effect is probably due to the high fuel injection pressure, small orifice of the injection nozzle and not enough spread in the spray of fuel from the injection nozzle. The consequence is a rapid acceleration of the fuel prior to entering the combustion chamber. This kinetic energy drives the fuel rapidly past the primary combustion zone without enough resident time for diffusion. The length dimension of the primary combustion zone might also be too short and the orifice of the combustor to narrow. It is also worth noting the improved symmetry for case 2 compared to case 1.

4.2.10 Mass Fraction C_3H_8 Profile XY Plot Comparison

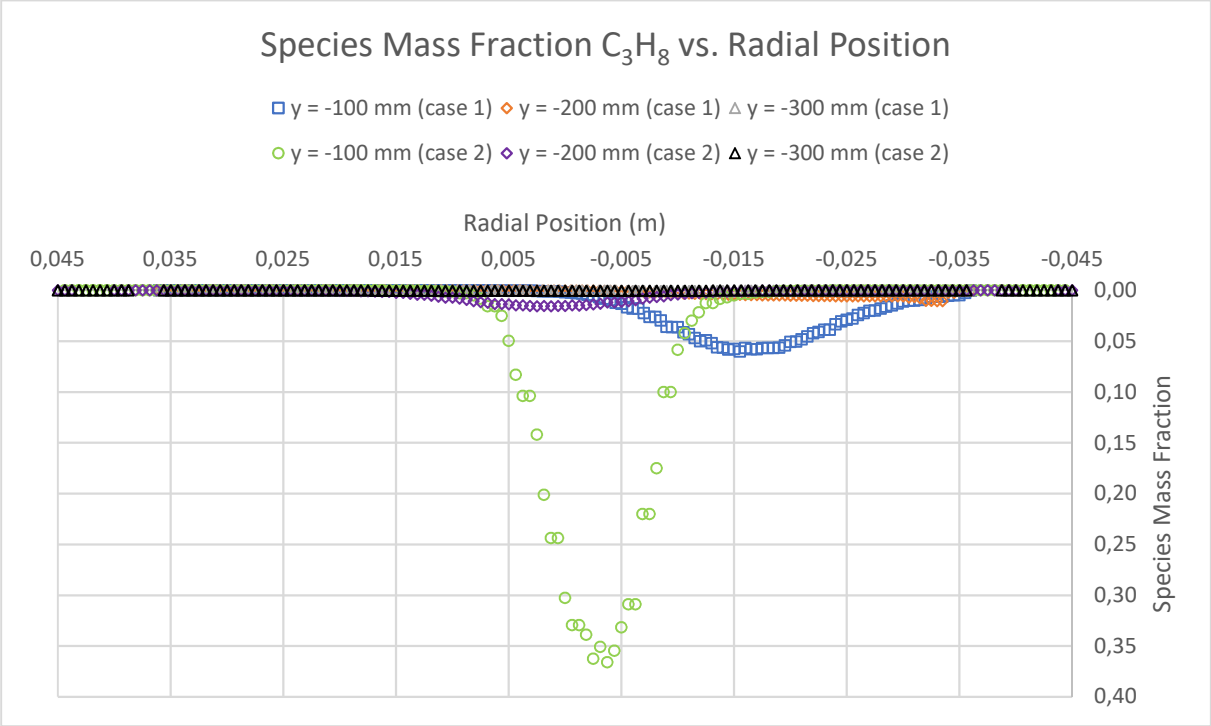

Figure 65: *This figure shows the species mass fraction of fuel. The high mass fraction of C_3H_8 indicates that a large portion of the fuel has not started the combustion process due to inadequate diffusion during the fluid resident time in the primary combustion zone. It is interesting to note that the mass fraction is rapidly reduced prior to y = -200, indicating a rapid reaction rate in the secondary combustion zone.*

The species mass fraction profile for C_3H_8 shows the same tendency as the mixture fraction profile. There is a core with high concentration of unburnt fuel at the centre of y = -100 for case 2. The mass fraction at this probe line is much higher for case 2 than for case 1. This shows that a large part of the fuel has not started the combustion process. Since this is a case of non-premixed combustion the fuel need to diffuse with the air prior to combustion. The resident time of the fluid in the primary zone is likely to short. There is also the possibility that the mass fraction of Oxygen (O_2) is too low in the primary zone, preventing effective diffusion. If that is the case, this is more of a rich burn quick quench design. To examine this more closely a mass fraction profile XY plot for O_2 is provided in subsequent section.

4.2.11 Mass Fraction O_2 Profile XY Plot

The XY plot for O_2 concentration vs. radial position is interesting in that is shows that the oxidiser does not penetrated the core of the injected fuel stream. For additional information a probe line for y = -50 mm is provided in figure 66. This position is two thirds along the length of the primary combustion zone from the fuel injection. Mixture fraction 0.00 at the centreline shows that no oxidiser is present at this position. The mixture fraction rapidly increases to approximately 0.23 when moving away from the centreline in both directions. This shows that the swirler device is not successful in promoting adequate diffusion of fuel and oxidiser. The figure also sheds light on the rapid reaction rate between y = -100 mm and y = -200 mm. In this zone the fuel is rapidly diffused due to high temperatures and that additional oxidiser penetrates the concentrated core of the fuel stream. In this zone the combustion could be described at partially pre-mixed. Based on the O_2 profile it is possible to consider this as a variant of a rich burn quick quench design, tough the mixture at the centre of the

combustor is too rich. Rich burning quick quenching is a viable option, but the mass fraction O_2 should be more than zero at the centre of the combustor.

This also explains the slightly fluctuating non-steady state values of the engineering scalars and the behaviour seen in the residuals plot, figure 27. These indicate that the combustor would not be operating smoothly. There would be fluctuations in the combustion, resulting in vibration and noise. The design needs to be improved, most likely the swirler design is to blame, but also the high injection pressure of the fuel. During the initial stages of the design as similar behaviour was discovered. The dimensions of the gap between the flame tube and the casing was increased to provide additional air to the swirler. This did not change the behaviour, suggesting that it is not the mass flow of air to the primary zone that is the problem, but that it is the swirler and how it is design and behaves in the numerical model. The counter-flow design of the air inlet and the dilution holes can also have an effect.

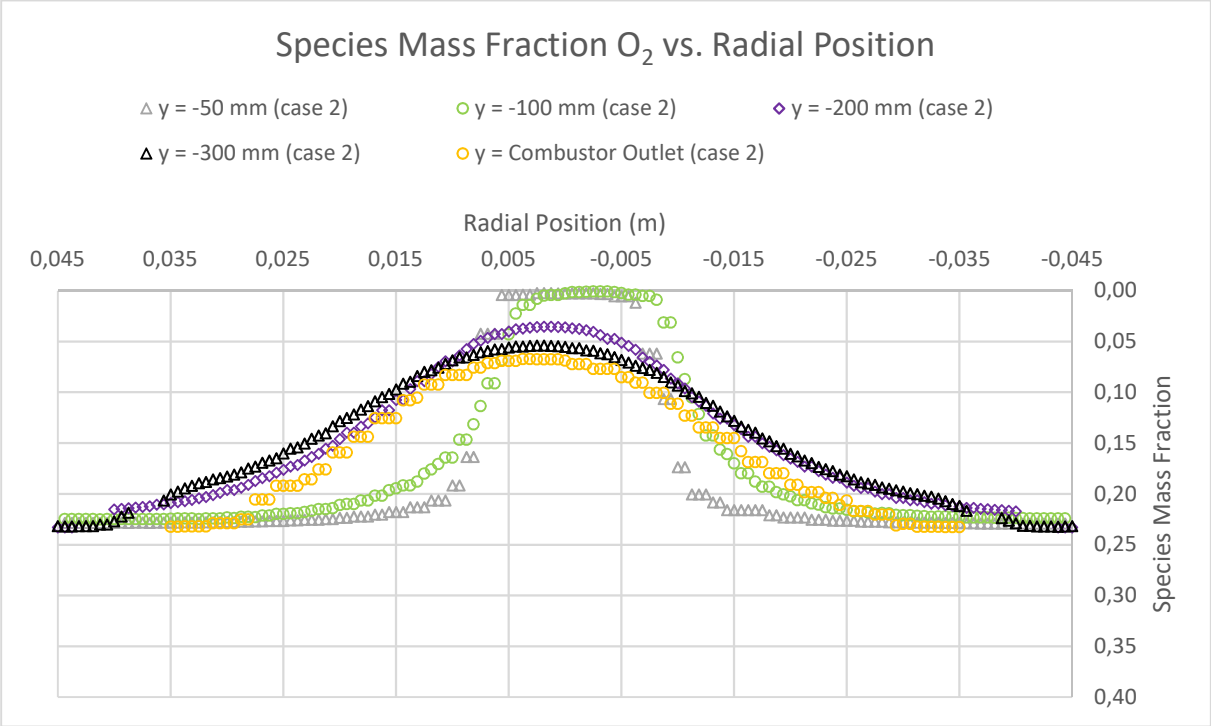

Figure 66: *This figure shows the O_2 mass fraction at the probe lines at y = -100, -200 and -300 mm. Additional lines are provided for y = -50 mm and at the combustor outlet. The probe lines show that oxidiser does not penetrated the core of the injected fuel spray as shown by a mixture fraction of 0.00 at the centreline for both y = -50 and -100 mm. This suggests a problem with the swirler design and with the shape of the spray of injected fuel. This plot explains the non-steady-state fluctuation experienced in the simulation. The probe lines at y = -200 and -300, show that the oxidiser does diffuse with the fuel in the secondary and tertiary zone.*

4.2.12 Mass Fraction CO Profile XY Plot Comparison

The presence of CO indicates that the combustion process is started. Figure 67 shows a distinct W-shape at y = -100 mm. This corresponds to the same shape for the temperature profile at this location. This shows a diffusion flame at this location. Case 2 has much better symmetry than case 1. In case 1 a majority of the combustion takes place mostly to one side of the combustor and in close proximity to the wall. Symmetry is superiors for case 2 at all three probe lines. The mass fraction CO is too high at y = -300 mm for both cases even though case 2 shows improvement over case 1. The resident time before the fluid reaches the outlet is still too short. The resident time needs to be increased either by

reducing velocity or by extending the total length of the combustor. Ideally the mixture fraction CO should be close to zero at y = -300 mm if the current length is maintained. Incomplete combustions and high CO emissions are a major problem with both designs and the scalar value at the outlet shows no improvement for case 2 over case 1.

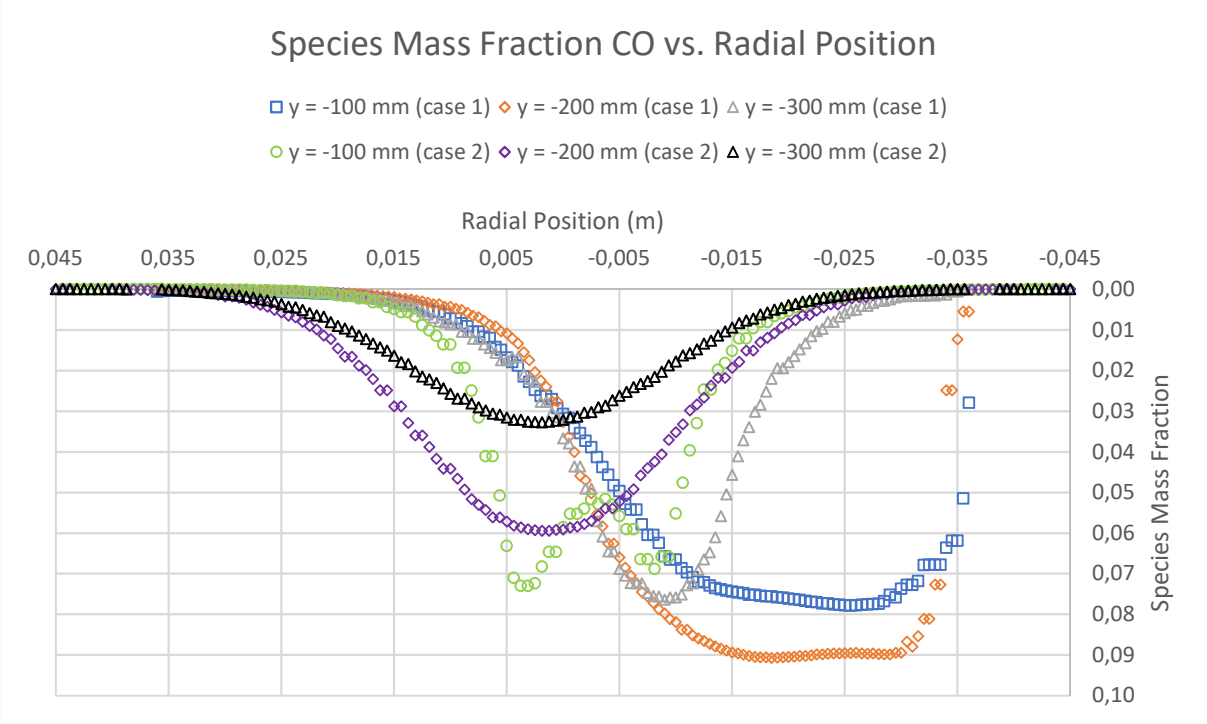

Figure 67: *This figure shows the probe lines for mass fraction CO vs. radial position. The distinct W-shape of the diffusion flame at y = -100 mm for case 2 corresponds to the shape observed for the temperature probe line at the same position. It is also worth noting the superior symmetry of case 2 over case 1. The probe lines at y= -300 mm shows to high mass fraction of CO close to the combustor outlet. This should ideally be close to zero at this location if current combustor length is to be maintained.*

4.2.13 Mass Fraction NO_x Profile XY Plot Comparison

The NO_x performance probe lines look superior for case 2 over case 1 and show the same results as evident from the scalar values for NO_x at the outlet. These showed a 70.5 % reduction in NO_x emissions. This is achieved by implementing the dry low NO_x method of rich combustion in the primary zone and quenching with additional air in the secondary zone. This reduces the combustion temperature in the primary and secondary zone. Dry Low NO_x was one of the design goals set for case 2. This has been accomplished. At probe lines y = -100 and -200 mm the mass fraction NO_x is close to zero which is very good for the primary and secondary combustion zone. There is build-up of a high-temperature core closer to the outlet as shown in the temperature 2D plane section, figure 53. This causes NO_x formation close to the outlet shown in the NO_x plane section, figure 59. The trend of increasing NO_x formation is shown by the probe line at y = -300 mm for case 2 and increases even more closer to the outlet. This corresponds well to the findings of Mallouppas et al. [15], who showed that much of the NO_x in the Siemens SGT-100 is formed close to the combustor outlet or just outside the outlet. This is an argument for that also the turbine inlet needs to be modelled as part of the combustor to give more accurate predictions. Additional or more efficient dilution is needed to cool the tertiary zone to reduce this trend.

With regards to lower NO_x emissions the probe lines show some good design elements that show promise for future design iterations. For this work additional mesh sensitivity for NO_x emissions should also be performed to confirm accurate results.

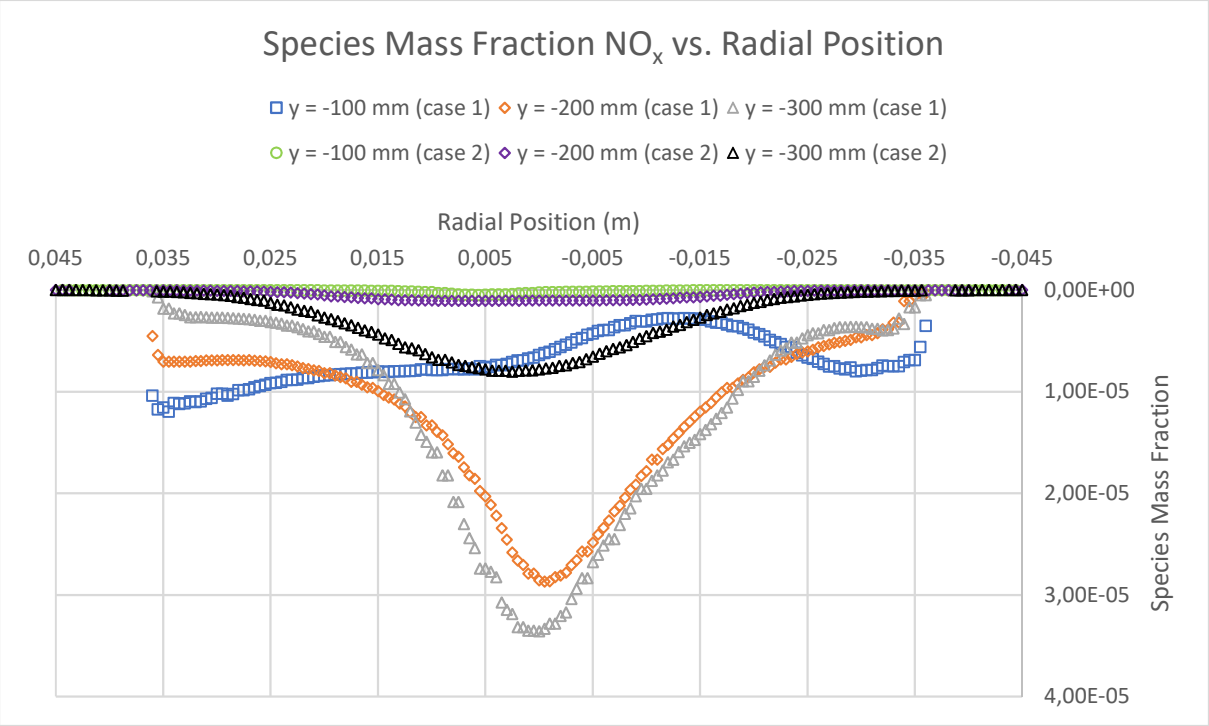

Figure 68: *This figure shows the mass fraction NO_x vs. radial position. The NO_x emissions are superior for case 2 compared to case 1. This is because design elements for dry low NO_x methods have been implemented in the design. The results show promise. The rise in mass fraction NO_x at y = -300 mm for case 2 can be improved by additional or more efficient dilution to reduce fluid temperatures close to the combustor outlet.*

4.3 Additional Discussions

Validation of the model for case 1 is a weak point in this work, but because of limits to the available timeframe additional experimental measurements were not possible. Also, during the 2017 test run a bearing in the turbine or compressor was damaged, so new experimental data was not an option. The validation has been performed based on the data available to me through previous work. It is also important to point out that a numerical model can never perfectly describe the physical world, but the result should be accurate enough to provide good insight into results that are otherwise unavailable or very difficult to show experimentally. It is this authors opinion that the numerical models presented here serve that purpose. Furthermore, using the admittedly somewhat weakly validated model for case 1 as a basis for case 2 at least improves the likelihood of this case also being valid. All the same modelling principles are used.

Based on the numerical values and the assumptions that the results are valid, case 2 is in my opinion a better design than case 1. Case 2 bring improvement to combustion temperature, outlet temperature and NO_x, while other scalars are similar to case 1. No scalar is particularly worse, although the fluctuations caused by too little oxidiser penetration into the primary combustion zone needs to be addressed. I am satisfied with the achieved results, even though the design is not ready for prototyping and model validation. That could probably not be expected in the given timeframe of the work.

I would have liked to try the following potential improvements to the design:

Adding between 100 and 200 mm length to the combustor. I expect this would result in a rapid reduction of CO emissions due to longer resident time for the fluid. If length is added to the combustor without adding additional dilution air, the high temperatures will likely increase NO_x generation.

Adding a diffusor such as a volumetric expansion to the fuel inlet nozzle. This would reduce the velocity of the injected fuel. The effect of the turbulence created by the swirler could change the fuel diffusion characteristics significantly. More of the fuel is predicted to react in the primary zone. Decreasing the fuel inlet pressure could have a similar effect and should be tried.

Adding additional dilution air by adding additional holes in the tertiary zone. I would also have like to try and raise the air inlet pressure with 0,5-1 bar and increase the mass flow rate from the air inlet boundary. Reduced combustion temperatures are expected, especially in the primary zone. Increased inlet pressure could also positively affect the turbulence and mixing created by the swirler.

4.4 Suggestions for Future Work

There are a lot of potential possibilities for future work based on the results provided. Some possibilities for future projects are presented in this section.

The obvious possibility is to continue to improve the numerical model created for this work and implement the suggestions for further improvement. The models created by me will be made available for this purpose. The numerical model should also include the turbine inlet for improved accuracy. Optimization should also be performed to find ideal dimensions, shapes and boundary conditions. The next step would be to build a prototype and validate the model.

Another CFD project could be to look at the design of the fuel injection nozzle and the swirler device. How can the shape and aerodynamics be improved to enhance mixing and reaction rate? Reducing excessive fuel injection pressure and velocities would also be a natural point of interest.

As for the HVL GTE physical setup there is a lot of room for improvement. The first step could be to improve the fuel supply system for a steady flow with accurate regulation and instrumentation. The possibility for the use of other fuels such as methane or biogas could also be examined. The system could be converted to premixed combustion and reliable ignition is needed. A second option for improvement is the instrumentation. More measurements with improved accuracy is obviously needed for accurate model validation and reliable research results. A third option is to rebuild the compressor and turbine coupling. These are directly coupled, which results in that air mass flow rate and air supply pressure is a function of the turbine work. For research purposes it would have been better to be able to regulate the compressor and the fuel supply independently.

5.0 Conclusion

This work has shown how a numerical model was built using STAR-CMM+ and how the quality of the model and insensitivity to resolution was checked. The numerical model is of good quality. Validation proved difficult due to limited measurements and instrumentation accuracy in previous experimental work. The results extracted from the numerical model are within the wide span of the experimental measurements. This supports some validation of the model.

The numerical model for the existing combustor, case 1, shows the limits of the design and is an argument for why a simple perforated flame tube and straight outer casing is not a good way to construct a simple and cheap microturbine combustor. The off-centred and asymmetrical placement of the air inlet is the cause for the asymmetry observed in the engineering scalars. The combustor has very high peak combustion temperatures, hot streaks along the walls and a very hot jet flame is formed that is unaffected by the dilution air in the tertiary zone. This causes NO_x formation that could be avoided. The numerical model shows very high levels of CO emissions and some UHC. The high levels of CO show incomplete combustion due to short resident time for the fluid inside the combustor. High fuel injection velocities contribute to this.

Another design concept is modelled for case 2 and relative differences between the two cases are examined. Case 2 implements the dry low NO_x method of rich combustion followed by quick quenching with excess air in the secondary zone. The model shows very good improvement of NO_x formation due to lower combustion temperatures. Some combustion instability was observed, likely caused by insufficient penetration of oxidiser at the centre of the primary combustion zone. Although combustion has been improved, case 2 still suffers from very high CO emissions due to short resident time. The increased aerodynamic complexity of the swirler device and geometry of the combustor added in case 2 also resulted in an increased pressure loss for this design. The results show that the design suggestion for case 2 has promise, but that it needs further improvement and optimization before prototyping and validation of the model can be recommended.

References

1. Ehrlich, R., *Renewable Energy: A First Course*. 2013, Boca Raton, CRC Press.
2. Soares, C., *Gas Turbines: A Handbook of Air, Land, and Sea Applications*. 2nd ed. 2015, Amsterdam: Butterworth-Heinemann.
3. Giampaolo, T., *Gas Turbine Handbook: Principles and Practice*. 5th ed. 2014, Lilburn, Fairmont Press.
4. McLarty, D., Brouwer, J., Samuelsen, S., "Fuel Cell–Gas Turbine Hybrid System Design Part I: Steady State Performance." Journal of Power Sources, 2014. 257: p. 412-420.
5. Wikipedia, "Brayton Cycle." 2018 [cited 2018 24.05.2018], available from: https://en.wikipedia.org/wiki/Brayton_cycle
6. Boyce, M.P., *Gas Turbine Engineering Handbook*. 4rd ed. 2012, Oxford, Butterworth-Heinemann.
7. Kuo, K.K., *Principles of Combustion*. 2nd ed. 2005, Hoboken, Wiley.
8. Saravanamuttoo, H.I.H., Rogers, G.F.C., Cohen, H., Straznicky, P.V., *Gas Turbine Theory*. 6th ed. 2009, Harlow, Prentice Hall.
9. Poinsot, T., Veynante, D., *Theoretical and Numerical Combustion*. 2nd ed. 2005, Philadelphia, Edwards.
10. Mjølhus, A., Andreassen, S., "Prosjektering og bygging av gassturbin." 2012, Høgskolen i Bergen, Institutt for maskin- og marinfag.
11. Leknes, E., Myklebust, M., Ellingsen, Ø., "Prosjektering og videreutvikling av gassturbin." 2013, Høgskolen i Bergen, Institutt for maskin- og marinfag.
12. Bergquist, E., Seth, M., "Målinger og termodynamisk analyse av gassturbin." 2014, Høgskolen i Bergen, Institutt for maskin- og marinfag.
13. Larsson, C., Omar, O., "Videreutvikle IMM sin modell gassturbin for å drive en kraftturbin." 2015, Høgskolen i Bergen, Institutt for maskin- og marinfag.
14. Munteanu, N., "Prediction of the Emission Generated from the Combustion of Non-premixed Methane-Hydrogen Mixture." 2017, Western Norway University of Applied Sciences, Department of Mechanical and Marine Engineering.
15. Mallouppas, G., Goldin, G., Zhang, Y., Thakre, P., Krishnamoorthy, N., Rawat, R., Gosman, D., Rogerson, J., Bulat, G., "Investigation of an Industrial Gas Turbine Combustor and Pollutant Formation Using LES." Proceedings of ASME Turbo Expo 2017: Turbomachinery Technical Conference and Exposition, 2017. p. 1-10.
16. Calabria, R., Chiariello, F., Massoli, P., Reale, F., "Numerical Study of a Micro Gas Turbine Fed by Liquid Fuels: Potentialities and Critical Issues." Energy Procedia, 2015. 81: p. 1131-1142.
17. Enagi, I.I., Al-Attab, K.A., Zainal, Z.A. "Combustion Chamber Design and Performance for Micro Gas Turbine Application." Fuel Processing Technology, 2017. 166: p. 258-268.
18. Krieger, G.C., de Campos, A.P.V., Filho, F.L.S., de Souze, R.C., "A Swirler Stabilized Combustion Chamber for a Micro-gas Turbine Fuelled With Natural Gas." Journal of the Brazilian Society of Mechanical Sciences and Engineering, 2012. 34(4): p. 441-449.
19. Cant, R.S., Mastorakos, E., *An Introduction to Turbulent Reacting Flows*. 2008, London, Imperial College Press.
20. Siemens Star-CCM+, "Fundamental Equations." Star-CCM+ online documentation 2018 [cited 2018 26.03], available from: https://documentation.thesteveportal.plm.automation.siemens.com/starccmplus_latest_en/index.html?param=7f.BV&authLoc=https://thesteveportal.plm.automation.siemens.com/AuthoriseRedirect#page/STARCCMP%2FGUID-47D00AD4-3E64-46A7-92AF-AEE070D3A71D%3Den%3D.html%23

21. Siemens Star-CCM+, "Fluid Flow." Star-CCM+ online documentation 2018 [cited 2018 27.03], available from: https://documentation.thesteveportal.plm.automation.siemens.com/starccmplus_latest_en/index.html#page/STARCCMP/GUID-B55A7D91-D613-4E1E-A7C2-133B3260A16B=en=.html#wwID0EKEZTC
22. Amzin, S., Swaminathan, N., "Computations of Turbulent Premixed Flames using Conditional Moment Closure." 2013, University of Cambridge, Department of Engineering.
23. Siemens Star-CCM+, "LES and Subgrid Scale Turbulence Models Reference." Star-CCM+ online documentation 2018 [cited 2018 29.01], available from: https://documentation.thesteveportal.plm.automation.siemens.com/starccmplus_latest_en/index.html?param=215dz&authLoc=https://thesteveportal.plm.automation.siemens.com/AuthoriseRedirect#page/STARCCMP%2FGUID-C47DD313-B23C-43A4-B614-E0E0A79515F9%3Den%3D.html
24. Siemens Star-CCM+, "Reynolds-Averaged Navier-Stokes (RANS) Turbulence Models." Star-CCM+ online documentation 2018 [cited 2018 28.03], available from: https://documentation.thesteveportal.plm.automation.siemens.com/starccmplus_latest_en/index.html?param=wtc_A&authLoc=https://thesteveportal.plm.automation.siemens.com/AuthoriseRedirect#page/STARCCMP%2FGUID-235E939A-BC77-4988-AE0A-D79B17FD6072%3Den%3D.html%23
25. Siemens Star-CCM+, "Eddy Viscosity Models." Star-CCM+ online documentation 2018 [cited 2018 30.03], available from: https://documentation.thesteveportal.plm.automation.siemens.com/starccmplus_latest_en/index.html?param=wtc_A&authLoc=https://thesteveportal.plm.automation.siemens.com/AuthoriseRedirect#page/STARCCMP%2FGUID-3A7C1AA6-74F0-458C-BF8F-BA9BDF8B5789%3Den%3D.html%23wwID0EOXOVC
26. Siemens Star-CCM+, "K-Epsilon Turbulence." Star-CCM+ online documentation 2018 [cited 2018 11.04], available from: https://documentation.thesteveportal.plm.automation.siemens.com/starccmplus_latest_en/index.html#page/STARCCMP%2FGUID-82CD7ECC-1BB5-4DA1-B024-273814BB8E3D%3Den%3D.html%23
27. Field, A., "What is meant by "All y+ Wall Treatment?" Star-CCM+ online documentation 30.10.2017 [cited 2018 11.04.2018], available from: https://documentation.thesteveportal.plm.automation.siemens.com/starccmplus_latest_en/index.html#page/STARCCMP%2FGUID-82CD7ECC-1BB5-4DA1-B024-273814BB8E3D%3Den%3D.html%23
28. Siemens Star-CCM+, "K-Epsilon Solvers Reference." Star-CCM+ online documentation 2018 [cited 2018 11.04.2018], available from: https://documentation.thesteveportal.plm.automation.siemens.com/starccmplus_latest_en/index.html#page/STARCCMP%2FGUID-A0E5537B-8853-4AE0-93D3-0C685EDE2D25%3Den%3D.html%23
29. Siemens Star-CCM+, "Reacting Flow." Star-CCM+ online documentation 2018 [cited 2018 27.03], available from: https://documentation.thesteveportal.plm.automation.siemens.com/starccmplus_latest_en/index.html?param=r.cq7&authLoc=https://thesteveportal.plm.automation.siemens.com/AuthoriseRedirect#page/STARCCMP%2FGUID-F057047C-0E4F-4E91-8A1C-DAB17F993E95%3Den%3D.html%23
30. Qin, Z., Lissianski, V.V., Yang, H., Gardiner, W.C., Davis, S.G., Wang, H., "Combustion Chemistry of Propane: A Case Study of Detailed Reaction Mechanism Optimization." Proceedings of the Combustion Institute, 2000. 28: p. 1663-1669.

31. Lin, K.C., Chiu, C.T., "A Compact Skeletal Mechanism of Propane Towards Applications From NTC-affected Ignition Predictions to CFD-modeled Diffusion Flames: Comparisons with Experiments." Fuel, 2017. 203: p. 102-112.
32. Law, C.K., *Combustion physics*. 2006, Cambridge, Cambridge University Press
33. Gong, J., Zhang, S., Cheng, Y., Huang, Z., Tang, C., Zhang, J., "A Comparative Study of n-Propanol, Propanal, Acetone, and Propane Combustion in Laminar Flames." Proceedings of the Combustion Institute, 2015. 35: p. 795-801.
34. Siemens Star-CCM+, "Mass Flow Inlet." Star-CCM+ online documentation 2018 [cited 2018 28.03], available from: https://documentation.thesteveportal.plm.automation.siemens.com/starccmplus_latest_en/index.html?param=wtc_A&authLoc=https://thesteveportal.plm.automation.siemens.com/AuthoriseRedirect#page/STARCCMP%2FGUID-AA234180-32CD-472D-8AA6-E6320A74E4C5%3Den%3D.html%23
35. Siemens Star-CCM+, "Wall." Star-CCM+ online documentation 2018 [cited 2018 28.03], available from: https://documentation.thesteveportal.plm.automation.siemens.com/starccmplus_latest_en/index.html?param=wtc_A&authLoc=https://thesteveportal.plm.automation.siemens.com/AuthoriseRedirect#page/STARCCMP%2FGUID-5DE29F16-9941-4E8A-B2F7-F110FC40E583%3Den%3D.html%23
36. Siemens Star-CCM+, "K-Epsilon Wall Treatment." Star-CCM+ online documentation 2018 [cited 2018 15.05.2018], available from: https://documentation.thesteveportal.plm.automation.siemens.com/starccmplus_latest_en/index.html#page/STARCCMP/GUID-B812CA7B-AB9E-4DD6-B73E-A69031DD3CAA=en=.html
37. Siemens Star-CCM+, "Wall Treatment." Star-CCM+ online documentation 2018 [cited 2018 15.05.2018], available from: https://documentation.thesteveportal.plm.automation.siemens.com/starccmplus_latest_en/index.html#page/STARCCMP/GUID-B812CA7B-AB9E-4DD6-B73E-A69031DD3CAA=en=.html
38. Siemens Star-CCM+, "Meshers in STAR-CCM+." Star-CCM+ online documentation 2018 [cited 2018 26.03], available from: https://documentation.thesteveportal.plm.automation.siemens.com/starccmplus_latest_en/index.html?param=7f.BV&authLoc=https://thesteveportal.plm.automation.siemens.com/AuthoriseRedirect#page/STARCCMP%2FGUID-699068E9-523E-4320-8390-09192C29F61B%3Den%3D.html%23
39. Siemens Star-CCM+, "Checking the Surface Validity." Star-CCM+ online documentation 2018 [cited 2018 15.05.2018], available from: https://documentation.thesteveportal.plm.automation.siemens.com/starccmplus_latest_en/index.html#page/STARCCMP/GUID-B812CA7B-AB9E-4DD6-B73E-A69031DD3CAA=en=.html

Appendix

Mixture Fraction for Stoichiometric Combustion of Propane

Mole O_2 for stoichiometric combustion, Y_{O2}:

$$C_xH_y = C_3H_8 \rightarrow X = 3, Y = 8 \quad (25)$$

Mole O_2 for stoichiometric combustion, Y_{O2}:

$$a = x + \frac{y}{4} = 3 + \frac{8}{4} = 5 \quad (26)$$

Air Fuel Ratio, $AFR_{stoichiometic}$:

$$4{,}76a \times \frac{MW_{air}}{MW_{fuel}} = 4{,}76 \times 5 \times \frac{28{,}85}{44{,}097} = 15.60523 \quad (27)$$

Stoichiometric Mixture Fraction:

$$\frac{1}{1+AFR_{stoichiometric}} = \frac{1}{1+15.60523} = 0.06022 \quad (28)$$

A mixture fraction of 0.0622 indicates peak temperature at standard reference conditions for temperature and pressure. Reference temperature is 298.15 K and reference pressure is 1.0 bar according to Kuo [7].

Plot of Mixture Fraction vs. Species Mass Fraction with Z_{var} = 0

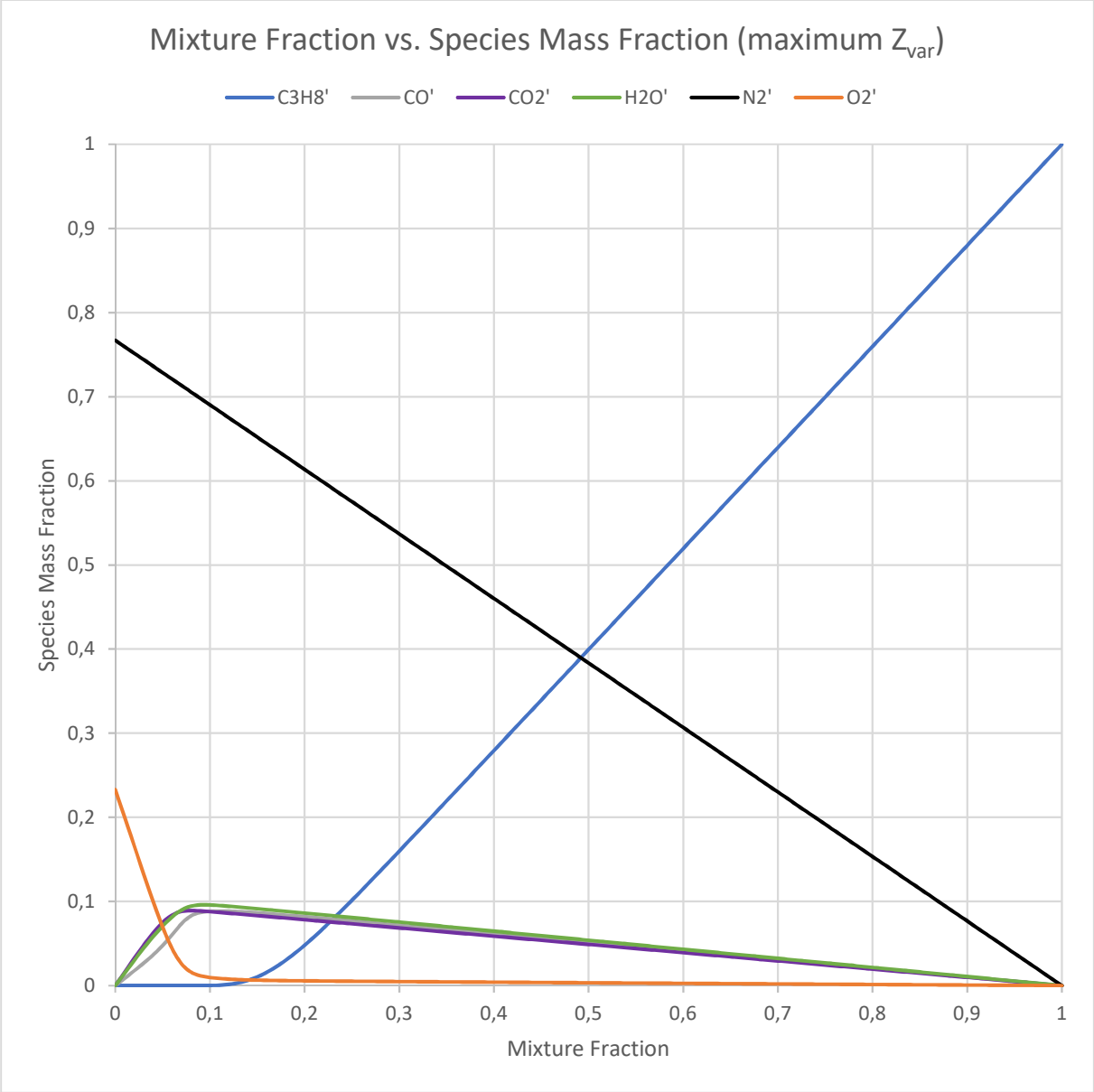

Figure 69: *All species selected for tabulation in the SLF table. The sum of all mass fractions for the species at a given mixture fraction totals to 1. The values for mixture fraction are plotted with mixture fraction variance Z_{var} = maximum.*

Plot of P3 Absolute Pressure Measurement Point vs. Cell Count

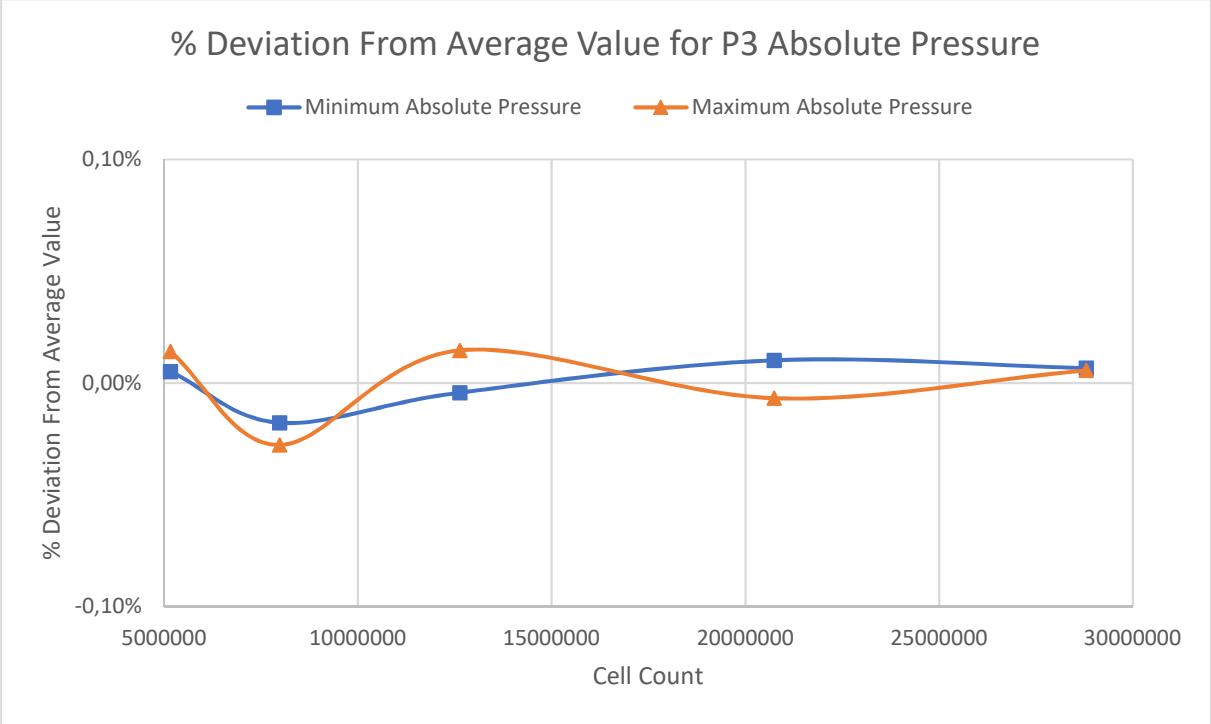

Figure 70: *The figure shows a graph for the percentage of change in engineering scalars for P3 absolute pressure measurement points, when compared to the average value of the five simulation runs performed in the mesh independence check for case 1. The graph is detailed with smoothed lines to clearly show the trend. There is very little deviation in the results with regards to cell count.*